12-2008

Localized Corrosion Behavior of Zr-based Bulk Metallic Glasses in Neutral NaCl Electrolytes

Brandice Annette Green
University of Tennessee - Knoxville

To the Graduate Council:

I am submitting herewith a dissertation written by Brandice Annette Green entitled "Localized Corrosion Behavior of Zr-based Bulk Metallic Glasses in Neutral NaCl Electrolytes." I have examined the final electronic copy of this dissertation for form and content and recommend that it be accepted in partial fulfillment of the requirements for the degree of Doctor of Philosophy, with a major in Materials Science and Engineering.

Peter K. Liaw, Major Professor

We have read this dissertation and recommend its acceptance:

Roberto Benson, Hahn Choo, Chain-Tsuan Liu, David C. Joy

Accepted for the Council:
Carolyn R. Hodges

Vice Provost and Dean of the Graduate School

(Original signatures are on file with official student records.)

To the Graduate Council:

I am submitting herewith a dissertation written by Brandice Annette Green entitled "Localized Corrosion Behavior of Zr-based Bulk Metallic Glasses in neutral NaCl electrolytes." I have examined the final electronic copy of this dissertation for form and content and recommend that it be accepted in partial fulfillment of the requirements for the degree of Doctor of Philosophy, with a major in Materials Science and Engineering.

_____
Peter K. Liaw, Major Professor

We have read this dissertation
and recommend its acceptance:

_____
[Roberto Benson]

_____
[Hahn Choo]

_____
[Chain-Tsuan Liu]

_____
[David C. Joy]

Accepted for the Council:

_____
Carolyn R. Hodges
Vice Provost and Dean of the Graduate School

LOCALIZED CORROSION BEHAVIOR OF ZR-BASED BULK METALLIC GLASSES IN NEUTRAL NACL ELECTROLYTES

A Dissertation
Presented for the
Doctor of Philosophy
Degree
The University of Tennessee, Knoxville

Brandice Annette Green
December 2008

ACKNOWLEDGEMENTS

I would like to express my gratitude to my advisors, Profs. Peter K. Liaw and the late Raymond A. Buchanan, for all of their support, encouragement, and guidance while completing my doctoral studies. I would like to thank my committee members, Profs. Roberto Benson, Hahn Choo, David Joy, and C.T. Liu, for providing fruitful discussions and offering novel solutions.

I would like to acknowledge the following groups for their funding: Tennessee Advanced Materials Laboratory [(TAML) under the guidance of Prof. Ward E. Plummer]; the National Science Foundation (NSF) Graduate Research Fellowship; Pipeline Engineering Diversity Program [supervised by Dr. Wayne Davis and Mr. James T. Pippin]; and the NSF Integrative Graduate Education and Research Training (IGERT) Program [under DGE-9987548, C. J. Van Hartesveldt, and Dr. Judith Giordan]. The Auger work was sponsored by the Assistant Secretary for Energy Efficiency and Renewable Energy, Office of FreedomCAR and Vehicle Technologies, as part of the High Temperature Materials Laboratory (HTML) User Program, Oak Ridge National Laboratory (ORNL), managed by UT-Battelle, LLC, for the U.S. DOE under contract number DE-AC05-00OR22725.

I extend my sincerest appreciation to all the staff in the materials science and engineering department at The University of Tennessee, Knoxville. I am pleased to thank Ms. Roberta Campbell, Ms. Carla Lawrence, and Ms. Sandra Maples, for all of their administrative support over the years. I would like to acknowledge the gentlemen in the machine shop, Mr. Doug E. Fielden, Mr. Danny Hackworth, and Mr. Larry Smith, for always doing impeccable work and providing my samples in a timely manner. I am

grateful to Mr. Howard (Brad) Synder, Mr. Steve Steiner, and Mr. Mike Neal (retired) from the electronics shop for their assistance with equipment. I thank Ms. Carol Winn for her help with the logistical aspects of my experimental setups. I would like to express appreciation to Mr. Gregory Jones for his instruction and guidance with various microscopes. I would also like to thank Mr. Frank Holiway and Mr. Randy Stooksbury for help with purchasing supplies and materials needed for my research.

I am grateful to Profs. Easo George and C.T. Liu for allowing me to conduct research within the Alloy Behavior and Design Group of the Materials Science and Technology (MS&T) Division at the Oak Ridge National Laboratory (ORNL). I would like to thank Mr. Cecil Carmichael for assistance with the arc-melting and Ms. Sherry Samples for providing administrative support. I would like to express appreciation to Drs. Mike Brady and Mike Miller (MS&T) for fruitful discussions and assistance with my book chapter. I would like to acknowledge Dr. Harry Meyer from the High Temperature Materials Laboratory (HTML) at ORNL for performing the Auger experiments. I am grateful to Dr. Stephen Jesse for designing the sample holder and helping with the atomic force microscopy (AFM) experiments. I would also like to thank Dr. Maxim Nikiforov and Dr. Katyayani Seal for their assistance with the in-situ AFM experiments that were conducted at the Center for Nanophase Materials Science (CNMS) at the ORNL.

I would like to express appreciation to Prof. Yoshihiko Yokoyama (Tohoku University, Sendai, Japan) for providing samples and great guidance for my research. Thanks to the many others with which I have collaborated and that have assisted my research: Profs. Narendra Dahotre, Kenneth Kihm, and George Schweitzer; Drs. Michael

Benson, Marios Demetriou, Chang Choi, Mark Morrison, William Peter, Rejanah Steward, and Gongyao Wang; Mr. Bryan Barnard, Mr. Andrew Chuang, Mr. Iltai Kim, Mr. Sameer Paital, Mr. Michael Peretich, Mr. Christopher Stephens, Mr. Jake Stewart; Ms. Irene Paulauskas, Ms. Dongchun Qiao, and Ms. Lu Huang.

Special thanks to Dr. Denise Jackson and Mr. James Pippin for their encouragement and support. To my dear Brandon, who has managed to keep me laughing, thank you for always knowing what to say. Last but certainly not least, I express my deep gratitude to my parents, Archie and Barbara, for their support, love, and most of all the foundation of abiding faith in Christ that has kept me through the good times and the not so good times.

ABSTRACT

The electrochemical behaviors the $Zr_{50}Cu_{40}Al_{10}$, $Zr_{50}Cu_{33}Al_{10}Pd_7$, and $Zr_{52.5}Cu_{17.9}Al_{10}Ni_{14.6}Ti_{5.0}$ BMGs were investigated in NaCl solutions. Both $Zr_{50}Cu_{40}Al_{10}$ and $Zr_{50}Cu_{33}Al_{10}Pd_7$ exhibited poor corrosion behaviors. $Zr_{50}Cu_{40}Al_{10}$ was vulnerable to localized corrosion at the open-circuit conditions (OCC). $Zr_{50}Cu_{33}Al_{10}Pd_7$ experienced localized corrosion at OCC or at slightly higher potentials. Anodic-polarization of both alloys demonstrated that small increases in the applied potential resulted in significant increases in the current density. Scanning electron microscopy examination of the corroded surfaces of both the $Zr_{50}Cu_{40}Al_{10}$ and $Zr_{50}Cu_{33}Al_{10}Pd_7$ BMGs revealed that an oxide layer formed on the surfaces after the exposure to the chloride solutions. In both cases, the growth pattern of the oxide seemed to be related to a dendritic structure. Scanning Auger microanalysis of the heavily corroded areas on $Zr_{50}Cu_{40}Al_{10}$ showed that the attacked regions were enriched with Cu, Cl, and O. Higher concentrations of Pd and Cu were observed in pits as opposed to the surface of $Zr_{50}Cu_{33}Al_{10}Pd_7$. A corrosion mechanism related to a galvanic electrode effect and the formation of CuCl and CuO was proposed.

The anodic-polarization behavior of $Zr_{52.5}Cu_{17.9}Al_{10}Ni_{14.6}Ti_{5.0}$ (Vitreloy 105) was improved over the behaviors of $Zr_{50}Cu_{40}Al_{10}$ and $Zr_{50}Cu_{33}Al_{10}Pd_7$. Corrosion investigations were performed on samples obtained from regions transverse to and along the long axis of Vitreloy 105 ingots. “Swirl” features, usually thought to be areas of crystallinity, were visible in the longitudinal samples. Some longitudinal samples were treated with a laser in attempts to induce crystallinity. The cross-sectional samples were passivated at OCC; however, pits did initiate after significant overpotentials were

applied. Some regions of the pits had a porous morphology that was enriched with Cu. The longitudinal samples also exhibited passive behavior at OCC. However, despite the presence of the "swirl" regions, the longitudinal samples were immune to pitting corrosion for the tested potential range. In-situ AFM experiments were performed on longitudinal samples in 0.6 M NaCl at an applied potential of -190 mV, SCE. Generally, the height of the surface increased with time, which was thought to be related to the thickening of the passive film. This observation may be associated with the improved pitting resistance of the longitudinal samples.

TABLE OF CONTENTS

Chapter 1. Introduction 1

Chapter 2. Review of the Literature 4

2.1. History of Metallic Glasses and Bulk Metallic Glasses 4

2.2. Glass-Forming Ability in Amorphous Alloys 5

2.3. Relevance of Zr-based Bulk Metallic Glasses (BMGs) 7

2.4. Corrosion Behavior of Zr-based Metallic Glasses and Bulk Metallic Glasses (BMGs) 8

2.4.1. The Effect of Structure on the Corrosion Behavior of Metallic Glasses and Bulk Metallic Glasses (BMGs) 9

2.4.2. The Effect of Composition on the Corrosion Behavior of Metallic Glasses and Bulk Metallic Glasses (BMGs) 14

2.4.3. Pitting Mechanisms of Zr-based Metallic Glasses and Bulk Metallic Glasses (BMGs) 16

2.4.4. Summary 19

Chapter 3. Theoretical Background 20

3.1. Atomic Force Microscopy 20

3.2. Differential Scanning Calorimetry and Differential Thermogravimetric Analysis 21

3.3. Polarization Experiments 21

3.4. Scanning Auger Spectroscopy 24

Chapter 4. Experimental Methods 27

4.1. Materials 27

4.2. Experimental Techniques 28

4.2.1. X-Ray Diffraction 28

4.2.2. Differential Scanning Calorimetry 28

4.2.3. Differential Thermogravimetric Analysis 28

4.2.4. Laser Treatments 28

4.2.5. Polarization Experiments 29

4.2.6. In-situ Optical Microscopy 30

4.2.7. In-situ Atomic Force Microscopy 30

4.2.8. Scanning Auger Microscopy 32

Chapter 5. Results 33

5.1. XRD, Thermal Analysis, and SAM 33

5.2. Electrochemical Results 34

5.2.1. Polarization Behavior of $Zr_{50}Cu_{40}Al_{10}$ 34

5.2.2 Polarization Behavior of $Zr_{50}Cu_{33}Al_{10}Pd_7$ 37
5.2.3 Polarization Behavior of Vitreloy 105 37
5.2.4. Polarization Behavior of Laser-treated Vitreloy 105 38
5.2.5. Electrochemical-AFM Results 39
5.2.6. Polarization behavior of Crystalline Constituents 40
5.3. Surface Examination (OM, SEM, SAM, and XRD) of Corroded Surfaces 41
5.3.1. $Zr_{50}Cu_{40}Al_{10}$ 41
5.3.2. $Zr_{50}Cu_{33}Al_{10}Pd_7$ 44
5.3.3. Vitreloy 105 45
Chapter 6: Discussion 47
6.1. Discussion of the Polarization Behavior of $Zr_{50}Cu_{40}Al_{10}$, $Zr_{50}Cu_{33}Al_{10}Pd_7$, Vitreloy 105, and the Crystalline Metals 47
6.2. Discussion of the Corroded Surfaces of $Zr_{50}Cu_{40}Al_{10}$, $Zr_{50}Cu_{33}Al_{10}Pd_7$, and Vitreloy 105 50
6.3. Discussion of the Chemical Character of the Corroded Surfaces of $Zr_{50}Cu_{40}Al_{10}$, $Zr_{50}Cu_{33}Al_{10}Pd_7$, and Vitreloy 105 52
6.4. Proposed Pitting Mechanisms 53
6.4.1. $Zr_{50}Cu_{40}Al_{10}$ 53
6.4.2. $Zr_{50}Cu_{33}Al_{10}Pd_7$ 56
6.4.3. Vitreloy 105 (cross-sectional samples) 57
Chapter 7: Conclusions 59
Chapter 8: Future Work 62
References 64
Appendix of Tables 73
Appendix of Figures 80

List of Tables

Table 1. Transition temperatures and GFA parameters. 74
Table 2. Mean polarization parameters for $Zr_{50}Cu_{40}Al_{10}$ in NaCl electrolytes of varying chloride concentration. 75
Table 3. Polarization parameters for $Zr_{50}Cu_{33}Al_{10}Pd_7$ in 0.6 M NaCl electrolytes of varying chloride concentration. 76
Table 4 . Atomic concentrations of positions given in Figure 61. 77
Table 5. Standard Gibbs free energies of formation of selected oxides. 78
Table 6. Selected Standard Electrode Potentials in Aqueous Solutions. 79

List of Figures

Figure 1. Temperature dependence of the specific volume of a molten metal that undergoes solidification by crystallization (gray curve) or by vitrification (black curve). 81

Figure 2. Critical cooling rate (R_c) versus maximum thickness (t_{max}) for various BMG systems. Figure was generated from data published by Inoue [3]. 82

Figure 3. Temperatures that can be obtained from thermal analysis techniques. T_g, T_x, T_s, and T_l represent the glass transition, crystallization, solidus, and liquidus temperatures, respectively. 83

Figure 4. (top) Tensile strength versus Young's modulus and (bottom) Vickers hardness versus Young's modulus for various BMG systems and crystalline alloys [3]. 84

Figure 5. S-N fatigue curves of conventional crystalline alloys and Zr-based BMGs [9]. 85

Figure 6. Scanning electron microscopy (SEM) image [11] demonstrating local attack generated at a crystalline inclusion in a $Zr_{55}Cu_{30}Al_{10}Ni_5$ amorphous alloy. The experiment was performed in a 10^{-3} M NaCl electrolyte. 86

Figure 7 (a) Optical micrograph of a crystalline "swirl" region on the surface of Vitreloy 105 [106]. (b) SEM image of microstarlets on Vitreloy 105 [126]. 87

Figure 8. Polarization curves of selected Zr-based BMGs generated in 0.5 and 0.6 M NaCl electrolytes from various literature reports [15, 27, 97, 99, 103]. 88

Figure 9. Corrosion pit on the surface of a $Zr_{59}Ti_3Cu_{20}Al_{10}Ni_8$ BMG illustrating cracked and honeycomb (porous) morphologies of pits [104]. 89

Figure 10. SEM images of Vitreloy 105 (a) before an anodic-polarization experiment and (b) after the anodic-polarization experiment [106]. 90

Figure 11. A schematic illustrating the components of an atomic force microscope (AFM). The x-, y-, and z piezoelectric devices are represented as X-P, Y-P, and Z-P, respectively. FS is the force sensor, and FCU is the feedback control unit. The frame of the AFM unit is denoted by F. 91

Figure 12. Components of the electrochemical cell. 92

Figure 13. Polarization curve of a passivating alloy with important corrosion parameters denoted. 93

Figure 14. Polarization curve of a material that exhibits Tafel behavior with an anodic diffusion limiting current density 94

Figure 15. Relaxation process of a surface bombarded with an electron beam by the ejection of an Auger electron [50]. 95

Figure 16. Experimental setup of the in-situ OM technique. The electrochemical cell is placed on the microscope stage. Electrodes from the electrochemical cell are connected to a potentiostat that is interfaced to a computer with corrosion software. The optical microscope is attached to a CCD camera that is interfaced to a computer containing a frame grabber. 96

Figure 17. (a) View of the AFM in-situ corrosion set-up. (b) Close up of the AFM stage showing the AFM probe holder and the electrochemical cell within the sample holder. The holder houses the sample and the electrolyte. 97

Figure 18. (a) Front view of the sample holder for the AFM in-situ corrosion experiments. (b) Back view of the sample holder..... 98
Figure 19. Representative XRD patterns for the $Zr_{50}Cu_{40}Al_{10}$, $Zr_{50}Cu_{33}Al_{10}Pd_7$, and Vitreloy 105 BMGs..... 99
Figure 20. Representative DSC thermograms of $Zr_{50}Cu_{40}Al_{10}$, $Zr_{50}Cu_{33}Al_{10}Pd_7$, and Vitreloy 105 indicating T_g and T_x..... 100
Figure 21. Thermograms of fusion of $Zr_{50}Cu_{40}Al_{10}$, $Zr_{50}Cu_{33}Al_{10}Pd_7$, and Vitreloy 105 generated with DTA. Black and pink arrows denote the solidus temperature (T_s) and liquidus temperature (T_l), respectively, for each alloy. 101
Figure 22. Auger sputter depth profiles of the as-received $Zr_{50}Cu_{40}Al_{10}$ BMG. Sputter rate = 0.025 nm/s. 102
Figure 23. Auger sputter depth profiles of the as-received $Zr_{50}Cu_{33}Al_{10}Pd_7$ BMG. Sputter rate = 0.025 nm/s. 103
Figure 24. (top left) SEM image of the as-polished surface of $Zr_{50}Cu_{40}Al_{10}$ after sputter etching. Zr, Cu, Al, C Auger elemental maps of the surface are presented. A combined Auger map of Zr, Cu, and Al is also shown (lower right). 104
Figure 25. SEM image of the as-polished surface of Vitreloy 105 after sputter etching. Auger combined maps of the area are displayed. 105
Figure 26. Polarization curves of $Zr_{50}Cu_{40}Al_{10}$ generated in naturally aerated 0.6 M NaCl electrolytes. The initial and final slopes (m_1 and m_2, respectively) are indicated on scan 2..... 106
Figure 27. Polarization curves of $Zr_{50}Cu_{40}Al_{10}$ generated in naturally aerated 0.1 M NaCl electrolytes. 107
Figure 28. Representative polarization curves of $Zr_{50}Cu_{40}Al_{10}$ obtained from an in-situ experiment in 0.6 M NaCl (black curve) and from a bulk experiment in 0.6 M NaCl. Both experiments were performed open to air. 108
Figure 29. OM dark-field images (a) – (d) corresponding to the four conditions denoted on the polarization curve in Figure 28. 109
Figure 30. Magnification of Figure 28 indicating the onset of diffusion (concentration) polarization for $Zr_{50}Cu_{40}Al_{10}$ polarization curves generated in the in situ setup and in a bulk volume of solution..... 110
Figure 31. Polarization curves of $Zr_{50}Cu_{33}Al_{10}Pd_7$ generated in naturally aerated 0.6 M NaCl electrolytes..... 111
Figure 32. Open-circuit potential versus time potential illustrating the variation of the E_{corr} of $Zr_{50}Cu_{33}Al_{10}Pd_7$ in a naturally aerated 0.6 M NaCl electrolyte. 112
Figure 33. Polarization curves of Vitreloy 105 generated in naturally aerated 0.6 M NaCl electrolytes. 113
Figure 34. Polarization curves of Vitreloy 105 generated in naturally aerated 0.3 M NaCl electrolytes. 114
Figure 35. Polarization curves of Vitreloy 105 generated in naturally aerated 0.3 M NaCl electrolytes excluding the outlier (scan 4). 115
Figure 36. Polarization curves of Vitreloy 105 generated in naturally aerated 0.1 M NaCl. 116
Figure 37. Corrosion potentials (E_{corr}) of Vitreloy 105 as a function of chloride concentration. Circles and error bars represent mean values and 95% confidence intervals, respectively..... 117

Figure 38. The pitting resistance parameters ($E_{pit} - E_{corr}$) of Vitreloy 105 as a function of chloride concentration. Circles and error bars represent mean values and 95% confidence intervals, respectively. Mean values are noted on the chart. 118
Figure 39. The passive current densities (i_p) of Vitreloy 105 as a function of chloride concentration. Circles and upper error bars represent mean values and upper 95% confidence intervals, respectively. Lower confidence intervals were omitted if they resulted in negative i_p values. Mean values are noted on the chart. 119
Figure 40. The corrosion current densities (i_{corr}) of Vitreloy 105 as a function of chloride concentration. Circles and upper error bars represent mean values and upper 95% confidence intervals, respectively. Lower confidence intervals were omitted if they resulted in negative i_{corr} values. Mean values are noted on the chart. 120
Figure 41. The corrosion penetration rates (CPR) of Vitreloy 105 as a function of chloride concentration. Circles and upper error bars represent mean values and upper 95% confidence intervals, respectively. Lower confidence intervals were omitted if they resulted in negative CPRs. Mean values are noted on the chart. 121
Figure 42. (top) Optical micrographs of "swirl" regions on the Vitreloy 105 BMG. (bottom) magnified image of the region. 122
Figure 43. Polarization curves of Vitreloy 105 longitudinal samples. The sample polarized in scan 1 was laser treated. 123
Figure 44. In-situ AFM topographic images of Vitreloy 105. Experiments were performed in a 0.6 M NaCl, and a potential of -190 mV, SCE was applied to the sample. Images (a), (b), (c), and (d) correspond to frames 1, 3, 5, and 7, respectively. The acquisition per frame was 10.7 minutes. Profiles of the four images were obtained at the position denoted by the dashed line in image (a). 124
Figure 45. AFM topographic profiles along the dashed line shown in Figure 44 at various times during the potentiostatic experiment. The subscripts correspond to the frame number. The time that had elapsed between the profiles was approximately 21 minutes. 125
Figure 46. Representative polarization curves of crystalline Zr, Cu, Al, and Ni generated in 0.6 M NaCl electrolytes. 126
Figure 47. Representative polarization curves of Zr, Cu, Ni, and Ti from experiments performed in 0.6 M NaCl. 127
Figure 48. SEM micrograph of a corroded region at the insulating enamel/sample interface $Zr_{50}Cu_{40}Al_{10}$ sample formed at E_{corr} (i.e., not anodically polarized) in a 0.6 M NaCl electrolyte. 128
Figure 49. SEM photomicrograph of the surface $Zr_{50}Cu_{40}Al_{10}$ illustrating the corrosion that occurs at E_{corr} (i.e., not anodically polarized) in a 0.6 M NaCl electrolyte. The area is of an area of the corroded region shown in Figure 48. The red circles highlight dendrites. 129
Figure 50. (a) SEM micrograph of $Zr_{50}Cu_{40}Al_{10}$ after a polarization experiment in a 0.1 M NaCl electrolyte illustrating the irregular shape of pits on the surface. (b) Magnified corrosion pit 130

Figure 51. SEM micrograph of $Zr_{50}Cu_{40}Al_{10}$ after a polarization experiment in a 0.1 M NaCl electrolyte illustrating the cracks due to exfoliation corrosion. 131
Figure 52. (a) SEM micrograph of $Zr_{50}Cu_{40}Al_{10}$ after a polarization experiment in a 0.1 M NaCl electrolyte showing an area of the surface covered with corrosion products. (b) EDS analysis of the regions of the surface denoted in (a)..... 132
Figure 53. (top left) SEM micrograph image of pits on the surface of a $Zr_{50}Cu_{40}Al_{10}$ sample after polarization in a 0.6 M NaCl electrolyte to 300 mV, SCE. (top right) Color-combined Auger map of Cu (red), Cl (blue), and O (green) corresponding to the area shown in the micrograph. (bottom) Gray-scale Auger map of Zr (white) present in the aforementioned area..... 133
Figure 54. (row 1) Scanning electron image of a heavily corroded portion of the polarized $Zr_{50}Cu_{40}Al_{10}$ sample. (row 2, left to right) Auger maps of C; O; Cu; (row 3, left to right) Zr; and Cl after sputter etching. 134
Figure 55. XRD patterns of $Zr_{50}Cu_{40}Al_{10}$ after two different polarization treatments. One sample was anodically polarized to -337 mV, SCE in a 0.1 M NaCl electrolyte. The other sample was polarized to 300 mV, SCE in a 0.6 M NaCl electrolyte..... 135
Figure 56. SEM photomicrograph of the corrosion experienced by $Zr_{50}Cu_{33}Al_{10}Pd_7$ while at open-circuit conditions in a 0.3 M NaCl electrolyte. 136
Figure 57. (a) SEM photomicrograph of the area enclosed in the rectangle shown in Figure 56. (b) Magnified; image of area shown in blue rectangle in (a). 137
Figure 58. (a) Heavily corroded area on the surface of $Zr_{50}Cu_{33}Al_{10}Pd_7$. (b) Magnified image of the area enclosed by the purple rectangle. 138
Figure 59. EDS analyses of the surface of $Zr_{50}Cu_{33}Al_{10}Pd_7$ corresponding to the areas shown in Figure 58b..... 139
Figure 60. Optical micrograph of the region shown in the top image of Figure 45 illustrating the characteristic channels associated with chloride induced corrosion. 140
Figure 61. SEM micrograph of a pit on the surface of $Zr_{50}Cu_{33}Al_{10}Pd_7$ after aborting a polarization experiment in 0.6 M NaCl. Numbered positions correspond to points where survey spectra were attained (see Table 4)..... 141
Figure 62. Auger maps obtained prior to sputtering of (top, left to right) Zr, Cl, Cu, (bottom, left to right) Pd, O, and C. Each of the maps is superimposed on the image shown in Figure 61..... 142
Figure 63. (a) SEM photomicrograph of a pit on Vitreloy 105 after polarization to E_{pit} (mV, SCE). (b) EDS was performed on areas outlined by the blue and yellow rectangles marked on image (a). 143
Figure 64. SEM micrograph of a cluster of pits on the surface of Vitreloy 105 after being polarized to E_{pit}. The bottom portion of the pit shown in Figure 63a is denoted. EDS analyses were performed on the areas within the red and white rectangles. 144
Figure 65. EDS analyses of the area within the yellow rectangle on Figure 63a and the area within the red rectangle in Figure 64. 145
Figure 66. EDS results of the area within the yellow rectangle on Figure 63a and the area within the white rectangle shown in Figure 64. 146

Figure 67. (a) An anodic site between two cathodic sites on a metal surface. (b) A schematic illustrating the current path from the anode to the cathode and the potential gradient within the electrolyte. Adapted from Stansbury and Buchanan [108] 147
Figure 68. Potential-pH equilibrium diagram for Cu-Cl-H_2O at 25^{o}C and a Cl^- concentration of 35,500 ppm [127]. The potential is relative to the hydrogen reference electrode; the standard calomel electrode (SCE) is +241 relative to the hydrogen reference electrode. 148

Nomenclature

A	Ampere
cm	Centimeter
g	Gram
J	Joule
K	Kelvin
M	Molar
mV	Millivolt
mmpy	Millimeters Per Year
N	Normal
nm	Nanometer
ppm	Parts Per Million
s	Second
μm	Micrometer
μm/yr	Micrometers Per Year

Abbreviations and Symbols

γ	Gamma
ρ	Density
ΔT_{xg}	Supercooled Liquid Region
Cl^-	Chloride Ion
Cu^+	Copper (I) Ion/Cuprous Ion
Cu^{2+}	Copper (II) Ion/Cupric Ion
CuCl	Copper (I) Chloride/Cuprous Chloride
$CuCl_2$	Copper (II) Chloride/Cupric Chloride
E_{corr}	Corrosion Potential
E_{pit}	Pitting Potential
H^+	Hydrogen Ion
HCl	Hydrochloric Acid
H_2O	Water
H_2SO_4	Sulfuric Acid
i	Current Density
i_{corr}	Corrosion Current Density
i_d	Diffusion Limiting Current Density
i_p	Passive Current Density
m	Metal-Ion Valence
M	Atomic Mass
NaCl	Sodium Chloride
NaOH	Sodium Hydroxide
Na_2SO_4	Sodium Sulfate
O_2	Oxygen
OH^-	Hydroxide Ion
R_c	Critical Cooling Rate
t_{max}	Maximum Thickness

T	Temperature
T_g	Glass Transition Temperature
T_l	Liquidus Temperature
T_m	Melting Temperature
T_{rg}	Reduced Glass Transition Temperature
T_s	Solidus Temperature
T_x	Onset Crystallization Temperature
AES	Auger Electron Spectroscopy
AFM	Atomic Force Microscope/Microscopy
AAS	Atomic Absorption Spectroscopy
BAA	Bulk Amorphous Alloy
BCC	Body-Centered Cubic
BMG	Bulk Metallic Glass
DSC	Differential Scanning Calorimetry
DSC-TGA	Differential Thermogravimetric Analysis
CPR	Corrosion Penetration Rate
EDX/EDS	Energy- Dispersive X-ray Spectroscopy
GFA	Glass Forming Ability
HCP	Hexagonal-Close Packed
OCC	Open-Circuit Conditions
OM	Optical Microscope/Microscopy
SEM	Scanning Electron Microscope/Microscopy
SCE	Standard Calomel Reference Electrode
XPS	X-ray Photoelectron Spectroscopy
XRD	X-ray Diffraction

Chapter 1. Introduction

Bulk metallic glasses (BMGs) are metal alloys that have amorphous atomic structures. Conventional alloys consist of atoms arranged so that long-range periodic order occurs. Atoms in BMGs have only local, nearest neighbor, ordering [1]. Therefore, these alloys do not have defects that are the result of deviations from a lattice structure (e.g., dislocations and grain boundaries). In addition, second phases, precipitates, and segregates are rare in BMGs [2]. This is because the rapid cooling rates required to produce an amorphous structure decrease the likelihood of appreciable solid-state diffusion. The unique structure of BMGs has led to interest in how their properties compare to their crystalline counterparts. BMGs are shown to exhibit higher tensile strengths, hardnesses, and lower Young's moduli than their crystalline counterparts [3].

The Zr-based BMGs have become an emerging class of materials because of their attractive properties. These alloys readily form their amorphous structure with lower critical-cooling rates (1 -10 K/s) than Fe, Mg, Ti and other BMG compositions. In addition to high strengths [3-5], high hardnesses [6], and low moduli [3, 7], Zr-based BMGs have excellent fatigue properties [3, 8, 9]. These BMGs have been used in sporting goods and electronic casings. They are currently being investigated for coatings and biomedical applications. The prospective applications, especially biomedical related, have underscored the relevance of the aqueous corrosion behavior of these materials. For this reason, several investigations on the aqueous corrosion behavior of Zr-based BMGs have been performed [10-20]. Studies have reported that Zr-based BMGs are vulnerable to pitting corrosion, especially in solutions containing chloride [21-24]. These findings have been fascinating. Zr-based BMGs are expected to be more resistant than their

crystalline counterparts to pitting (localized) corrosion due to their chemical homogeneity and the absence of microstructural defects, such as grain boundaries and second phase precipitates [2, 25, 26]. Also, since BMGs are not restricted by solubility limits, there is flexibility with the alloy design [26]. Specifically, corrosion resistant elements may be added in order to enhance the corrosion resistance of the BMG [11]. However, the pitting corrosion behaviors of Zr-based amorphous alloys have been reported to be only slightly improved when compared to their crystalline counterparts [25, 27].

Explanations have been given in attempts to justify pitting corrosion in Zr-based BMGs, namely, (1) pitting is due to the presence of crystalline inclusions in the amorphous matrix [11, 18] and (2) pitting is due to chemically-distinct regions in the amorphous matrix [18]. The analysis is further complicated by considering that changes in the chemistry may accompany crystalline inclusions. In addition, the chemical composition of inclusions may depend on the nominal composition of the BMG. Though some mechanistic descriptions of the pitting corrosion behavior of Zr-based BMGs are available, they are scarce due to the interest in reporting and ranking the corrosion behaviors of new compositions. Often the descriptions available, though reasonable, have limited experimental support.

The overall goal of the research is to elucidate the pitting corrosion mechanisms of three Zr-based BMGs [$Zr_{50}Cu_{40}Al_{10}$, $Zr_{50}Cu_{33}Al_{10}Pd_{7}$, and $Zr_{52.5}Cu_{17.9}Al_{10}Ni_{14.6}Ti_{5.0}$ (atomic %, at. %)] in chloride containing solutions. This aim will be met by addressing the following questions

(1) How do variations in the alloy composition and chloride ion concentration of the electrolyte affect the anodic-polarization behavior of Zr-based BMGs?

(2) What is the chemical makeup of the electrochemically-treated surfaces of Zr-based BMGs?

(3) What are the corrosion products associated with the polarization of Zr-based BMGs in chloride solutions?

(4) What role (if any) do microcrystalline inclusions play in the pitting corrosion in Zr-based BMGs?

Chapter 2. Review of the Literature

2.1. History of Metallic Glasses and Bulk Metallic Glasses

The structure of metallic elements and their alloys has historically been described as a three-dimensional periodic array of atoms. Duwez and his co-workers at the California Institute of Technology became the first to fabricate amorphous alloys (metallic glasses) by direct quenching from the melt [1]. Though commonly compared to glasses, amorphous alloys consist mainly of metallic elements and have electrical, magnetic, and optical properties similar to conventional metals [28]. In 1960, Klement et al. [29] rapidly cooled $Au_{75}Si_{25}$ from its molten state by splat quenching producing an alloy without long-range periodic order. Figure 1 highlights the difference between the temperature dependence of the specific volume observed during vitrification and crystallization of a molten metal (black and gray curves, respectively) [1, 30]. When a conventional metal is cooled from the melt, a discontinuous decrease in the specific volume is observed if the metal is allowed to crystallize at the equilibrium freezing temperature, T_m. A sufficiently high cooling rate can sometimes suppress the volume discontinuity (i.e., crystallization) and solidification will occur at the glass transition temperature, T_g.

The extreme cooling rate achieved by the splat quenching process enabled the suppression of crystallization during solidification [1]. The quenching rate was estimated to be at least 10^6 K s^{-1} with the resulting thickness varying from 1 to 10 μm [31]. In general, critical cooling rates greater than 10^5 K s^{-1} were required to produce metallic glasses with thicknesses on the order of 50 μm. Thus, the progress of metallic glasses was inhibited by the high critical-cooling rates required to preclude nucleation and

growth of crystalline phases. Alloys of Pd-Cu-Si, Pd-Ni-P, and Pt-Ni-P were exceptions to the rule and considered to be easy glass formers due to (1) critical cooling rates on the order of 10^2 K s^{-1} and (2) their ability to be fabricated into rods of 1 to 3 mm [31]. Drehman, Greer, and Turnbull [32, 33] illustrated that amorphous spheres of $Pd_{40}Ni_{40}P_{20}$ up to 5.3 mm in diameter could be produced with low cooling rates (~ 1.4 K s^{-1}).

By the early 1990s, Inoue and co-workers in Japan had introduced a new series of alloy systems: La- [34], Mg- [35], Zr- [36, 37], Ti- [38], Fe- [39-45], Cu- [46-48], and Pd- [49, 50]. Johnson, Lin, and Peker also made significant contributions with Zr- and Ti-based alloy systems [51, 52]. These novel multicomponent systems required lower critical-cooling rates (some as low as 10^{-1} K s^{-1}) and yielded diameters as large as 1 cm [3, 53]. These systems that readily form glasses are commonly called bulk metallic glasses, BMGs, or bulk amorphous alloys, BAAs.

2.2. Glass-Forming Ability in Amorphous Alloys

Inoue proposed the following three empirical rules for obtaining high glass-forming ability (GFA) in alloys [3] (1) alloy systems containing more than three elements, (2) a difference of atomic ratios of greater than 12%, and (3) negative heats of mixing between the main elements. According to Inoue, these rules cause the formation of a liquid with a new atomic configuration and short-range multicomponent interactions. The new configuration and the short-range interactions increase the solid/liquid interfacial energy (i.e., increase the liquid stability) and require long-range atomic rearrangement for crystallization. In turn, nucleation and growth of crystalline phases are suppressed.

Finding alloy compositions with high GFA has been an important step in attempts to advance the study of amorphous alloys. A low critical cooling rate (R_c) has served as an indicator of good GFA. There is an inverse relationship between the R_c and the maximum specimen thickness, t_{max}. The R_c and t_{max} for various bulk metallic glass systems are presented in Figure 2 [3]. Though R_c is a consistent gauge of GFA, precise measurements of R_c are difficult. Other parameters based on thermal analysis have been created to quantify the GFA of alloy systems.

Figure 3 presents characteristic temperatures that can be obtained from thermal analysis measurements of an amorphous alloy. The thermal analyses can provide the glass transition (T_g), crystallization (T_x), solidus (T_s), and liquidus temperatures (T_l). The most common parameters used to assess GFA have been the reduced glass transition temperature [54], the supercooled liquid region [55], and the gamma parameter [56]. The reduced glass transition temperature (T_{rg}) is defined by the following expression

$$T_{rg} = {T_g}/{T_l} \tag{2.1}$$

High values (approaching unity) of T_{rg} imply high GFA. A low value of T_l and a high value of T_g increases the probability of cooling through the region without inducing crystallization [57]. The supercooled liquid region (ΔT_{xg}) [55] is expressed as

$$\Delta T_{xg} = T_x - T_g \tag{2.2}$$

Larger values of ΔT_{xg} generally correspond to higher GFA. The larger the supercooled region the greater the tendency of the glass to resist devitrification when heated [58]. The gamma parameter (γ), which is given below

$$\gamma = \frac{T_x}{T_g + T_l}, \tag{2.3}$$

has also been introduced as a measure of GFA with larger values signifying better GFA. The gamma parameter [56] combines T_{rg} and a weighted expression of the super-cooled region ($\Delta T_{xg}/T_g$).

Inoue's three empirical rules intrinsically stress the importance of the composition on the GFA of an alloy. However, even a composition with high GFA can be adversely affected by the presence of impurities in the alloy melt. In particular, oxygen contamination of the alloy has been shown to negatively affect the GFA [59-62]. Murty et al. [63], for instance, investigated the thermal properties of $Zr_{65-x}Cu_{27.5}Al_{7.5}O_x$ (x = 0.14%, 0.43%, and 0.82%) amorphous alloys. An increase in oxygen from 0.14% to 0.82% was accompanied by a significant decrease in ΔT_{xg} from 79 to 57^oC. Oxygen contamination of the molten melt can also increase the critical-cooling rate by promoting heterogeneous nucleation [60]. Higher critical-cooling rates make it more difficult to form a completely amorphous sample. Liu et al. [64] demonstrated that microalloying the $Zr_{52.5}Cu_{17.9}Ni_{14.6}Al_{10}Ti_5$ (atomic, at., %) BMG with B and Si was effective in counteracting the detrimental effects of oxygen on the GFA and thermal stability.

2.3. Relevance of Zr-based Bulk Metallic Glasses (BMGs)

The ability to fabricate amorphous alloys of larger diameters has made the quantification of physical and mechanical properties possible [65]. As demonstrated in Figure 2, Zr-based BMGs have low critical-cooling rates; therefore, many can be fabricated by conventional melting and casting techniques. These alloys have also been shown to possess mechanical properties that make them attractive for structural and other applications [3, 65, 66]. Some of the unique properties exhibited by Zr-based BMGs are high GFA [51, 67-69], near-net-shape formability [65, 66], high strength-to-weight ratios

[65], high strengths [3, 66], high fatigue strengths [3, 8, 9, 70], high elastic strains [69, 71], and low Young's moduli [7, 66]. Figure 4 presents a comparison of the mechanical properties of various BMG systems compared with conventional crystalline alloys. The fatigue-endurance limits of some Zr-based BMGs are comparable or higher than those of some crystalline alloys (Figure 5) [9]. Due to their high fatigue strength, Zr-based BMGs are currently being used in sporting goods such as golf clubs and tennis racquets. They are also being considered for biomedical applications (e.g., surgical tools and implant components) and hinge components for cellular phones. The prospect of biomedical applications for Zr-based BMGs has increased interest in their corrosion resistance [72-78].

2.4. Corrosion Behavior of Zr-based Metallic Glasses and Bulk Metallic Glasses (BMGs)

Gebert et al. [11] performed the first electrochemical investigation of a Zr-based BMG. The study examined the cyclic-polarization behavior of the $Zr_{55}Cu_{30}Al_{10}Ni_5$ (at. %) BMG in nitrogen-purged Na_2SO_4 and NaOH and its localized corrosion behavior in nitrogen-purged NaCl. The BMG was immune to pitting corrosion in the Na_2SO_4 and NaOH solutions. However, a chloride concentration of 10^{-3} M resulted in pitting corrosion. A scanning electron microscope (SEM) image, Figure 6, revealed a pit that was generated at a small crystalline inclusion (~ 4 μm) on $Zr_{55}Cu_{30}Al_{10}Ni_5$. The phase boundary between the amorphous matrix and the dendrite was believed to have a detrimental effect on the localized corrosion resistance. This was compared to the sometime negative effects of grain boundaries on the corrosion behavior of polycrystalline materials. Two possible explanations were given for the pitting corrosion:

(1) a composition change of the bulk alloy or the passive film in the transition zone or (2) formation of crevices due to stresses in the transition zone. This analysis furthered the idea that crystalline inclusions were the key to understanding localized corrosion in amorphous alloys. The crystalline inclusions that have been observed in Zr-based BMGs are believed to be the result of heterogeneous nucleation caused by the presence of impurities in the molten alloy [3, 11, 64]. Figure 7a is an optical micrograph exhibiting the "swirl" regions commonly observed on a polished and etched specimen of the $Zr_{52.5}Cu_{17.9}Ni_{14.6}Al_{10}Ti_{5.0}$ BMG (Vitreloy 105). Peter et al. [27] stated that the spiral regions were areas of crystallinity located just inside the circumference of the ingots and were comprised of microstarlets (Figure 7b). Star-shaped dendrites were observed by Eckert et al. [79] for the as-cast glass-matrix composite with the nominal composition of $Zr_{63}Ti_5Nb_2Cu_{15.8}Ni_{6.3}Al_{7.9}$.

2.4.1. The Effect of Structure on the Corrosion Behavior of Metallic Glasses and Bulk Metallic Glasses (BMGs)

Attempts to gain more information on the possible relationship between crystalline inclusions and the corrosion behavior have been approached in the literature primarily in one of two ways: (1) comparing the corrosion behavior of a fully amorphous alloy to that of an amorphous alloy with some regions of crystallinity or (2) comparing the corrosion behavior of an amorphous alloy to its crystalline counterpart. Various studies have reported deteriorated electrochemical behavior of partially devitrified amorphous alloys [80-82]. For instance, Dutta et al. [83] examined the corrosion behaviors of the wheel and air sides of $Zr_{76}Ni_{16}Fe_8$ melt spun ribbons in chloride environments (10^{-2} N HCl and 1 M NaCl). X-ray diffraction (XRD) revealed crystalline

phases in the air side of the ribbon. The anodic-polarization behavior of the air side surface was worse than the wheel side surface as demonstrated by its higher anodic current densities.

Mehmood et al. [23] examined the anodic polarization behaviors of sputter deposited Cr-60Zr and Cr-67Zr alloys. The two alloys were heat-treated at temperatures of 673, 773, 873, and 973 K for 30 minutes to induce crystallinity. XRD patterns revealed crystalline peaks for the Cr-60Zr samples heat-treated at 773 K and above. Crystalline peaks were observed in the diffraction patterns of all the Cr-67Zr samples that had been heat-treated. The initial crystalline phase was hexagonal close packed corresponding to zirconium and with longer heat treatments the amorphous matrix approached the composition of a Cr_2Zr intermetallic compound with the crystallite size increasing with temperature. The pitting potential (E_{pit}) of Cr-60Zr increased with the heat-treatment temperature in spite of the presence of crystalline inclusions. However, the E_{pit} of Cr-67Zr only increased with the heat-treatment temperature up until 773 K and decreased when the alloy was heat-treated to 873 K. The initial formation of the hexagonal close packed (HCP) phase led to chromium enrichment of the matrix, which yielded a more protective passive film. Decreases in the pitting potential were a result of zirconium precipitates reaching a critical size (> 20 nm) where they could no longer be covered by the protective passive film.

On the other hand, there are some cases when partial devitrification has little effect on the electrochemical behavior or is even beneficial [84-86]. Köster et al. [14] investigated the salt spray and polarization behavior of amorphous and nanocrystalline $Zr_{69.5}Cu_{12}Ni_{11}Al_{7.5}$ ribbons in 10^{-1} N NaOH electrolytes. The authors concluded that there

was not much difference between the corrosion behavior of amorphous and nanocrystalline $Zr_{69.5}Cu_{12}Ni_{11}Al_{7.5}$ ribbons when subjected to salt spray tests. The nanocrystalline sample was described as exhibiting a slightly higher corrosion resistance when compared to the amorphous sample. With regards to the polarization behavior, both the amorphous and the nanocrystalline ribbons were passivated at their corrosion potentials [~ -441 and -491 mV, SCE (standard calomel electrode), respectively]. Increasing the potential eventually led to sharp surges in the current density. The authors did not mention whether this increase in current density corresponded to a pitting potential or a transpassive potential. There was little difference between the polarization behaviors of the amorphous and nanocrystalline ribbons. However, the amorphous ribbon did have a slightly lower passive current density.

Mondal et al. [87] observed the polarization behavior of amorphous and nanoquasicrystalline $Zr_{70}Pd_{30}$ and $Zr_{80}Pt_{20}$ alloy ribbons in NaCl, H_2SO_4, and NaOH electrolytes. Polarization experiments were performed on melt-spun $Zr_{70}Pd_{30}$ ribbons (wheel speed 20 m/s) that had been annealed at 623 K for 30 minutes and 698 K for 15 and 90 minutes. $Zr_{80}Pt_{20}$ ribbons were annealed at 623 K for 30 minutes. The authors found the completely nanocrystalline ribbons of $Zr_{70}Pd_{30}$ and $Zr_{80}Pt_{20}$ were more corrosion resistant than amorphous or partially quasicrystalline ribbons in NaCl. However, an amorphous ribbon had better corrosion resistance than a mixture of amorphous and nanoquasicrystalline phases in NaCl.

Park et al. [88] investigated the corrosion behavior of various sputter-deposited $Mo_{(100-X)}Zr_X$ (X = 27, 35, 40, 50, 60, 73, 80, and 88, atomic percent, at. %) alloys in 12 M HCl. For comparison sputter-deposited Mo and Zr were also examined. Alloys

containing between 40 and 80 at. % of Zr had diffuse halo x-ray patterns characteristic of amorphous materials. Both diffraction patterns of $Mo_{73}Zr_{27}$ and $Mo_{65}Zr_{35}$ indicated a mixture of an amorphous phase and the body-centered cubic (BCC) molybdenum phase. The structure of the $Mo_{12}Zr_{88}$ alloy was found to be a mixture of an amorphous phase and the HCP zirconium phase. Sputter-deposited Zr had the highest corrosion rate [1.03×10^{-1} mm/y (mmpy)] followed by sputter deposited Mo (3.9×10^{-3} mmpy). All of the Mo-Zr alloys, regardless of structure, exhibited corrosion rates lower than sputter deposited Zr and Mo in the 12 M HCl electrolyte. $Mo_{12}Zr_{88}$ had the lowest corrosion rate (~ 5.0×10^{-4} mmpy) in spite of its mixed structure. The anodic-polarization results illustrated that all the Mo-Zr alloys were spontaneously passive at open-circuit conditions and were passivated to potentials higher than 1.3 V, SCE. The zirconium-rich alloys ($\geq$ 60 at. %) had lower anodic current densities than molybdenum and zirconium with current densities decreasing with zirconium additions.

Regarding the second approach, there have been several studies examining the corrosion behavior of Zr-based amorphous alloys and their crystalline counterparts. It is worth mentioning that in order to observe the effect of structural disorder the amorphous alloy should be compared to its single phased crystalline counterpart [89]. If the crystalline alloy has more than one phase, a galvanic effect become more likely [23, 90], and the analysis must include the consideration of a galvanic effect in addition to the structural-order effect. This aspect is not always emphasized in the literature. Dey et al. [91] studied the corrosion rates of amorphous and crystalline $Zr_{67}Ni_{33}$ alloys in 1 N HCl, 1 N H_2SO_4, and 1 N HNO_3. In all solutions, crystalline $Zr_{67}Ni_{33}$ had higher corrosion rates.

Naka and coworkers [92] performed immersion and polarization experiments on amorphous and crystalline $Zr_{50}Cu_{50}$ ribbons in various solutions including 3% NaCl and found the amorphous ribbon to be more corrosion resistant. Peter et al. [27] studied the polarization behavior of the $Zr_{52.5}Cu_{17.9}Ni_{14.6}Al_{10.0}Ti_{5.0}$ BMG and its crystalline form in 0.6 M NaCl. Both the BMG and crystalline state were passivated at their corrosion potentials (E_{corr}) (-257 and -252 mV, SCE, respectively) and exhibited low corrosion current densities. Eventually, pitting corrosion occurred when samples were polarized to their critical pitting potentials (E_{pit}). The mean E_{pit} values for the BMG and the crystalline alloy were 61 and 32 mV, SCE, respectively.

Schroeder et al. [25] examined the polarization behavior of the $Zr_{41.2}Ti_{13.8}Cu_{12.5}Ni_{10}Be_{22.5}$ BMG and its crystallized form in NaCl and $NaClO_4$ electrolytes. The average E_{corr} and E_{pit} values in NaCl were -205 and 2 mV, SCE, respectively, for the $Zr_{41.2}Ti_{13.8}Cu_{12.5}Ni_{10}Be_{22.5}$ BMG and -316 and -227 mV, SCE, respectively, for its crystallized form. In the $NaClO_4$ solution, the average E_{corr} values for the BMG and the crystalline alloy were -265 and -290 mV, SCE, respectively. Neither of the alloys was passivated in $NaClO_4$ and there was little difference in the anodic current densities. From the $NaClO_4$ results, the authors concluded that an amorphous structure did not significantly improve the general and localized corrosion resistance $Zr_{41.2}Ti_{13.8}Cu_{12.5}Ni_{10}Be_{22.5}$.

Though there are many studies that support superior corrosion (i.e., general and/or localized) resistance of amorphous alloys and BMGs over their crystalline counterparts, this is not always the case. Polarization experiments were performed on amorphous and crystalline $Cu_{45}Zr_{55}$, $Cu_{50}Zr_{50}$, and $Cu_{60}Zr_{40}$ alloys by Bala and Szymura [93]. Argon

saturated 1 N solutions of H_2SO_4, HCl, and Na_2SO_4 served as the electrolytes for polarization tests. The authors reported no significant structural effect in the 1 N H_2SO_4. However, crystalline $Cu_{50}Zr_{50}$ and $Cu_{60}Zr_{40}$ alloys were more resistant to localized and general corrosion than the amorphous alloys in 1 N HCl.

2.4.2. The Effect of Composition on the Corrosion Behavior of Metallic Glasses and Bulk Metallic Glasses (BMGs)

It is clear that the "lack of structure" of amorphous alloys can affect the corrosion behavior; however, the composition may be a more significant factor [89]. The differences observed between the electrochemical behaviors as a consequence of structure are generally less pronounced than the differences due to changes in the composition. Various reports have shown that changes in composition (sometimes even less than 5 at. %) can markedly alter the general and/or localized corrosion behavior [19, 22, 74, 94-102]. Since BMGs are not restricted by solubility limits, there is flexibility with the alloy design [26]. However, altering the composition must be balanced with maintain a glass-forming alloy. Many investigations have focused on reporting the role of composition on the corrosion behavior of Zr-based BMGs. Zr-Cu-Al, Zr-Cu-Al-Ni, Zr-Ti-Ni-Cu-Be, and Zr-Cu-Al-Ni-Ti have been the most commonly investigated systems. Liu et al. [99] examined the polarization behavior of $Zr_{65-x}Hf_xCu_{17.5}Ni_{10}Al_{7.5}$ (x = 0 and 1 at. %) BMGs in 0.5 M NaCl electrolytes. The substitution of 1 at. % of Hf drastically improved the pitting resistance of the alloy and increased the pitting potential by more than 550 mV. Hafnium was believed to promote the formation of a stable protective film.

Qiu et al. [74] found that additions of Nb to a Zr-Al-Cu-Ni BMG improved the localized corrosion behavior. The potentiodynamic polarization behaviors of the $Zr_{65-x}Nb_xCu_{17.5}Ni_{10}Al_{7.5}$ (x = 0, 2, and 5 at. %) BMGs were investigated in simulated body fluids (chloride concentration ≈ 0.2 M). The pitting potential was raised by 950 mV with the addition of 5 at. % Nb. Raju and coworkers [22] investigated the effect of additions of up to 5 at. % of Nb and Ti on the polarization behavior a Zr-Cu-Al-Ni BMG in 10^{-2} M NaCl electrolytes. Niobium and Ti were both shown to improve the resistance to localized corrosion as demonstrated by an elevation of E_{pit}. Niobium was found to be more effective than Ti.

Huang et al. [101] examined the anodic polarization behavior of $Zr_{55}Al_{10}Ni_5Cu_{30}$ and $(Zr_{55}Al_{10}Ni_5Cu_{30})_{0.99}Y_1$ BMGs in phosphate buffered saline solutions at 310 K. The $(Zr_{55}Al_{10}Ni_5Cu_{30})_{0.99}Y_1$ BMG had a larger pitting overpotential (E_{pit}-E_{corr}) than the $Zr_{55}Al_{10}Ni_5Cu_{30}$ BMG (446 and 349, mV, respectively) indicating Y improved the resistance to pitting corrosion. Yttrium also improved the general corrosion resistance. The corrosion penetration rate (CPR) of $Zr_{55}Al_{10}Ni_5Cu_{30}$ was 9.9 μm/y compared to 0.6 μm/y for $(Zr_{55}Al_{10}Ni_5Cu_{30})_{0.99}Y_1$. Qin and coworkers [95] observed the polarization behavior of bulk amorphous $Zr_{55}Al_{10}Cu_{30}Ni_{5-x}Pd_x$ (x = 0, 1, 3, and 5 at.%) alloys in 0.6 M solutions and found Pd additions had a detrimental effect. The additions of Pd decreased E_{pit} (1 at.% Pd) or destroyed the passivating abilities (3 and 5 at. %). Figure 8 presents polarization curves of selected Zr-based BMGs [15, 27, 97, 99, 103] from experiments performed in either 0.5 or 0.6 M NaCl electrolytes.

2.4.3. Pitting Mechanisms of Zr-based Metallic Glasses and Bulk Metallic Glasses (BMGs)

The structural and compositional aspects are commonly the subject of published reports on the localized corrosion behavior of Zr-based metallic glasses and BMGs. Less attention has been given to developing detailed descriptions of the possible chemical reactions and processes that accompany the localized corrosion of Zr-based metallic glasses and BMGs. Recently, authors have been giving more consideration to the chemical and microstructural analysis of the corroded surfaces in attempts to provide insight on pitting mechanisms. For instance, the cracked and mottled appearance observed outward from the corrosion pits [90, 101, 102, 104, 105] and the porous or sponge-like (sometimes described as honeycomb) appearance within the corrosion pits [99, 101, 104, 105] on Zr-based metallic glasses and BMGs have been reported in several studies. Mudali et al. [104] described and analyzed this morphology for a pit that formed on the $Zr_{59}Ti_3Cu_{20}Al_{10}Ni_8$ BMG during polarization in a H_2SO_4 solution containing NaCl (Figure 9). Energy dispersive x-ray (EDX) analysis of the cracked and porous regions revealed enrichment of Cu and a depletion of Zr and Al. High levels of oxygen were present in the "bright products" region. Similar findings have been reported by others [101, 105]. After the polarization of $Zr_{58}Cu_{28}Al_{10}Ti_4$ and $Zr_{65}Cu_{7.5}Al_{7.5}Ni_{10}Pd_{10}$ amorphous ribbons in 0.5 M NaCl, Mondal et al. [90] found that a corrosion pit on $Zr_{58}Cu_{28}Al_{10}Ti_4$ was enriched with Cu. While a pit on $Zr_{65}Cu_{7.5}Al_{7.5}Ni_{10}Pd_{10}$ was significantly enriched with Cu and Pd. Lu and coworkers [105] examined the pitting corrosion behavior of Cu-Zr amorphous ribbons in 0.1 M HCl. In addition to observing high levels of Cu in corrosion pits with EDX analysis, XRD of the pits yielded proof of

copper and cupric chloride ($CuCl_2$) on the corroded surface. It was stated that the porous morphology of pits was dependent on the Cu-Zr ratio. Zander et al. [20]performed XRD on $Cu_{46}Zr_{42}Al_7Y_5$ after polarization in a 10^{-2} NaCl solution and Cu and CuO peaks were detected.

Morrison [106] conducted an anodic-polarization study of Vitreloy 105 in 0.6 M NaCl. Polarization experiments were aborted 1-5 mV after the pits began to initiate (i.e., E_{pit}), and subsequently, the surface was examined by SEM. Figure 10a and Figure 10b are the pre-test and post-test micrographs, respectively. Morrison stated the morphology of the pits suggested that initiation may have been caused by inhomogeneities in the amorphous matrix. However, the author did not mention observing inhomogeneities such as crystalline microstarlets on the surface prior to the electrochemical experiments. EDS analyses of pits revealed that they were enriched with Cu and depleted in Zr.

The increased knowledge about the chemistry of corrosion pits has aided in the development of several descriptions of pitting in Cu containing Zr-based amorphous alloys. The descriptions do not concentrate on pit initiation. Rather, it has been assumed that pits initiate due to chloride penetration of weak spots in the passive film. This has been one of the classical approaches to pit initiation with crystalline alloys. However, with amorphous alloys, the weak spots have been either presumed to be a result of crystalline inclusions or not specifically identified. Mondal et al. [90] and Lu et al. [105] explain the enrichment of corrosion pits with Cu (and Pd in the case of Mondal et al.) as a consequence of selective dissolution of the less noble elements (e.g., Zr and Al). The preferential dissolution of the less noble elements is also believed to result in the porous morphology of the pits. Mixing enthalpies of Zr and the other elements in the amorphous

alloy compositions were also used by Mondal et al. to justify the enrichment of corrosion pits with Cu and Pd. Lu et al. [105] asserted that the remaining Cu in the attacked regions rearranges and transforms into a porous CuCl film at higher anodic potentials.

In a review article, Mudali et al. [102] suggested that the mere presence of crystalline inclusions did not provide a sufficient explanation for the poor localized corrosion resistance of Zr-based BMGs, especially when a protective passive film existed. A pitting mechanism was proposed to explain the corrosion behavior of Zr-based BMGs in chloride environments. The authors asserted (based on previous studies) that below the film (predominately ZrO_2 with smaller amounts of Al_2O_3) there is a Cu-enriched layer. The chemical composition of the oxide that forms on Zr-based BMGs due to passivation has been verified in other investigations [18,31-33]. Mudali et al. stated that the presence of the enriched Cu layer rather than a copper oxide is supported by the high Gibbs free energy of formation for copper oxide when compared to the energy of formations of zirconium and aluminum oxides. The diffusion of chloride ions through the oxide film is enhanced by the copper enriched layer. An interaction between the chloride ions and copper layer will yield cupric chloride ($CuCl_2$). Released cupric ions, Cu^{2+}, are believed to polarize the surface and attack weak points on the ZrO_2 film. Cupric chloride causes the pitting attack, and the cracked appearance of corrosion pits is a result of the generation of cupric chloride species at the site. In a recent study on the corrosion behavior of Zr-Ti-Nb-Cu-Ni-Al BMG composites, Gebert et al. [35] emphasized the significance of copper inhomogeneity on the pitting susceptibility.

2.4.4. Summary

The literature on the localized corrosion behavior of Zr-based BMGs has focused on the role of crystalline inclusions and composition. From the reports, it seems that composition has a more dramatic effect on the pitting behavior than that of crystalline inclusions. The effect of crystalline inclusions on the localized corrosion behavior is not clear as evidenced by conflicting corrosion reports. Some reports show that crystallinity may play a role on the general corrosion behavior but not necessarily the pitting corrosion behavior. The contradictory reports may be due to lack of knowledge regarding the induced crystallinity. For example, the composition of the inclusions may be dependent on the composition of the amorphous matrix. Therefore, it is difficult to ascertain whether partial devitrification is always detrimental to the localized corrosion resistance of a BMG. Some efforts have been made to provide a more detailed description of the pitting mechanisms by paying closer attention to the surface chemistry of specific compositions. The interaction between Cu and Cl seems to be an important aspect of the pitting mechanism.

Chapter 3. Theoretical Background

The results presented in Chapter 5 were obtained using various experimental techniques. This chapter provides fundamental information on some of the experimental methods and summaries of their governing principles.

3.1. Atomic Force Microscopy

The atomic force microscope (AFM) belongs to a family of microscopes that is able to provide high-resolution (nanoscale) information about a sample by monitoring interactions between the surface and a sharpened scanning probe. In the case of atomic force microscopy (AFM), the near-field character that is monitored is the interaction force between the probe and sample surface. Figure 11 illustrates the primary components of an AFM. The probe tip is mounted on a cantilever. Piezoelectric elements allow the probe to scan the surface and move in the z direction. Contact mode is a common imaging mode; however, there are various operating modes for the AFM. During contact mode, the distance between the probe and surface is small enough so that a repulsive force is acting on the tip. The repulsive forces experienced as the probe is scanned are related to the surface topography. Due to the small magnitude of the force, the AFM actually measures the deflection of the cantilever. The deflection system consists of a laser beam, which is directed at the back of the cantilever and a four-quadrant photodetector. Initially, the beam is aligned at a position on the cantilever so that its reflection is located at the origin of the photodetector. Changes in the beam position from the origin are used to determine the deflection of the cantilever. The repulsive force is calculated using Hooke's Law

$$F = -kx \tag{3.1}$$

where F is the force, k is the cantilever spring constant, and x is the vertical deflection. The calculated force is then converted to an electrical signal. In contact - constant force operation mode, a feedback mechanism maintains a constant deflection as the probe scans the surface by adjusting the z piezoelectric transducer. The adjustments to maintain a constant deflection (i.e., constant force) represent the topography of the surface.

3.2. Differential Scanning Calorimetry and Differential Thermogravimetric Analysis

Differential scanning calorimetry (DSC) and differential thermogravimetric analysis (DSC-TGA) are thermo-analytical techniques used to determine thermal properties of a sample [107]. From these methods, it is possible to obtain thermal properties such as T_g and T_x. In DSC, a temperature program controls the temperatures of an empty reference pan and a pan containing a sample. The instrumentation ensures that the reference pan and the sample pan are heated at the same rate and maintained at the same temperature. Heat is added to or subtracted from the sample pan in order to make sure its temperature is the same temperature as reference pan. The results of a DSC experiment provide the difference in the heat output of the two pans as a function of increasing temperature. The magnitude of the heat added or subtracted is equivalent to the amount of energy absorbed or released due to a thermal transition [107]. In addition to measuring the difference in the heat output, the DSC-TGA also determines the change in mass of the sample as a function of temperature.

3.3. Polarization Experiments

Polarization experiments provide a means to characterize the aqueous electrochemical behavior of metals and alloys of interest. The pertinent data is obtained

by interfacing an electrochemical cell with a potentiostat. In Figure 12, a standard three-electrode electrochemical cell consisting of counter, working, and reference electrodes in an electrolyte is shown. The counter electrode completes the electrochemical circuit without corroding and contaminating the electrolyte. The potential of the working electrode, the material to be studied, is measured with respect to the reference electrode (a constant potential electrode). During the experiments, the potentiostat controls the potentials of the working electrode while the current response is measured. The corrosion potential (E_{corr}) is the measured potential when the working electrode is not controlled by the potentiostat. This condition is referred to as the open-circuit condition (OCC). The corresponding external current density at the OCC is zero. Cathodic or anodic polarization occurs when the potentiostat imposes potentials more negative or more positive, respectively, than the E_{corr}. The polarity associated with cathodic and anodic polarization is shown in Figure 12. Electrons are supplied to the working electrode during cathodic polarization. This trend means that a net reduction reaction is occurring at the working electrode. During the anodic polarization, electrons are driven from the working electrode. Anodic polarization corresponds to a net oxidation reaction at the working electrode. Oxidation at the working electrode is designated the corrosion reaction because the working electrode is degraded by the following reaction

$$M \rightarrow M^{m+} + me \tag{3.2}$$

where M represents the metal working electrode, M^{m+} is a metal ion that is released into the electrolyte, and *me* are moles of electrons that flow through the circuit. For a specific example, consider the anodic polarization of iron in a deaerated hydrochloric acid electrolyte. The overall reaction can be written as

$$Fe + 2H^+ \rightarrow Fe^{2+} + H_2 \quad (3.3)$$

Equation (3.3) is the sum of the oxidation and reduction half-reactions shown, respectively.

$$Fe \rightarrow Fe^{2+} + 2e \quad (3.4)$$

$$2H^+ + 2e \rightarrow H_2 \quad (3.5)$$

The reduction of hydrogen ions supports the oxidation of iron.

The data obtained from polarization experiments (Figure 13) provides insight on a material's resistance to general and localized corrosion. Potential is the independent variable (and the "driving force" for oxidation) though it is plotted on the ordinate. Several of the parameters that can be determined from the polarization curves are denoted in the figure. Polarization experiments are commenced a few millivolts below the E_{corr} in order to obtain a portion of the cathodic curve. The corrosion potential is identified as the potential at which the current density approaches zero. As the potential is raised above E_{corr} there is a region of almost constant current density. This region corresponds to the formation of a protective film on the sample surface, which hinders the oxidation reaction at the surface and yields low current densities. The low almost constant current density is called the passive current density, i_p. The region where the i_p dominates is designated the passive region. Usually, increasing the potential eventually results in the breakdown of the passive film and a corresponding surge in the current density ensues. If the breakdown of the film is localized, cavities will be present on the surface of the material. In this case, the material is susceptible to pitting (localized) corrosion. Thus, the difference between E_{pit} and E_{corr} can be used to describe a material's resistance to pitting corrosion. Alloys that exhibit the type of polarization behavior described above

are called active-passive alloys. Some materials, however, experience uniform rather than localized corrosion. Figure 14 is a representative polarization curve of a material which undergoes uniform corrosion. The potential and the logarithm of the current have a linear relationship (Tafel behavior). An anodic diffusion current limit is also shown in Figure 14. At a limiting diffusion current density, i_d, the polarization behavior is controlled by the rate of diffusion of metal ions and or corrosion products from the surface. The observation of i_d is possible in materials that exhibit Tafel or passivation behaviors.

In addition to parameters shown in Figure 13 and Figure 14, the uniform corrosion rate under naturally corroding conditions (i.e., at E_{corr}) can be determined from the corrosion current density. The corrosion current density, $i_{corr,}$ is obtained by extrapolative procedures or one of various experimental methods. The corrosion penetration rate, CPR (μm/year), can then be calculated by applying Faraday's Law:

$$\mathrm{CPR} = \frac{0.327 * \mathrm{M} * i_{corr}}{m\rho} \tag{3.6}$$

where M (g/mol) is the atomic mass, i_{corr} (mA/m^2) is the corrosion current density, m is the metal-ion valence, and ρ (g/cm^3) is the density [108].

3.4. Scanning Auger Spectroscopy

In electrochemical corrosion, the dominate concern is the transport of charge across an interface (e.g., a metal/electrolyte interface). Corrosion, therefore, is defined as a surface phenomenon. Techniques that are able to characterize the surface are attractive in corrosion research. Auger electron spectroscopy (AES) allows the semi-quantitative nondestructive determination of the elemental compositions of surfaces, thin films, and interfaces [109]. In addition to providing highly sensitive (~ 0.1 at. %) chemical analysis

of the surface, the ability of AES to characterize films is advantageous since, as discussed previously, the passive film plays a role in protecting the surface from localized corrosion.

The Auger process is a result of the interactions that occur when incident radiation contacts the surface. An incident electron beam strikes the sample surface and ejects a core-level electron resulting in an ionized atom. The core-level vacancy is filled by an outer-level electron. Subsequently, another electron (an Auger electron) is emitted in order to return the ionized atom to its ground state [109, 110]. Thus, the Auger process results in a doubly-ionized atom. The governing equation for the Auger process is given below

$$\mathrm{KE_{Auger}} \approx \mathrm{E_{core}} - \mathrm{E_{outer}} - \mathrm{E_{Auger}} \tag{3.7}$$

where KE_{Auger} is the kinetic energy of the emitted Auger electron, E_{core} is the binding energy of the ejected core-level electron; E_{outer} is the binding energy of the outer electron that fills the core-level vacancy; and E_{Auger} is the binding energy of the emitted Auger electron. Since the KE_{Auger} is related to binding energies, the kinetic energies of Auger electrons provides characteristic peaks in the spectrum, which are used to identify the elements present on the surface. Figure 15 [110] illustrates the Auger process with the ejection of a K electron, an internal transition of a $L_{2,3}$ electron, and the ejection of a $L_{2,3}$ election. Auger electrons have relatively low kinetic energies. Only the Auger electrons from near the surface (a depth of ~100 Å) can escape without being scattered, thus making AES is a reliable surface analysis technique.

AES in conjunction with ion sputtering allows depth profiles of films. An ion-sputter gun removes layers of the surface at a predetermined rate, and subsequently, the

Auger data is collected from each new surface. With the collected information, Auger sputter profiles can be generated. The profiles provide the sample composition as a function of the depth. In addition, individual Auger lineshapes of a particular element can be plotted along with the corresponding sputter cycle. Shifts in the lineshapes can provide limited information about the chemical state of the element. For instance, a shift in a peak as a function of successive sputter cycles can provide insight on if bonding is metal-metal or metal-oxide bonding. The profile data along with the elemental lineshapes can provide information regarding the composition of an oxide film. Reasonable estimates of the film thickness can also be made by taking the sputter rate into account.

Scanning Auger microscopy (SAM) is an attractive technique that combines the capabilities of AES and SEM. The electron beam is scanned across the surface of the sample. When the scanning Auger microscope is operating in its SEM mode, images are obtained by collecting the secondary electrons that are emitted as a result of the beam interaction with the sample surface. SAM can also be used to generate chemical maps of the sample surface. The lateral resolution of SAM is less than 100 Å [109].

Chapter 4. Experimental Methods

4.1. Materials

Samples of the $Zr_{52.5}Cu_{17.9}Al_{10}Ni_{14.6}Ti_{5.0}$ BMG (Vitreloy 105, at. %) were fabricated by arc-melting. Appropriate amounts of Zr, Cu, Al, Ni, and Ti were weighed (± 0.001 g) to obtain 20 g of the raw material. The elements were arc-melted in a Zr-gettered argon atmosphere on a water-cooled copper hearth. To insure adequate mixing, the button of the master alloy was flipped and re-melted five times. Drop-casting of the buttons were performed in a water-cooled cylindrical copper mold. High-purity Zr (99.5 weight, wt., %), Cu (99.999 wt. %), Al (99.999 wt. %), Ni (9 9.9945 wt. %), and Ti (99.99 wt. %) were used to produce Vitreloy 105 ingots of 6.4 mm in diameter.

Specimens of the $Zr_{50}Cu_{30}Al_{10}$ [111-115] and $Zr_{50}Cu_{33}Al_{10}Pd_7$ were provided by Professor Yoshihiko Yokoyama at Tohoku University (Sendai, Japan). The constitutive elements were arc-melted in an argon environment yielding master alloy buttons. Buttons of the $Zr_{50}Cu_{33}Al_{10}Pd_7$ master alloys were then re-melted and cast in cylindrical-copper molds using a tilt-casting apparatus [116, 117]. Cylindrical ingots of $Zr_{50}Cu_{40}Al_{10}$ were obtained using a cap-cast technique [118]. The $Zr_{50}Cu_{40}Al_{10}$ and $Zr_{50}Cu_{33}Al_{10}Pd_7$ ingots were 6 and 8 mm in diameter, respectively. The corrosion behaviors of crystalline elements were also investigated for comparison purposes. High-purity plates of Zr, Cu, Al, Ni, and Ti were obtained from Alfa Aesar.

4.2. Experimental Techniques

4.2.1. X-Ray Diffraction

XRD experiments were performed by a Philips X'pert X-Ray Diffractometer on $Zr_{50}Cu_{40}Al_{10}$, $Zr_{50}Cu_{33}Al_{10}Pd_7$, and Vitreloy 105 to ascertain amorphous structures (within instrumental limitations). The instrument scanned from 2θ values of 20^o to 90^o with a scan rate of 6.6×10^{-3} ^{o}/s.

4.2.2. Differential Scanning Calorimetry

The T_g and T_x for $Zr_{50}Cu_{40}Al_{10}$, $Zr_{50}Cu_{33}Al_{10}Pd_7$, and Vitreloy 105 were determined using a Perkin-Elmer Pyris Diamond Differential Scanning Calorimeter. DSC investigations were conducted in an argon atmosphere. All samples were held for 30 minutes at 323 K, heated from 323 K to 873 K at a rate of 20 K/min, held for 5 minute at 873 K, and then cooled back to 373 K at a rate of 80 K/min.

4.2.3. Differential Thermogravimetric Analysis

The T_l was obtained using a DSC-TGA instrument. Before the experiments, the furnace was allowed to equilibrate to 323 K. The samples were then heated from 323 K to 1523 K at a rate of 20 K/min, held at 1523 K for 3 minutes, and cooled back to 323 K at a rate of 20 K/min.

4.2.4. Laser Treatments

A Lumonics (Rugby, England) pulsed Nd:YAG laser (Model: JK 701) was used to treat Vitreloy 105 in order to induce crystallinity. Five 1 J pulses at a frequency of 20 Hz were applied to the Vitreloy 105 sample. The open shutter time was 3 ms.

4.2.5. Polarization Experiments

All polarization experiments utilized a standard three-electrode electrochemical cell (Figure 12). A platinum counter electrode was employed in the polarization experiments. The reference electrode was a standard calomel reference electrode (SCE). Electrolytes were made by adding appropriate amounts of NaCl to 1930 mL of deionized/distilled water. A pH of 7.0 (± 0.1) was achieved with the addition of a NaOH buffer. The electrolytes in the cell were 0.6, 0.3, or 0.1 M NaCl solutions open to air. All experiments were conducted using an EG&G Princeton Applied Research Model 263A Potentiostat/Galvanostat. The Princeton Applied Research PowerCorr Software was used to record the electrochemical data. Before polarization experiments were commenced, each sample was allowed to stabilize in the electrolyte for 1 h or until the OCC approached the E_{corr}. The E_{corr} was taken as the potential that changed by no more than 1 mV over a 5-minute time span. In order to obtain portions of the cathodic curves, the starting potential was set 15 to 20 mV below E_{corr}. In general, anodic-polarization experiments of the BMGs were either aborted when the current density was approximately 10^{-3} A cm^{-2} or at a potential of 300 mV, SCE. The scan rate was 0.17 mV s^{-1}

Cross sections of $Zr_{50}Cu_{40}Al_{10}$ and $Zr_{50}Cu_{33}Al_{10}Pd_7$ ingots were used as samples for corrosion experiments. $Zr_{52.5}Cu_{17.9}Al_{10}Ni_{14.6}Ti_{5.0}$ samples were obtained by cutting transverse to and along the long axis of the ingot. The working electrodes were constructed in one of two ways. Samples that were only to be used for polarization experiments were mounted in epoxy, and a Cu screw was tapped in back of the mount for an electrical connection. Insulating enamel was used to cover the sample/epoxy interface

in order to protect from crevice corrosion. Samples that were to be examined by SAM after polarization experiments were placed in a Teflon holder where a circular cross section (3 mm in diameter) was exposed. Electrical connection was achieved through a Cu screw tapped in the back of the holder. All samples were polished to a 1200 SiC surface finish.

4.2.6. In-situ Optical Microscopy

Figure 16 illustrates the experimental setup used for the in-situ pitting observation. The container holding the electrochemical cell was placed on the stage of the optical microscope (NIKON, Microphot FX). A three-electrode cell was utilized consisting of a working electrode (the sample), a platinum counter electrode, and a saturated calomel reference electrode (SCE). The electrolyte was a 0.6 M NaCl solution that was open to air (pH = 7.0 ± 0.1). Electrodes were connected to a PARSTAT 2263 potentiostat (Princeton Applied Research). The solution height over the sample was less than 2 mm. The optical microscope was attached to a charge coupled device, CCD, (Hitachi KP MIU), which was connected to a computer with a Scion LG-3 frame grabber. Polarization scans were commenced at potentials below E_{corr} to obtain portions of the cathodic curve. The scan rate was 0.17 mV s^{-1}. Princeton Applied Research PowerCorr Software was used to record the electrochemical data. Images of the specimen surface (600 grit) were captured during polarization scans. The area exposed to the electrolyte was approximately 0.20 cm^2; however, the images are of an area of 0.29 mm^2.

4.2.7. In-situ Atomic Force Microscopy

Electrochemical experiments were performed on Vitreloy 105 samples while the surface was examined with a Digital Images Dimensions V AFM. All samples were

polished to a 1200 grit SiC surface finish. A view of the experimental in-situ AFM set-up is shown in Figure 17. Figure 18 is an image of the sample holder that was designed for the experiments. The sample was inserted into a rectangular channel through the back side of the holder (Figure 18b). A rectangular copper bar with a hole at each end was placed in the channel on top of the sample. Two screws were inserted through the front side of the holder (Figure 18a) through the openings in the bar in order to secure the sample into the channel. The front side of the holder partially exposed three faces of the rectangular sample. An insulating enamel was used to mask the sample so that only a small rectangle (~ 0.06 cm^2) on the top surface was exposed. The counter electrode (platinum foil) was adhered to the bottom of one of the reservoirs. Approximately 40 mL of the 0.6 M NaCl electrolyte was used to fill the reservoirs. The SCE was placed in the same reservoir as the counter electrode. Figure 17b shows an image of the electrochemical cell within the sample holder. The sample, counter electrode, and SCE were interfaced with the potentiostat (Princeton Applied Research PARSTAT® 2263). An optical microscope was used to monitor the position of the AFM probe in relation to the sample.

AFM/electrochemical experiments were performed in DC contact-constant force mode with a SiN probe so that the tip was electrically isolated from the sample. Though the sample area exposed to the electrolyte was approximately 0.06 cm^2, AFM images were limited to 50 μm x 50 μm. The acquisition time for one frame was 640 s. The first frame was always acquired at the OCC (no applied potential). Potentiostatic control of the sample was initiated at subsequent frames. A potential of -190 mV, SCE (~ E_{corr} + 50 mV) was applied to the sample.

4.2.8. Scanning Auger Microscopy

SAM was performed on as-polished and electrochemically corroded $Zr_{50}Cu_{40}Al_{10}$ and $Zr_{50}Cu_{33}Al_{10}Pd_7$ and on as-polished Vitreloy 105 using a Phi Model 680 Scanning Auger Nanoprobe with a primary electron beam of 20 kV, 10 nA, and a diameter of 15 nm. The base operating pressure of the system was 10^{-10} torr. Survey spectra and sputter profiles were taken to elucidate differences in the surface as a function of composition and polarization treatment. Atomic concentrations of elements were calculated using Auger signal intensities normalized with suitable instrumental sensitivity factors. Sputtering was achieved using a 3.5 kV argon ion beam (vacuum pressure of 5 x 10^{-9} torr) and was performed over a 2 mm by 2 mm area. The sputter rate was 0.025 nm/s previously calibrated using a 100 nm Ta_2O_5 standard film. In order to differentiate between oxide and metallic contributions in successive sputter cycles, a linear least squares method was performed on the Auger lineshapes of the constituent elements of the alloys.

Chapter 5. Results

5.1. XRD, Thermal Analysis, and SAM

The diffraction patterns of $Zr_{50}Cu_{40}Al_{10}$, $Zr_{50}Cu_{33}Al_{10}Pd_7$, and Vitreloy 105 are presented in Figure 19. All three alloys exhibited broad peaks characteristic of amorphous materials. Representative DSC and DTA thermograms are shown in Figure 20 and Figure 21, respectively. The T_g, T_x, and T_l of the three BMGs, as determined by DSC and DSC-TGA, are given in Table 1 along with their derived GFA parameters. The T_{rg} and γ parameters of the three BMGs were comparable. Based on these parameters the GFA of the three alloys were similar. However, the differences in the ΔT_{xg} parameters of the BMGs were more pronounced. The $Zr_{50}Cu_{30}Al_{10}$ and Vitreloy 105 BMGs had the highest and lowest ΔT_{xg} values, respectively. Larger ΔT_{xg} values are believed to coincide with increased GFA.

The SAM was used to characterize the as-polished surfaces of $Zr_{50}Cu_{40}Al_{10}$ and $Zr_{50}Cu_{33}Al_{10}Pd_7$. Sputter profiles of as-received $Zr_{50}Cu_{40}Al_{10}$ and $Zr_{50}Cu_{33}Al_{10}Pd_7$ are presented in Figure 22 and Figure 23, respectively. There was not a significant difference between the depth profiles of the two BMGs. Both of the as-received alloys had significant oxygen concentrations at the surface. The presence of metallic oxides on both alloys was verified by shifts in the Auger lineshapes of the metallic elements. Gradual shifts in the peaks with subsequent sputtering corresponded to changes from metal-oxide bonding to metal-metal bonding. Shifts were observed in the Zr (LMM) lineshape from 1842 to 1847 eV and in the Al (LMM) lineshape from 1394 to 1400 eV. These transitions indicated changes from Zr-O to Zr-Zr bonding and Al-O to Al-Al bonding.

Shifts were not detected for the Cu signal in either of the BMGs or for the Pd signal in the $Zr_{50}Cu_{33}Al_{10}Pd_7$ BMG.

Auger maps of the as-polished surfaces $Zr_{50}Cu_{40}Al_{10}$ and Vitreloy 105 were generated. In Figure 24, the SEM image and the corresponding Auger maps of the as-polished surface of $Zr_{50}Cu_{40}Al_{10}$ are presented. The line and other areas denoted on the SEM image were remnants of the carbon stain that was deposited on the surface as the sample sat in the chamber and the beam rastered the surface. Sputtering of the surface removed much of the stain. These areas were verified with the C Auger map. The areas appear as dark regions in the Zr, Cu, and combined Auger maps. C-rich regions demonstrate the resolution that could be observed if strong variations existed in the Zr, Cu, or Al maps. Auger maps of Zr and Cu did not show any strong variations. It was unclear from the Al map whether the map illustrated noise or Al-rich areas. However, observation of the combined map did not support the presence of Al-rich areas and affirmed uniformity in composition. In Figure 25, Auger combined maps of an as-polished area of Vitreloy 105 are displayed. These combined maps showed homogeneity in the composition as well.

5.2. Electrochemical Results

5.2.1. Polarization Behavior of $Zr_{50}Cu_{40}Al_{10}$

The anodic-polarization curves of $Zr_{50}Cu_{40}Al_{10}$ in 0.6 and 0.1 M NaCl electrolytes are shown in Figure 26 and Figure 27, respectively. Polarization behaviors of $Zr_{50}Cu_{40}Al_{10}$ in both electrolytes were similar. The anodic behaviors were bilinear with the final slopes (m_2) being less steep than the initial slopes (m_1). The decrease in slope signified that with increasing potential a smaller driving force was needed to induce

corrosion. Though m_1 was greater relative to m_2, it is unlikely that m_1 represents a passive region due to its low value. This point will be addressed in more detail in the following section. Table 2 provides a summary of the mean values of the pertinent corrosion parameters. The mean E_{corr} and m_1 values of $Zr_{50}Cu_{40}Al_{10}$ in 0.1 M NaCl were higher than those from 0.6 M NaCl. The greater mean m_1 value indicated a larger driving potential was needed to increase the current in 0.1 M NaCl. The corrosion rate of the BMG was lower in 0.1 M NaCl.

5.2.1.1. In situ polarization behavior of $Zr_{50}Cu_{40}Al_{10}$

A polarization curve generated for the $Zr_{50}Cu_{40}Al_{10}$ BMG with the in-situ setup (0.6 M NaCl) is shown in Figure 28. At -453 mV, SCE, there is a change in the slope. Further increasing of the applied potential revealed that the anodic curve was dominated by a region of almost constant current density. Dark-field microscopy images captured during the polarization experiment (Figure 29a-d) provided a means to directly observe the surface. The starting time (t = 0 s) marks the commencement of the polarization experiment. The images shown correspond to the times and potentials denoted on the polarization curve. Figure 29a illustrates no observable changes in the surface when an initial cathodic potential, -560 mV, SCE, was applied. The image of the surface at E_{corr}, -512 mV, SCE, (Figure 29b) reveals that $Zr_{50}Cu_{40}Al_{10}$ was susceptible to pitting corrosion at open-circuit conditions with a pit of 15 μm in length being resolved (t = 271 s). Therefore, for the $Zr_{50}Cu_{40}Al_{10}$ BMG, E_{corr} is greater than or equal to E_{pit} ($E_{pit} - E_{corr} < 0$). Further increases in the potential induced the nucleation of more pits on the surface (Figure 29c and d). At the end of the experiment, the surface was covered with a black corrosion product. Since pits were evident at E_{corr}, the initial slope (m_1), mentioned in the

previous section, did not correspond to passivity. In addition, the region of almost constant current density present in Figure 28 can be explained by increased domination of concentration polarization (diffusion controlled polarization) rather than by passivity.

It was first unclear whether the concentration polarization was characteristic behavior of $Zr_{50}Cu_{40}Al_{10}$ in 0.6 M NaCl at higher potentials or a consequence of the small amount of testing electrolyte due to the size constraints of the in-situ setup. This point was considered since limiting current densities, i_d, (other than passive current densities) are not usually significant for anodic-oxidation processes [108, 119]. To elucidate the observations, the curve from the present study was compared to a curve generated during an aerated polarization experiment of $Zr_{50}Cu_{40}Al_{10}$ conducted in a bulk (~ 2000 mL) 0.6 M NaCl electrolyte (gray curve in Figure 28). The comparison polarization curve also exhibited a concentration polarization region indicating that diffusion-controlled polarization was characteristic of the BMG. Concentration polarization dominance was probably a consequence of metal ions passing into solution faster than they could diffuse away from the metal/solution interface.

The same curves shown in Figure 28 are displayed in Figure 30 over a shorter potential range. The bulk curve demonstrated the change in slope (from m_1 to m_2) (defined in Figure 26) at -463 mV, SCE. At -453 mV, SCE, the curve generated in-situ exhibits a change in slope; however, the m_2 slope region was dominated by the onset of diffusion polarization. The i_d was lower (2×10^{-4} A/cm^2) than that of the curve generated in the bulk volume of solution (0.03 A/cm^2). The solution volume influences the i_d in that a larger electrolyte volume allows metal ions to migrate more readily from the metal/solution interface bringing about a larger i_d.

5.2.2 Polarization Behavior of $Zr_{50}Cu_{33}Al_{10}Pd_7$

The polarization behavior of $Zr_{50}Cu_{33}Al_{10}Pd_7$ in 0.6 M NaCl is shown in Figure 31. It is evident from the curves that the anodic behavior varied considerably. Some of the curves exhibited a slight change in slope similar to that observed in the polarization behavior of $Zr_{50}Cu_{40}Al_{10}$. This change was not as consistent or pronounced. In general, initial slopes (m_1) were shallow suggesting that the alloy offered little resistance to corrosion. Pits were observed on the surface after all of the polarization experiments. In some cases, pits (that were visible to the eye) formed on the surface at open-circuit conditions. Figure 32 is a plot of the open-circuit potential versus time. Oscillations in the potential were observed, which is typically associated with pit initiation and repassivation [108]. The open-circuit potential did not readily stabilize. Summary of the corrosion parameters are given in Table 3.

5.2.3 Polarization Behavior of Vitreloy 105

Figure 33 - Figure 36 are plots of the anodic-polarization behavior of Vitreloy 105 in electrolytes with varying chloride concentrations. In the 0.6, 0.3, 0.1 M NaCl electrolytes, the polarization behaviors of Vitreloy 105 exhibited similar trends. After the software scanned through E_{corr}, the curves exhibited passive regions. Eventually, the curves illustrated sharp rises in the current corresponding to the breakdown of the passive film and the formation of pits. After the plateau, a region where the polarization was diffusion controlled dominated (shown in Figure 32). Figure 37 - Figure 41 illustrate the effect of the chloride concentration on the corrosion parameters. The error bars correspond to 95% confidence intervals. Lower confidence intervals were omitted when the lower bound value had no physical meaning (for instance, negative values of i_p, i_{corr},

and CPR). The passive current density, i_p, was defined as the current density that corresponded to the midpoint potential between E_{corr} and E_{pit}. Lowering the chloride ion concentration had the most definitive effect on the mean values i_p, i_{corr}, and CPR. These parameters decreased with the chloride concentration. Thus, decreasing the chloride concentration shifted the polarization curves to lower current densities. The relationships, however, between the chloride concentration and E_{corr} and $E_{pit} - E_{corr}$ were more complicated. The highest (-252 mV, SCE) and lowest (-282 mV, SCE) mean values of E_{corr} corresponded to chloride concentrations of 0.6 and 0.3 M, respectively. As expected, alloys tested in 0.6 M NaCl were found to be the most vulnerable to pitting corrosion, as demonstrated by having the lowest mean $E_{pit} - E_{corr}$ (265 mV). On average, experiments in the intermediate chloride environment (0.3 M) proved to be most resistant to localized corrosion ($E_{pit} - E_{corr}$ = 554 mV). It is worth noting that this average $E_{pit} - E_{corr}$ was strongly influenced by scan 4, which had a $E_{pit} - E_{corr}$ value of 1484 mV. As demonstrated in Figure 38, the value is well outside of the upper confidence interval. It was not excluded because there was no experimental reason that supported dismissing the experiment. However, the mean calculated (367 mV) without the outlier was still greater than the average $E_{pit} - E_{corr}$ value for a chloride concentration of 0.6 M but only slightly greater than the mean value for a chloride concentration of 0.1 M (348 mV).

5.2.4. Polarization Behavior of Laser-treated Vitreloy 105

The samples used for these experiments were surfaces parallel to the long axes of the ingots. This was done to ensure a large enough area to allow the laser beam to be positioned at the center of the sample. However, in the longitudinal direction, "swirl" patterns were visible to the eye. Optical micrographs (Figure 42) show these regions.

The purpose of the laser treatment was to induce crystallinity (i.e., to cause heterogeneities). The laser treated sample also had these intrinsic inhomogeneities. Since the samples already had regions of inhomogeneity, i.e. swirls, only one laser treated sample was tested. The polarization curves of are shown in Figure 43. Surprisingly, none of the samples were susceptible to localized corrosion for the potential range tested. Due to the significant difference between scan 1 and 2, the third experiment was performed on the same sample that was used in scan 2 in order to check reproducibility. The laser treated sample (scan 4) actually was polarized to 1600 mV without pit initiation. The mean CPR for the experiments was 30 μm/yr.

5.2.5. Electrochemical-AFM Results

Some of the resulting AFM topographic images that were acquired while a potential of -190 mV, SCE was applied to the surface are shown in Figure 44. The area that was exposed to the electrolyte (2 mm by 3 mm) was chosen because inhomogeneities (the spiral features) were visible to the eye. Only an area 50 μm by 50 μm was probed by the AFM. Figure 44a is the topographical map of the surface while in the electrolyte without a potential being applied. Approximately 21 minutes elapsed between each image shown. In Figure 44a, the frame acquired at open-circuit conditions show areas of considerably higher topography. At first, the overall height of the surface increased as the potential was applied. However, there was then a decrease in surface height. This fact is clearly conveyed in the profiles shown in Figure 45. The path of the profile is denoted by the dashed line marked on Figure 44a. The profiles increase in height up to profile t_7, which was shown to be lower than t_5. Examination of profile t_6 (not shown) revealed that it was lower than t_5 but greater than t_7. Therefore, a decrease in topography

occurs after frame 5. The profile associated with the final frame, t_8, increased and was comparable to profile t_5. In this experiment, pit initiation was not captured in the probed area. The OM, however, did capture pitting of areas of the surface that were not probed by the AFM. Pits were visible on the surface after the potential had been applied for 37 minutes.

5.2.6. Polarization behavior of Crystalline Constituents

For comparison, the polarization behaviors of the crystalline constituents of $Zr_{50}Cu_{40}Al_{10,}$ and Vitreloy 105 were investigated. Representative polarization curves of Zr, Cu, Al, Ni, and Ti that were generated in 0.6 M NaCl are shown in Figure 46 and Figure 47. Ti exhibited good passivation with a i_p of about 2×10^{-6} A cm^{-2}. The surface of Ti was passivated up to 1600 mV, SCE, and breakdown did not occur. Zr, Al, and Ni were susceptible to localized corrosion in 0.6 M NaCl with Zr exhibiting a higher resistance to localized corrosion. Zr was passivated at E_{corr}; however, subsequent increases in the potential resulted in pitting corrosion at 194 mV, SCE. Al exhibited an E_{corr} value significantly lower than the other elements but like Zr was passivated at open-circuit conditions. Breakdown of the passive film eventually occurred at -759 mV, SCE. Ni did not exhibit a clear defined passive region; however, pits were observed on the surface after polarization. Thus, the pitting potential is either less than or equal to E_{corr}. The representative polarization curve of Cu had a similar shape to that of Ni. Nevertheless, pits were not observed on the surface of Cu after the polarization experiment. The surface was degraded by general corrosion (that is, uniform corrosion of the surface). A light green corrosion product covered the surface of Cu after the experiment.

5.3. Surface Examination (OM, SEM, SAM, and XRD) of Corroded Surfaces

5.3.1. $Zr_{50}Cu_{40}Al_{10}$

Figure 48 is a scanning electron microscopy (SEM) image of the corroded region on the surface of $Zr_{50}Cu_{40}Al_{10}$. The localized attack occurred in the vicinity of the insulating enamel/sample interface at open-circuit conditions (that is, without applying a potential) in a 0.6 M NaCl electrolyte. Figure 49 shows the perimeter of the corroded region at a higher magnification. In general, the corroded area had a rough and "cracked" appearance. Pits had an irregular shape rather than the more common hemispherical morphology. The localized corrosion was associated with a dendritic structure (denoted with circles). Some of the dendrites seemed to be raised from the surface. Protrusions were observed from some pits. SEM images of the surface of $Zr_{50}Cu_{40}Al_{10}$ after polarization experiment in a 0.1 M NaCl electrolyte are shown in Figure 50 and Figure 51. There are features similar to those seen in Figure 49. However, the extent of the corrosion was more severe since the sample was potentiostaically controlled. Figure 50 illustrates light particles and irregular pits on the surface. Some features on the surface of seemed to be raised. However, from Figure 50a it is unclear whether the raised area is on something that is on top of the surface. Figure 50b is a higher magnification SEM image of the surface. In this micrograph, an area of higher topography due to the build up of particles underneath the surface is shown. These particles were also observed on top of the surface. The cracked regions detected on the surface may be a result stresses from corrosion products forming under the surface. Protrusions from of pitted areas were also observed on the surface (Figure 51).

Some portions of the surface were almost completely covered by the particles (Figure 52a). Examination of Figure 52a revealed three distinct regions (or layers) on the corrosion surface. Energy dispersive x-ray spectroscopy (EDS) analyses were performed on the three layers. The blue rectangle (layer 1) was the original surface. This conclusion seemed reasonable since the original grinding marks were apparent. The red rectangle (layer 2) corresponds to an area with many particles. Layer 3 denoted by the green rectangle was the layer atop the as-polished surface. This layer was probably the same as the elevated structure observed in Figure 50a. It is clear that the elevation is due to something that grew on the surface (rather than underneath it). According to the EDS results, the region within the green rectangle had much higher levels of oxygen than the other two regions and is probably a zirconium oxide. When the atomic concentration for the region in the blue rectangle was calculated ignoring the oxygen, the atomic percentages of Zr, Cu, and Al were 51, 39, and 10, respectively. The same analysis was performed on the region in the red rectangle and resulted in atomic percentages of Zr, Cu, and Al of 49, 43, and 8, respectively. Visibility of grind marks and the close agreement with the nominal composition support that the area within the blue rectangle is the as-polished surface. The composition of the light particles is also close to the nominal composition. However, it is unlikely they were particles broken off from the original as-polished surface especially since in Figure 50b they were observed coming out from beneath the original surface. The particles are also seen growing underneath the oxide later (red arrow).

A SEM image of a highly pitted region on $Zr_{50}Cu_{40}Al_{10}$ is provided in Figure 53 (top left). SAM was used to examine to the sample after it had been polarized in an

aerated 0.6 M NaCl electrolyte to approximately 300 mV, SCE. Figure 53 (top right) shows the corresponding color-combined Auger map for the area presented in the micrograph. The map shows Cu (red), O (green), and Cl (blue) and was compiled prior to sputtering. The color map and the grey scale map (bottom of Figure 53) illustrate an enrichment of Cu and depletion of Zr within pits when compared to the bulk surface. Pitted areas on the color map are purple indicating that they are associated with Cu and Cl. Auger spot analysis revealed areas highly enriched with Cu and Cl were depleted in Al.

Auger analysis was also performed on the corroded surface of $Zr_{50}Cu_{40}Al_{10}$ subsequent to sputter etching. Auger maps (Figure 54) were obtained of C, O, Cu, Zr, and Cl. Carbon signals were low in most areas illustrating that sputtering removed the majority of the surface impurities. Oxygen was not associated with the flat surface, but Cu and Zr were observed in this region. Thus, the sputter etching was able to remove the oxide over the flat (non-pitted) areas and uncover the bulk composition. The heavily corroded portion, however, was depleted of Zr and enriched with Cu and O. The oxide over the corroded region seems to be an effect of the corrosion process and different from the oxide which previously covered the flat regions. However, within this region, areas that exhibited very high concentrations of Cu (very bright areas) were depleted in O and Cl.

Auger spectroscopy provides limited information about chemical species; therefore, x-ray diffraction was performed on $Zr_{50}Cu_{40}Al_{10}$ two electrochemically treated samples. One sample was polarized in a 0.1 M NaCl electrolyte to a maximum anodic potential of -377 mV, SCE. The other sample was polarized to an anodic potential of 300

mV, SCE in a 0.6 M NaCl electrolyte. The XRD plots of polarized $Zr_{50}Cu_{40}Al_{10}$ samples (both mounted in epoxy) are presented in Figure 55. At 20^{o}, the amorphous peaks observed are due to the epoxy mounts. The pattern of the less aggressive electrochemical treatment (polarized to -377 mV) revealed no effects of polarization even though particles were observed on the corroded surface (Figure 52). However, the diffraction pattern of the sample polarized to 300 mV, SCE displayed peaks that verified the presence of crystalline Cu on the corroded surface.

5.3.2. $Zr_{50}Cu_{33}Al_{10}Pd_7$

Figure 56 is a SEM photomicrograph of the corroded surface of $Zr_{50}Cu_{33}Al_{10}Pd_7$ after being exposed to a 0.3 M NaCl electrolyte. A magnified view of the area outlined in Figure 56 is shown in Figure 57a. Figure 57b reveals 3 distinct regions that were similar to the regions identified on corroded $Zr_{50}Cu_{40}Al_{10}$ samples (Figure 52a). The first region (layer 1) is the original polished surface as evidenced by the grinding features. The layer directly above the original surface is designated as layer 2. This region is characterized by a rough cracked appearance. In addition, particles are beneath the surface of layer 2. The third region (layer 3) seemed to have broken off from the top of layer 2. Figure 58a illustrates an area of severe localized corrosion. The magnified view of the area outlined by the purple rectangle presented in Figure 58b provided more detail of layers 1 and 2. Layer 1 had a definite dendritic pattern. EDS analyses of layers 1 and 2 are summarized in Figure 59. Again, the chemistry of layer 1 is similar to the nominal composition while layer 2 has high concentrations of O, Zr, and Cu. Figure 60 is an optical micrograph of a severely corroded area. The micrograph contained three colors (rust, green, and white) which may be related the layers that were mentioned previously.

Also, channels in the micrograph are characteristic of localized corrosion due to exposure to chloride ions.

Figure 61 shows a small pit on the surface of the $Zr_{50}Cu_{33}Al_{10}Pd_7$ BMG that had been polarized in a 0.6 M NaCl electrolyte. The polarization experiment performed on this particular $Zr_{50}Cu_{33}Al_{10}Pd_7$ sample was aborted prematurely (-274 mV, SCE), that is, before the limiting diffusion current region. This was done so that the surface would not be heavily corroded, and pits could be investigated in their early stages. The numbers in Figure 61 correspond to points where survey spectra were taken (prior to sputtering). Concentrations from the survey spectra are presented in the Table 4. The data shows that points within the pit (positions 1, 2, and 3) were depleted in Zr and Al when compared to the surface (position 4). In addition, Cl was not detected on the surface but was heavily concentrated in the pit. Palladium was not observed on the surface but was observed in the pit. Most importantly, the Auger data reveals the presence of compound containing Cu and Cl (position 3). Positions 1 and 3 showed small amounts of Na. The high Cl to Na ratio makes it unlikely that the chlorine is due to NaCl crystals. Auger maps of the pit shown in Figure 61 are presented in Figure 62. The Auger maps highlight the findings of the position survey spectra.

5.3.3. Vitreloy 105

SEM was used to examine the surface of a cross-sectional sample of Vitreloy 105 after an experiment was aborted less than 5 mV after E_{pit}. Figure 63a is a photomicrograph of the pit on the surface of Vitreloy 105. The center of the pit has a "sponge-like"/porous morphology that is different from the smooth appearance of the bottom of the pit. EDS analyses of the area within in the pit (yellow rectangle) and an

area on the surface (blue rectangle) are presented in Figure 63b. The composition of the surface was more consistent with the nominal composition of Vitreloy 105. However, the analysis of the porous area within the pit revealed the area was mainly Cu and O. Figure 64 is a micrograph of a cluster of pits emphasizing changes in the pit morphology. The bottom of some of the corrosion pits had a smoother appearance (red rectangle). EDS analyses (Figure 65 and Figure 66) were performed on these areas and compared to the elemental analysis of the sponge-like morphology. The results reveal that the chemistry within corrosion pits varied. There was significant difference between the chemical makeup of the bottom of the pit (smoother region) when compared to the sponge-like/porous region. The smoother areas were in closer agreement with the nominal composition of Vitreloy 105. Charging around the pits is from the oxide layer associated with the surface. Furthermore, the EDS analysis was performed on the bright area outlined by the white rectangle in Figure 64. Like the porous region, the bright area was predominately Cu and O, but the ratio of Cu to O was lower.

Chapter 6: Discussion

6.1. Discussion of the Polarization Behavior of $Zr_{50}Cu_{40}Al_{10}$, $Zr_{50}Cu_{33}Al_{10}Pd_7$, Vitreloy 105, and the Crystalline Metals

Little difference was observed between the polarization behaviors of the $Zr_{50}Cu_{40}Al_{10}$ and $Zr_{50}Cu_{33}Al_{10}Pd_7$ BMGs in the NaCl electrolytes. Each alloy exhibited poor anodic-polarization behavior with small increases in the applied potential yielding large increases in the current density. In all experiments, $Zr_{50}Cu_{40}Al_{10}$ was susceptible to localized corrosion at open-circuit conditions. This means that the natural potentials established by the BMG in the electrolytes were sufficient to overcome the threshold for pitting (that is $E_{corr} \geq E_{pit}$). $Zr_{50}Cu_{33}Al_{10}Pd_7$ was vulnerable to localized attack at open-circuit conditions in most cases. Passive film formation was not enhanced by the anodic polarization of either $Zr_{50}Cu_{40}Al_{10}$ or $Zr_{50}Cu_{33}Al_{10}Pd_7$ in any of the NaCl electrolytes. However, intrinsic oxide layers, mainly Zr and Al, on $Zr_{50}Cu_{40}Al_{10}$ and $Zr_{50}Cu_{33}Al_{10}Pd_7$ were observed with AES depth profiling on as-polished samples. The predominance of Zr and Al in the oxide layers can be explained by the low standard free energies of formation of ZrO_2 and Al_2O_3. Table 5 gives the standard Gibbs free energies of formation for several oxides [120, 121]. It has been reported elsewhere that the oxide films of Zr-based BMGs are mainly ZrO_2 and Al_2O_3 [122].

Though the behaviors of $Zr_{50}Cu_{40}Al_{10}$ and $Zr_{50}Cu_{33}Al_{10}Pd_7$ were similar, the polarization curves of $Zr_{50}Cu_{33}Al_{10}Pd_7$ illustrated significant variation while those of $Zr_{50}Cu_{40}Al_{10}$ were more consistent. The mean E_{corr} of $Zr_{50}Cu_{33}Al_{10}Pd_7$ (-326 mV, SCE) was more noble than that of $Zr_{50}Cu_{40}Al_{10}$ (-518 mV, SCE); however, this detail did not translate into increased corrosion resistance. The initial slopes of the polarization curves

of $Zr_{50}Cu_{40}Al_{10}$ tended to be greater than those of $Zr_{50}Cu_{33}Al_{10}Pd_{7.}$ Therefore, compared to $Zr_{50}Cu_{33}Al_{10}Pd_{7,}$ $Zr_{50}Cu_{40}Al_{10}$ was marginally more resistant to corrosion when the potential was increased, which agrees with the study asserting the negative effect of Pd additions [95, 96] on the polarization behavior. Decreasing the chloride concentration from 0.6 to 0.1 M did not significantly alter the localized corrosion behavior of $Zr_{50}Cu_{40}Al_{10}$ (that is, pitting still occurred at E_{corr}). This point was surprising since decreasing the chloride concentration tends to make the electrolyte less aggressive.

The polarization behavior of Vitreloy 105 showed great improvement over the behaviors of $Zr_{50}Cu_{33}Al_{10}Pd_7$ and $Zr_{50}Cu_{40}Al_{10}$. Even in the most aggressive electrolyte, the cross-sectional samples of Vitreloy 105 exhibited passive behavior at E_{corr} and remained passivated as the potential was increased. Eventually, breakdown of the passive film occurred. The Vitreloy 105 samples with the "swirl" regions (the longitudinal samples), had localized corrosion resistance that was far superior to the cross-sectional samples. The longitudinal samples did not pit up to polarization of 300 mV, SCE. Note at 300 mV, SCE, cross-sectional samples of Vitreloy 105 exhibited a current density on the order of 0.1 A/cm^2. At this potential, the longitudinal samples with the worst corrosion resistance (scans 2 and 3) exhibited a current density four magnitudes lower (~ 10^{-3} A/cm^2) than the cross-sectional samples. However, the mean corrosion rate of the longitudinal samples was comparable to that of the cross-sectional samples (30 and 27 um/y, respectively). The superior resistance to localized corrosion of the longitudinal samples of Vitreloy 105 was unexpected since the presence of inclusions was thought increase the likelihood for pitting corrosion. These findings illustrate that inhomogeneities do not necessarily result in susceptibility to localized corrosion. The

Auger maps of Vitreloy 105 did not reveal any chemically distinct regions. However, these experiments were performed on the cross-section of the ingot. At this time the chemistry of these inhomogeneities are not known. These regions are believed to be crystalline inclusions [27]; however, XRD patterns of the surfaces that contained the inclusions did not reveal any crystalline peaks. This discrepancy could be a consequence of inadequate instrument sensitivity. Regardless of the nature of the inclusions, they led to the increased the effectiveness of the passive film. The AFM results illustrating a growth, reduction, and growth on the surface may be related to the behavior of the passive film. The decrease in the surface topography occurred almost an entire frame (~11 minutes) after pits became visible with OM. Thus, the increases and decreases in the surface topography could be related to substantial pit formation and repassivation.

A comparison of the polarization curves of the BMGs with the curves of the crystalline elements provides some explanation for the difference between Vitreloy 105 (both the cross-sectional and longitudinal samples) and the other BMGs.[1] Ti and its alloys are widely recognized as resistant to localized corrosion due to the formation of a tenacious TiO_2 film. The effectiveness of the passive film was exemplified by titanium's polarization curve shown in Figure 47. Even after polarization to 1600 mV, SCE local breakdown of the oxide did not occur. The superior polarization behavior of Vitreloy 105 (compared to $Zr_{50}Cu_{33}Al_{10}Pd_7$ and $Zr_{50}Cu_{40}Al_{10}$) is attributed to the oxide forming ability of Ti. This may explain why Pd, which is less likely to form an oxide (Table 5), was not more beneficial to the localized corrosion resistance. The superior localized

[1] A caveat is warranted since the polarization behaviors of uncoupled elements are compared to BMGs that contains those elements. The thermodynamic parameters that influence the properties of these elements are subject to change when surrounded by atoms of another element. In addition, the structure difference (crystalline versus amorphous) might also lead to changes. However, the difficulty in producing amorphous samples of only one element requires the consideration of crystalline elements.

resistance of Vitreloy 105 was ascribed to Ti and not to Ni. The $Zr_{50}Cu_{30}Al_{10}Ni_{10}$ BMG did show a small passive region when polarized in a 0.6 M NaCl electrolyte [123] (Figure 8). However, it still markedly less resistant to localized corrosion than Vitreloy 105.

6.2. Discussion of the Corroded Surfaces of $Zr_{50}Cu_{40}Al_{10}$, $Zr_{50}Cu_{33}Al_{10}Pd_7$, and Vitreloy 105

Analysis of the corroded surfaces of $Zr_{50}Cu_{40}Al_{10}$ and $Zr_{50}Cu_{33}Al_{10}Pd_7$ revealed the existence of similar features. The exposure of both BMGs to NaCl solutions results in the growth of a substance on the surface. In Figure 52a and Figure 57b, the areas labeled layers 2 and 3 correspond to a corrosion product that developed on the surface. Examination of SEM micrographs suggests that layer 3 is actually on top of layer 2. Two possible explanations for the exposure of layer 2 is (1) the growth of the substance was incomplete or (2) something caused a portion of layer 3 to become unattached leaving layer 2 exposed (see Figure 57b). Though there is evidence that layer 2 is apart of layer 3, EDS analysis uncovered differences in the chemical makeup. Both layers had considerable amounts of O. However, the O to Zr ratio on layer 3 was almost two times higher than that on layer 2 (Figure 52a).

Additional examination of the corroded surface provided evidence that the corrosion behavior of both BMGs was influenced by the presence of crystalline inclusions. Figure 49 and Figure 58b illustrate that the corrosion product developed in a way in which the exposed areas had a dendritic shape. The exposed area was found to be the as-polished surfaces evidenced by the grinding features and EDS analysis. After $Zr_{50}Cu_{40}Al_{10}$ was polarized, little of the as-polished surface was visible. The surface was almost entirely covered by layer 2 or layer 3 (Figure 52a). The as-polished surface (layer

1) was only visible in areas where the corrosion product served as a barrier. Though the corrosion product did preserve some areas of the as-polished surface, it did not have a significant effect on the polarization curve. That is, the growth of the product did not yield a region of decreased current density (small increases in potential still resulted in large increases in the current density). Areas of localized attack had an irregular, cracked appearance and were similar in shape to the dendritic structures shown in Figure 49. These areas of attack seemed to have been areas where the as-polished surface was previously exposed. The cracked appearance was a consequence of the formation of corrosion products underneath the surface (Figure 50b and Figure 51). This type of process is referred to as exfoliation corrosion and is most common to Al alloys.

In general, the morphology of corroded surfaces of $Zr_{50}Cu_{40}Al_{10}$ and $Zr_{50}Cu_{33}Al_{10}Pd_7$ were similar. However, the $Zr_{50}Cu_{33}Al_{10}Pd_7$ sample that was polarized to -274 mV, SCE (Figure 61), did not have the same features described previously (layers 2 and 3 and the dendritic structure). The localized attacked was not irregular but rather hemispherical in shape. The difference in morphology of the corroded samples can be attributed to the varying the polarization behavior of $Zr_{50}Cu_{33}Al_{10}Pd_7$.

The localized attack on Vitreloy 105 (the cross-sectional samples) was markedly different from the attack seen on $Zr_{50}Cu_{40}Al_{10}$ and $Zr_{50}Cu_{33}Al_{10}Pd_7$. There was not any sign of corrosion products that had grown on the surface during the corrosion process. Corrosion pits had a hemispherical shape. The edges of the pits were defined and smooth. Within some pits there was a sponge-like morphology and other regions of the pit had smoother appearance. No microstructural features, such as crystalline inclusions, were observed in the vicinity of pits after the sample was polarized to E_{pit}.

6.3. Discussion of the Chemical Character of the Corroded Surfaces of $Zr_{50}Cu_{40}Al_{10}$, $Zr_{50}Cu_{33}Al_{10}Pd_7$, and Vitreloy 105

Though the electrochemical experiment that preceded the SAM examination of $Zr_{50}Cu_{33}Al_{10}Pd_7$ was less aggressive than the treatment that proceeded $Zr_{50}Cu_{40}Al_{10}$ similar trends were seen in the chemical analyses. In general, the corroded areas of both BMGs were enriched in Cu and Cl and depleted in Zr. Also, high levels of oxygen were associated with areas of attack. The heavily corroded area shown in Figure 54 had a high O concentration, even though the surface had been sputter etched. Interestingly, there were areas within this region that had high concentrations of Cu but low concentration of O and Cl. This suggested that the corroded region may have contained two compounds: (1) a copper oxide and (2) a copper chloride. The extremely bright areas on the Cu Auger maps within the corroded areas did not seem to be related to either of the possible compounds. It is believed that these areas are connected to the crystalline Cu peaks that were identified in the diffraction pattern shown in Figure 55. This finding supported the observation that there was Cu present that was not associated with a compound. No peaks corresponding to an oxide or chloride were present. In addition, it was clear that the crystalline Cu detected was only related to the more aggressive electrochemical treatment since the peaks were not observed when $Zr_{50}Cu_{40}Al_{10}$ was polarized to -377 mV, SCE. However, it should be noted that the less aggressive electrochemical treatment was performed in 0.1 M NaCl rather than 0.6M. This difference is not believed to be significant since the corrosion behavior in both electrolytes was so similar.

The EDS analysis of corrosion pits on Vitreloy 105 also had heighted levels of Cu and O when compared to the surface. No significant amount of Cl was observed within the pits. The chemical makeup was found to be varied within the pit. The porous/honeycomb morphology was almost exclusively Cu (Figure 63). However, the smoother parts of the pits (for instance, the bottom) had a chemical makeup more similar to the nominal composition (Figure 64 and Figure 65).

6.4. Proposed Pitting Mechanisms

6.4.1. $Zr_{50}Cu_{40}Al_{10}$

Exposure of the $Zr_{50}Cu_{40}Al_{10}$ surface to the NaCl electrolyte causes the growth of a corrosion product (an oxide) over certain areas of the surface. More than likely the oxide was primarily ZrO_2 since it is the most stable zirconium oxide [120]. It is unclear the reason that the oxide grows on some areas and not others. Undoubtedly, it is related to crystalline inclusions since the areas not covered have the shape of dendrites. It is possible that areas over which the oxide grew had a composition that was different from the nominal composition. Nevertheless, the presence of both the bare alloy and the oxide caused a galvanic electrode effect. The oxide layer was a sufficient electron conductor to support the reduction of dissolved oxygen

$$O_2 + 2H_2O + 4e \rightarrow 4OH^- \quad (5.1)$$

The reaction above is the dominant cathodic reaction that occurs in aerated near-neutral electrolytes. Areas where the as-polished surface was exposed were anodic in relation to the oxide meaning the potential over these areas were higher. Current travels from the anodic regions to the cathodic regions, since current flows from a higher potential site to a lower potential site. A schematic of the galvanic electrode effect is shown in Figure 67.

This is the same effect that results in the preferential attack of bare steel when the other areas of the alloy are covered with the black magnetite oxide [108]. The governing reactions at the anodic sites are oxidation reactions. At the anodic sites the oxidation reactions were probably

$$Zr \rightarrow Zr^{4+} + 4e \quad (5.2)$$

$$Al \rightarrow Al^{3+} + 3e \quad (5.3)$$

due to the lower standard electrode potentials of Zr and Al when compared to Cu (Table 6) [124]. This assertion is strengthened when the minimum potentials of the experiments are considered (approximately -520 mV, SCE). Since this potential was greater than the standard potentials, net oxidation (loss of electrons) occurred. The preferential dissolution of certain areas would have resulted in occluded areas (pits) with heightened concentration of Zr^{4+} and Al^{3+} ions, which in turn would encourage the migration of Cl^- ions to the pits. It is likely that the Zr^{4+} will tend to hydrolyze by the following reaction

$$Zr^{4+} + H_2O \rightarrow [Zr(OH)]^{3+} + H^+ \quad (5.4)$$

owing to its negative pK_{eq} [- log (equilibrium constant)] of -4.0 [125]. The Zr^{4+} ions can reduce the pH within the pit. The importance of the acidification of the Cu enriched pit becomes clear when the potential-pH equilibrium diagram for the Cu-Cl-H_2O system with a chloride ion concentration of 35,500 ppm (0.6 M) is considered (Figure 68).[2] According to the diagram, in acidic conditions a $CuCl^{-2}$ complex will form and at higher potentials CuCl, cuprous chloride, is stable. As the potential of the experiments was increased, the formation of CuCl within areas of local attack occurred. The high levels of

[2] The potential on the potential-pH equilibrium shown in Figure 68 is relative to the hydrogen reference electrode. The standard calomel electrode (SCE) is +241 mV relative to the hydrogen reference electrode.

Cu and Cl experimental observed are attributed to this highly insoluble compound. According to Figure 68, CuCl is stable at pH values less than 6, but in the presence of neutral water it tends to be hydrolyzed by the reaction below

$$CuCl + H_2O \rightarrow Cu_2O + 2Cl^- + 2H^+ \quad (5.5)$$

This reaction is reflected by Line 51 on the potential-pH diagram. With the large amount of neutral bulk solution available, the hydrolysis of CuCl is reasonable. The reaction above provides one explanation of the high concentrations of Cu, Cl, O that were observed with SAM.

Though the outlined reactions initiate within the pit, they result in autocatalytic processes that eventually cause the deterioration of the entire surface. A higher potentials (pH≈7) the phase thermodynamically predicted for the Cu-Cl-H_2O system was the $3Cu(OH)_2$ $CuCl_2$ compound. However, at a pH of about 7.5, this phase is in equilibrium with CuO.

$$3Cu(OH)_2 \cdot CuCl_2 = 4CuO + 2Cl^- + 2H^+ + H_2O \quad (5.6)$$

After polarization to 300 mV, the surface was covered with a very dark corrosion product. Reaction 5.6 is reasonable since CuO is a black oxide, and it provides a possible explanation for the high amounts of Cu, Cl, and O that were observed by SAM. When polarization was completed, any Cu ions or complexes in the solution would deposit on the surface since they would no longer be stable (potential = E_{corr}). The deposition of Cu on the corroded surface was supported by the crystalline Cu peaks that were observed in the diffraction pattern of a corroded $Zr_{50}Cu_{40}Al_{10}$ sample. This crystalline Cu was

probably the bright areas in the Cu Auger map in Figure 54 that were not associated with O or Cl.

6.4.2. $Zr_{50}Cu_{33}Al_{10}Pd_7$

In general, the observed corrosion behavior of $Zr_{50}Cu_{33}Al_{10}Pd_7$ was very similar to that of $Zr_{50}Cu_{40}Al_{10}$. $Zr_{50}Cu_{33}Al_{10}Pd_7$ also formed an oxide corrosion product on the surface after exposure to NaCl. And like $Zr_{50}Cu_{40}Al_{10}$, the oxide grew so that the exposed as-polished areas were in the shape of dendrites. Due to these similarities, it is assumed that the mechanism described above for $Zr_{50}Cu_{40}Al_{10}$ can also be applied to $Zr_{50}Cu_{33}Al_{10}Pd_7$.

However, one sample when examined did not exhibit the extensive growth of a corrosion product on the surface. The sample showed signs of localized corrosion; however, the pits had the conventional hemispherical shape. Taking into account the variation in the polarization curves, the observation of two different corrosion morphologies was not surprising. The difference in the corrosion morphologies may be related to the presence or absence of a dendritic structure. Growth of the oxide product on the $Zr_{50}Cu_{33}Al_{10}Pd_7$ seemed to relate to a dendritic pattern. This type of pattern was not observed on the corroded surfaces of the sample with the hemispherical pit morphology.

In the case of the sample with the more conventional pit morphology, the pit initiation is assumed to have occurred at weak spots and/or defects in the air formed film. The perimeter of the pit clearly shows the presence of a film. Obviously, the air-formed film was not successful in protecting the surface from localized corrosion as evidenced by the poor polarization behavior of the alloy. Pit initiation is believed to occur at weak

spots and/or defects in the film. This is a common belief and is why pit initiation is commonly treated as a stochastic process. SAM revealed that the hemispherical corrosion pits were depleted in Zr and Al and enriched in Cu and Cl. From this data, it is assumed that the remaining steps in the mechanism were parallel to the corrosion mechanism described for $Zr_{50}Cu_{40}Al_{10}$. Preferential dissolution of Zr and Al due to their lower standard potentials (Table 6 [124]) resulted in pit formation. Next, hydrolysis of Zr^{4+} (equation 5.4) lowered the pH within the pit and enabled the formation of CuCl by the following reaction

$$Cu + Cl^- = CuCl + e \quad (5.7)$$

These steps are bolstered by the SAM findings. The pit in Figure 62 was enriched with Cu and Pd. The E_{corr} value and final potential were -334 and -274 mV, SCE, respectively, for the $Zr_{50}Cu_{33}Al_{10}Pd_7$ sample that was examined by SAM. Within this potential range, the oxidation reactions of Zr and Al were favored resulting in preferential dissolution of Zr and Al. In addition, within the pit, a compound with high amounts of Cl and Cu was discovered.

6.4.3. Vitreloy 105 (cross-sectional samples)

Based on the presented experimental findings, the following steps are proposed to explain the pitting corrosion in the cross-sectional samples of Vitreloy 105 in an aerated 0.6 M NaCl electrolyte. Examining the standard Gibbs free energies of formation it seems possible that the air-formed oxide film on Vitreloy 105 might contain a certain amount of TiO_2 in addition to ZrO_2 and Al_2O_3. The shape of the polarization curves suggests that the intrinsic film forms into a reasonably protective passive film. It is unclear what causes the breakdown of the passive film. However, since the E_{pit} was

affected by the chloride concentration, chloride ions probably had a role. Nevertheless, areas where the film is no longer protective are fully exposed to the electrolyte. Similar to the other proposed mechanisms, the dissolution of Al, Zr, Ti, and Ni is preferred over Cu due to their lower standard potentials. The Cu-rich porous regions within the pits seem to be a direct result of this preferential dissolution of the other elements. The porous structure, which was predominately Cu, suggests there was little Cu dissolution. The may explain the less prominent role of Cl in the pitting behavior of Vitreloy 105.

Chapter 7: Conclusions

In the current study, the corrosion properties of the $Zr_{50}Cu_{40}Al_{10}$, $Zr_{50}Cu_{33}Al_{10}Pd_{7,}$ and $Zr_{52.5}Cu_{17.9}Al_{10}Ni_{14.6}Ti_{5.0}$ (Vitreloy 105) BMGs were investigated in NaCl solutions. The $Zr_{50}Cu_{40}Al_{10}$ and $Zr_{50}Cu_{33}Al_{10}Pd_7$ BMGs both exhibited poor resistance to general and localized corrosion. At open-circuit conditions, $Zr_{50}Cu_{40}Al_{10}$ was susceptible to localized corrosion. $Zr_{50}Cu_{33}Al_{10}Pd_7$ was vulnerable to localized corrosion at E_{corr} or at potentials slightly higher than E_{corr}. The application of slightly anodic potentials yielded large increases in the current densities of both alloys. In fact, overpotentials of less than 50 mV resulted in such large current responses that the alloys experienced concentration polarization as evidenced by limiting diffusion current densities.

SEM examination of the corroded surfaces of $Zr_{50}Cu_{40}Al_{10}$ and $Zr_{50}Cu_{33}Al_{10}Pd_7$ revealed that exposure to NaCl solutions causes the formation of a solid product on the surface. The product seemed to have originated as particles on the surface, which eventually grew together to form a layer. As the layer grew, the particles also continued to grow. The continued growth of the particles caused stresses in the layer, which resulted in intense cracking. EDS analysis of the layer illustrated that it was predominately oxygen. However, the chemical makeup of the layer did vary at different depths. The initial layer (made up of many particles) had approximately equal amounts Zr, Cu, and O. The top surface of the layer was predominately O (70 at. %) and Zr (20 at. %) with Cu and Al accounting for the balance. The oxide layer grew in a peculiar pattern with uncovered areas having a dendritic appearance. This observation suggested that dendrites played some role in the localized corrosion behavior. The distinctive growth pattern was observed on both $Zr_{50}Cu_{40}Al_{10}$ and $Zr_{50}Cu_{33}Al_{10}Pd_7$. These exposed

areas were the areas where the localized attack first occurred. SAM of intensely corroded surfaces of $Zr_{50}Cu_{40}Al_{10}$ illustrated the enrichment of Cu, Cl, and O and a depletion of Zr. Corroded areas on the surface of $Zr_{50}Cu_{33}Al_{10}Pd_7$ were enriched with Cu, Cl, and Pd.

Mechanisms were proposed for both BMGs based on the galvanic electrode effect. The formation of a solid product over a large portion of the surface and the exposed regions of the as-polished alloy was the reason for the aggressive localized attack. The corrosion product acted as the cathode and supported the cathodic reaction. In the case of the neutral NaCl solution, the main cathodic reaction was the reduction of dissolved oxygen. The cathode supported the dissolution of the uncovered as-polished surface, which explained why these regions were locally attacked. The method of dissolution of the uncovered regions was the preferential dissolution of Zr and Al. Cu enrichment of corroded areas of $Zr_{50}Cu_{40}Al_{10}$ and Cu and Pd enrichment within corroded areas of $Zr_{50}Cu_{33}Al_{10}Pd_7$ was the result of the preferential dissolution. The enriched Cu zones along with the chloride ions provided an environment where copper-chloride complexes and the insoluble CuCl salt were able to form. High oxygen concentrations on the surface were probably the result of the formation of CO and/or $Cu(OH)_2*CuCl_2$ at higher potentials.

Vitreloy 105 exhibited superior corrosion behavior when compared to $Zr_{50}Cu_{40}Al_{10}$ and $Zr_{50}Cu_{33}Al_{10}Pd_7$. The alloy was passivated at open-circuit conditions (E_{corr}). There was a difference in the localized corrosion behavior of Vitreloy 105 depending on whether the sample was from the cross-section or along the long axis of the ingot. Cross sectional samples were vulnerable to pitting corrosion as the potential was raised above the corrosion potential. However, longitudinal samples were immune to

localized corrosion in some cases even after polarizing to 1600 mV. This finding was surprising because the longitudinal samples had inhomogeneities on the surface that were visible to the eye. These inhomogeneities were the "swirl" patterns that are commonly thought to be crystalline inclusions.

The SEM examination of the pits on the cross-sectional samples revealed pits that were hemispherical in shape unlike the irregular pits that were common on $Zr_{50}Cu_{40}Al_{10}$ and $Zr_{50}Cu_{33}Al_{10}Pd_7$. There also were no signs of the growth of corrosion product on the surface like what was observed in the other BMGs. EDS analysis of pits did show that the porous regions had high concentrations of Cu. However, significant Cl concentrations were not observed. Pit initiation on Vitreloy 105 seemed to be much more of a stochastic event in which pit initiation may have been related to some flaw or defect in the passive film. However, after initiation the exposed surface was attacked by the preferential dissolution of the less noble elements (Al, Ti, Zr, and Ni). Again this explains the Cu enrichment within pits. The porous Cu-enriched structure within the pits suggests that little Cu dissolution occurred, which may explain the less pronounced role of the chloride ions.

It is unclear why the longitudinal samples were immune to localized corrosion. Certainly, the passive films that form on these samples were more protective than those formed on the cross-sectional samples. It is possible that the inclusions played a role in the increased protectiveness of the film. The in-situ AFM experiments on a longitudinal sample showed that line profiles tended to increase as a function of time. This trend is thought to be related to the thickening of the passive film, which may explain the longitudinal samples resistance to pitting.

Chapter 8: Future Work

Possible future work for examining the corrosion behaviors of $Zr_{50}Cu_{40}Al_{10}$ and $Zr_{50}Cu_{33}Al_{10}Pd_7$ should include continued efforts to construct experiments that can provide more details on the localized corrosion mechanisms of these alloys. SAM did provide chemical information about the corroded surfaces; however, it was unable to provide detailed analysis of the chemical states that were present on the surface. Chemical state imaging is possible with x-ray photoelectron spectroscopy (XPS). This technique would be able to clearly define the kind of bonding associated with Cu so that distinctions could be made between CuO_2 and CO. In addition, chloride compounds could be identified.

Analyzing the electrolyte might also provide a means to obtain more information about the surface reactions that occur. Since the corrosion process forces metal ions into the solution, the determination of the concentrations of ions in the electrolyte could provide insight into the reactions occurring at the surface of the sample. Previous attempts were made to analyze electrolytes with atomic absorption spectroscopy (AAS). However, the NaCl of the electrolyte caused masking, and the concentrations of metal ions could not be determined. Inductively coupled plasma mass spectrometry (ICP-MS) is a highly sensitive (~ part per billion) tool that is capable of analyzing ions in liquid samples. However, the technique can be expensive. A relatively low-cost way to analyze the electrolytes would be chemical spot tests. However, this technique will only provide qualitative information about the ions present in the electrolyte.

The unexpected high localized corrosion resistance of inhomogeneous samples of Vitreloy 105 provides an opportunity for interesting future work. The “swirl” patterns

are easily visible to the eye even on rough (240 SiC grit) unetched surfaces. It is clear that there is a significant difference in removal rates between the inclusions and the bulk matrix. Probing the mechanical properties of these regions using nanoindentation could yield interesting information. In addition, the inclusions must be identified. Electron microprobe analysis (EPMA) may provide a way to determine if the composition of the inclusion is significantly different than the matrix. When XRD experiments were done on samples that contained these inclusions, the diffraction pattern attained was the diffuse pattern typical of an amorphous material. This observation could be a result of instrumental limitations. It is possible that the inclusions are not crystalline. The analysis of the samples using synchrotron radiation or election backscatter diffraction (EBSD) could determine if the inclusions are crystalline. DSC experiments of samples taken from the cross-section and the longitudinal direction may also provide information on crystallinity if the enthalpy changes are compared.

References

1. F.E. Luborsky, Amorphous metallic alloys, in F.E. Luborsky (Ed.) Amorphous Metallic Alloys, Butterworths: London. 1983. pp. 1-7.
2. K. Hashimoto, Chemical Properties, in F.E. Luborsky (Ed.) Amorphous Metallic Alloys, Butterworths: London. 1983. pp. 471-486.
3. A. Inoue, Stabilization of metallic supercooled liquid and bulk amorphous alloys. Acta Materialia. 48:1 (2000) 279-306.
4. H.A. Bruck, A.J. Rosakis, and W.L. Johnson, The dynamic compressive behavior of beryllium bearing bulk metallic glasses. Journal of Materials Research. 11:2 (1996) 503-511.
5. Z. Bian, G. He, and G.L. Chen, Microstructure and mechanical properties of as-cast $Zr_{52.5}Cu_{17.9}Ni_{14.6}Al_{10}Ti_5$ bulky glass alloy. Scripta Materialia. 43:11 (2000) 1003-1008.
6. W.H. Wang, Elastic moduli and behaviors of metallic glasses. Journal of Non-Crystalline Solids. 351 (2005) 1481–1485.
7. A. Inoue, Bulk amorphous and nanocrystalline alloys with high functional properties. Materials Science and Engineering a-Structural Materials Properties Microstructure and Processing. 304 (2001) 1-10.
8. W.H. Peter, P.K. Liaw, R.A. Buchanan, C.T. Liu, C.R. Brooks, J.A.H. Jr, C.A.C. Jr, and J.L. Wright, Fatigue behavior of $Zr_{52.5}Al_{10}Ti_5Cu_{17.9}Ni_{14.6}$ bulk metallic glass. Intermetallics. 10 (2002) 1125-1129.
9. G.Y. Wang, P.K. Liaw, W.H. Peter, B. Yang, Y. Yokoyama, M.L. Benson, B.A. Green, M.J. Kirkham, S.A. White, and T.A. Saleh, Fatigue behavior of bulk-metallic glasses. Intermetallics. 12:7-9 (2004) 885-892.
10. A. Gebert, K. Buchholz, A.M. El-Aziz, and J. Eckert, Hot water corrosion behaviour of Zr-Cu-Al-Ni bulk metallic glass. Materials Science and Engineering a-Structural Materials Properties Microstructure and Processing. 316:1-2 (2001) 60-65.
11. A. Gebert, K. Mummert, J. Eckert, L. Schultz, and A. Inoue, Electrochemical investigations on the bulk glass forming $Zr_{55}Cu_{30}Al_{10}Ni_5$ alloy. Materials and Corrosion. 48 (1997) 293-297.
12. A. Gebert, K. Buchholz, A. Leonhard, K. Mummert, J. Eckert, and L. Schultz, Investigations on the electrochemical behaviour of Zr-based bulk metallic glasses. Materials Science and Engineering A. 267:2 (1999) 294-300.
13. S. Hiromoto, A.P. Tsai, M. Sumita, and T. Hanawa, Effects of surface finishing and dissolved oxygen on the polarization behavior of $Zr_{65}Al_{7.5}Ni_{10}Cu_{17.5}$ amorphous alloy in phosphate buffered solution. Corrosion Science. 42:12 (2000) 2167-2185.
14. U. Köster, D. Zander, Triwikantoro, A. Rudiger, and L. Jastrow, Environmental properties of Zr-based metallic glasses and nanocrystalline alloys. Scripta Materialia. 44:8-9 (2001) 1649-1654.
15. M.L. Morrison, R.A. Buchanan, A. Peker, W.H. Peter, J.A. Horton, and P.K. Liaw, Cyclic-anodic-polarization studies of a $Zr_{41.2}Ti_{13.8}Ni_{10}Cu_{12.5}Be_{22.5}$. Intermetallics. 12 (2004) 1177-1181.
16. B.A. Green, P.K. Liaw, and R.A. Buchanan, Corrosion Behavior, in M.K. Miller and P.K. Liaw (Eds), Bulk Metallic Glasses, Springer: New York. 2008. pp. 205-234.

17. W.H. Jiang, F. Jiang, B.A. Green, F.X. Liu, P.K. Liaw, H. Choo, and K.Q. Qiu, Electrochemical corrosion behavior of a Zr-based bulk-metallic glass. Applied Physics Letters. 91:4 (2007).
18. J.R. Scully, A. Gebert, and J.H. Payer, Corrosion and related mechanical properties of bulk metallic glasses. Journal of Materials Research. 22:2 (2007) 302-313.
19. L. Liu, C.L. Qiu, Q. Chen, and S.M. Zhang, Corrosion behavior of Zr-based bulk metallic glasses in different artificial body fluids. Journal of Alloys and Compounds. 425:1-2 (2006) 268-273.
20. D. Zander, B. Heisterkamp, and I. Gallino, Corrosion resistance of Cu-Zr-Al-Y and Zr-Cu-Ni-Al-Nb bulk metallic glasses. Journal of Alloys and Compounds. 434 (2007) 234-236.
21. S. Pang, T. Zhang, H. Kimura, K. Asami, and A. Inoue, Corrosion behavior of Zr-(Nb-)Al-Ni-Cu glassy alloys. Materials Transactions, JIM (Japan). 41:11 (2000) 1490-1494.
22. V.R. Raju, U. Kühn, U. Wolff, F. Schneider, J. Eckert, R. Reiche, and A. Gebert, Corrosion behaviour of Zr-based bulk glass-forming alloys containing Nb or Ti. Materials Letters. 57 (2002) 173-177.
23. M. Mehmood, B.-P. Zhang, E. Akiyama, H. Habazaki, A. Kawashima, K. Asami, and K. Hashimoto, Experimental evidence for the critical size of heterogeneity areas for pitting corrosion of Cr-Zr alloys in 6 M HCl. Corrosion Science. 40:1 (1998) 1-17.
24. S. Hiromoto, A.-P. Tsai, M. Sumita, and T. Hanawa, Effect of chloride ion on the anodic polarization behavior of the Zr65Al7.5Ni10Cu17.5 amorphous alloy in phosphate buffered solution. Corrosion Science. 42:9 (2000) 1651-1660.
25. V. Schroeder, C.J. Gilbert, and R.O. Ritchie, Comparison of the Corrosion Behavior of a Bulk Amorphous Metal, $Zr_{41.2}Ti_{13.8}Cu_{12.5}Ni_{10}Be_{22.5}$ with Its Crystallized Form. Scripta Materialia. 38:10 (1998) 1481-1485.
26. R.G. Walmsley, Y.S. Lee, A.F. Marshall, and D.A. Stevenson, Electrochemical characterization of amorphous and microcrystalline metals. Journal of Non-Crystalline Solids. 61-2:JAN (1984) 625-630.
27. W.H. Peter, R.A. Buchanan, C.T. Liu, P.K. Liaw, M.L. Morrison, C.A. Carmichael, and J.L. Wright, Localized corrosion behavior of a zirconium-based bulk metallic glass relative to its crystalline state. Intermetallics. 10 (2002) 1157-1162.
28. S.R. Elliot, *Physics of Amorphous Materials*. 1984, London: Longman.
29. W. Klement, R.H. Willens, and P. Duwez, Non-crystalline structure in solidified gold-silicon alloys. Nature. 187 (1960) 869-870.
30. W.D. Callister, *Materials Science and Engineering: An Introduction*. 7 ed. 2006: Wiley.
31. H.S. Chen, Glassy Metals. Reports on Progress in Physics. 43:4 (1980) 353-432.
32. A.J. Drehman, A.L. Greer, and D. Turnbull, Bulk formation of a metallic glass : $Pd_{40}Ni_{40}P_{20}$. Applied Physics Letters. 41:8 (1982) 716-717.
33. A.J. Drehman and A.L. Greer, Kinetics of Crystal Nucleation and Growth in $Pd_{40}Ni_{40}P_{20}$ Glass. Acta Metallurgica. 32:3 (1984) 323-332.

34. A. Inoue, T. Zhang, and T. Masumoto, Al-La-Ni Amorphous-Alloys with a Wide Supercooled Liquid Region. Materials Transactions Jim. 30:12 (1989) 965-972.
35. A. Inoue, M. Kohinata, and A.-P. Tsai, Mg-Ni-La Amorphous Alloys with a Wide Supercooled Liquid Region. Materials Transactions, JIM. 30:5 (1989) 378-381.
36. A. Inoue, T. Zhang, and T. Masumoto, Zr-Al-Ni Amorphous-Alloys with High Glass-Transition Temperature and Significant Supercooled Liquid Region. Materials Transactions Jim. 31:3 (1990) 177-183.
37. A. Inoue, T. Shibata, and T. Zhang, Effect of additional elements on glass transition behavior and glass formation tendency of Zr-Al-Cu-Ni alloys. Materials Transactions Jim. 36:12 (1995) 1420-1426.
38. A. Inoue, N. Nishiyama, K. Amiya, T. Zhang, and T. Masumoto, Ti-based amorphous alloys with a wide supercooled liquid region. Materials Letters. 19:3-4 (1994) 131.
39. A. Inoue and J.S. Gook, Fe-Based Ferromagnetic Glassy Alloys with Wide Supercooled Liquid Region. Materials Transactions Jim. 36:9 (1995) 1180-1183.
40. A. Inoue and J.S. Gook, Effect of additional elements (M) on the thermal stability of supercooled liquid in Fe(72-x)Al(5)Ga(2)P(11)C(6)B(4)M(x) glassy alloys. Materials Transactions Jim. 37:1 (1996) 32-38.
41. B.L. Shen, H. Koshiba, T. Mizushima, and A. Inoue, Bulk amorphous Fe-Ga-P-B-C alloys with a large supercooled liquid region. Materials Transactions Jim. 41:7 (2000) 873-876.
42. W. Zhang and A. Inoue, Thermal and magnetic properties of Fe-Co-Ln-B (Ln=Nd, Sm, Th or Dy) amorphous alloys with high magnetostriction. Materials Transactions Jim. 40:1 (1999) 78-81.
43. T.D. Shen and R.B. Schwarz, Bulk ferromagnetic glasses prepared by flux melting and water quenching. Applied Physics Letters. 75:1 (1999) 49-51.
44. A. Inoue, T. Zhang, H. Koshiba, and A. Makino, New bulk amorphous Fe-(Co,Ni)-M-B (M=Zr,Hf,Nb,Ta,Mo,W) alloys with good soft magnetic properties. Journal of Applied Physics. 83:11 (1998) 6326-6328.
45. S.J. Pang, T. Zhang, K. Asami, and A. Inoue, New Fe-Cr-Mo-(Nb, Ta)-C-B glassy alloys with high glass-forming ability and good corrosion resistance. Materials Transactions Jim. 42:2 (2001) 376-379.
46. A. Inoue, W. Zhang, T. Zhang, and K. Kurosaka, Thermal and mechanical properties of Cu-based Cu-Zr-Ti bulk glassy alloys. Materials Transactions. 42:6 (2001) 1149-1151.
47. A. Inoue, T. Zhang, K. Kurosaka, and W. Zhang, High-strength Cu-based bulk glassy alloys in Cu-Zr-Ti-Be system. Materials Transactions. 42:8 (2001) 1800-1804.
48. T. Zhang, K. Kurosaka, and A. Inoue, Thermal and mechanical properties of Cu-based Cu-Zr-Ti-Y bulk glassy alloys. Materials Transactions. 42:10 (2001) 2042-2045.
49. A. Inoue, N. Nishiyama, and T. Matsuda, Preparation of bulk glassy Pd40Ni10Cu30P20 alloy of 40 mm in diameter by water quenching. Materials Transactions Jim. 37:2 (1996) 181-184.

50. Y. He, T.D. Shen, and R.B. Schwarz, Bulk amorphous metallic alloys: Synthesis by fluxing techniques and properties. Metallurgical and Materials Transactions a-Physical Metallurgy and Materials Science. 29:7 (1998) 1795-1804.
51. A. Peker and W.L. Johnson, A Highly Processable Metallic-Glass - $Zr_{41.2}Ti_{13.8}Cu_{12.5}Ni_{10.0}Be_{22.5}$. Applied Physics Letters. 63:17 (1993) 2342-2344.
52. X.H. Lin and W.L. Johnson, Formation of Ti-Zr-Cu-Ni Bulk Metallic Glasses. Journal of Applied Physics. 78:11 (1995) 6514-6519.
53. A. Inoue and N. Nishiyama, Extremely low critical cooling rates of new Pd-Cu-P base amorphous alloys. Materials Science and Engineering A. 226-228 (1997) 401-405.
54. D. Turnbull, Under What Conditions Can a Glass Be Formed. Contemporary Physics. 10:5 (1969) 473-488.
55. A. Inoue, T. Zhang, and T. Masumoto, Glass-forming ability of alloys. Journal of Non-Crystalline Solids. 156 (1993) 473-480.
56. Z.P. Lu and C.T. Liu, A new glass-forming ability criterion for bulk metallic glasses. Acta Materialia. 50:13 (2002) 3501-3512.
57. H.A. Davies, Metallic glass formation, in F.E. Luborsky (Ed.) Amorphous Metallic Alloys, Buttersworth: London. 1983.
58. Y. Li, S.C. Ng, C.K. Ong, H.H. Hng, and T.T. Goh, Glass forming ability of bulk glass forming alloys. Scripta Materialia. 36:7 (1997) 783-787.
59. A. Gebert, J. Eckert, and L. Schultz, Effect of oxygen on phase formation and thermal stability of slowly cooled $Zr_{65}Al_{7.5}Cu_{17.5}Ni_{10}$ metallic glass. Acta Materialia. 46:15 (1998) 5475-5482.
60. X.H. Lin, W.L. Johnson, and W.K. Rhim, Effect of Oxygen Impurity on Crystallization of an Undercooled Bulk Glass Forming Zr-Ti-Cu-Ni-Al alloy. Materials Transactions, JIM. 38:5 (1997) 473-477.
61. D.J. Sordelet, X. Yang, E.A. Rozhkova, M.F. Besser, and M.J. Kramer, Influence of oxygen content in phase selection during quenching of Zr80Pt20 melt spun ribbons. Intermetallics. 12:10-11 (2004) 1211-1217.
62. Z. Altounian, E. Batalla, J.O. Strom-Olsen, and J.L. Walter, The influence of oxygen and other impurities on the crystallization of $NiZr_2$ and related metallic glasses. Journal of Applied Physics. 61:1 (1987) 149-155.
63. B.S. Murty, D.H. Ping, and K. Hono, Direct evidence for oxygen stabilization of icosahedral phase during crystallization of $Zr_{65}Cu_{27.5}Al_{7.5}$ metallic glass. Applied Physics Letters. 76:1 (2000) 55-57.
64. C.T. Liu, M.F. Chisholm, and M.K. Miller, Oxygen impurity and microalloying effect in a Zr-based bulk metallic glass alloy. Intermetallics. 10:11-12 (2002) 1105-1112.
65. W.L. Johnson, Bulk metallic glasses - A new engineering material. Current Opinion in Solid State & Materials Science. 1:3 (1996) 383-386.
66. M. Telford, The case for bulk metallic glass. Materials Today. 7:3 (2004) 36-43.
67. A. Inoue, C. Fan, J. Saida, and T. Zhang, High-strength Zr-based bulk amorphous alloys containing nanocrystalline and nanoquasicrystalline particles. Science and Technology of Advanced Materials (UK). 1:2 (2000) 73-86.

68. A. Inoue, T. Zhang, N. Nishiyama, K. Ohba, and T. Masumoto, Preparation of 16 mm diameter rod of amorphous $Zr_{65}Al_{7.5}Ni_{10}Cu_{17.5}$ alloy. Materials Transactions Jim. 34:12 (1993) 1234-1237.
69. J. Basu and S. Ranganathan, Bulk metallic glasses: A new class of engineering materials. Sadhana-Academy Proceedings in Engineering Sciences. 28 (2003) 783-798.
70. W.H. Peter, R.A. Buchanan, C.T. Liu, and P.K. Liaw, The fatigue behavior of a zirconium-based bulk metallic glass. Journal of Non-Crystalline Solids. 317 (2003) 187-192.
71. C.C. Hays, C.P. Kim, and W.L. Johnson, Microstructure controlled shear band pattern formation and enhanced plasticity of bulk metallic glasses containing in situ formed ductile phase dendrite dispersions. Physical Review Letters. 84:13 (2000) 2901-2904.
72. S. Hiromoto, A.P. Tsai, M. Sumita, and T. Hanawa, Effect of chloride ion on the anodic polarization behavior of the $Zr_{65}Al_{7.5}Ni_{10}Cu_{17.5}$ amorphous alloy in phosphate buffered solution. Corrosion Science. 42:9 (2000) 1651-1660.
73. M.L. Morrison, R.A. Buchanan, R.V. Leon, C.T. Liu, B.A. Green, P.K. Liaw, and J.A. Horton, The electrochemical evaluation of a Zr-based bulk metallic glass in a phosphate-buffered saline electrolyte. Journal of Biomedical Materials Research Part A. 74A:3 (2005) 430-438.
74. C.L. Qiu, L. Liu, M. Sun, and S.M. Zhang, The effect of Nb addition on mechanical properties, corrosion behavior, and metal-ion release of ZrAlCuNi bulk metallic glasses in artificial body fluid. Journal of Biomedical Materials Research Part A. 75:4 (2005) 950-956.
75. S. Buzzi, K.F. Jin, P.J. Uggowitzer, S. Tosatti, T. Gerber, and J.F. Loffler, Cytotoxicity of Zr-based bulk metallic glasses. Intermetallics. 14:7 (2006) 729-734.
76. L. Liu, C.L. Qiu, M. Sun, Q. Chen, K.C. Chan, and G.K.H. Pang, Improvements in the plasticity and biocompatibility of Zr-Cu-Ni-Al bulk metallic glass by the microalloying of Nb. Materials Science and Engineering a-Structural Materials Properties Microstructure and Processing. 449 (2007) 193-197.
77. F.X. Qin, X.M. Wang, and A. Inoue, Observation of bone-like apatite on Ti-coated Zr55Al10Ni5Cu30 bulk metallic glass after alkali treatment. Intermetallics. 16:7 (2008) 917-922.
78. C.L. Qiu, Q. Chen, L. Liu, K.C. Chan, J.X. Zhou, P.P. Chen, and S.M. Zhang, A novel Ni-free Zr-based bulk metallic glass with enhanced plasticity and good biocompatibility. Scripta Materialia. 55:7 (2006) 605-608.
79. J. Eckert, U. Kuhn, J. Das, S. Scudino, and N. Radtke, Nanostructured composite materials with improved deformation behavior. Advanced Engineering Materials. 7:7 (2005) 587-596.
80. C.A.C. Souza, F.S. Politi, and C.S. Kiminami, Influence of structural relaxation and partial devitrification on the corrosion resistance of $Fe_{78}B_{13}Si_9$ amorphous alloy. Scripta Materialia. 39:3 (1998) 329-334.
81. C.A.C. Souza, M.F. de Oliveira, J.E. May, W.J. Botta F, N.A. Mariano, S.E. Kuri, and C.S. Kiminami, Corrosion resistance of amorphous and nanocrystalline Fe-

M-B (M=Zr, Nb) alloys. Journal of Non-Crystalline Solids. 273:1-3 (2000) 282-288.
82. M.G. Alvarez, S.M. Vazquez, J. Moya, and H. Sirkin, Anodic behaviour of Fe73.5Si13.5-xAlxB9Nb3Cu1 (x = 0-2) amorphous, nanostructured and crystalline alloys. Scripta Materialia. 44:3 (2001) 507-512.
83. R.S. Dutta, R.T. Savalia, and G.K. Dey, Corrosion behaviour of rapidly solidified $Zr_{76}Ni_{16}Fe_8$ alloy in chloride environments. Scripta Metallurgica et Materialia. 32:2 (1995) 207-212.
84. C.G. Tan, W.J. Jiang, Z.C. Zhang, X.Q. Wu, and J.G. Lin, The effect of Ti-addition on the corrosion behavior of the partially crystallized Ni-based bulk metallic glasses. Materials Chemistry and Physics. 108 (2008) 29-32.
85. D. Szewieczek, J. Tyrlik-Held, and Z. Paszenda, Corrosion investigations of nanocrystalline iron based alloy. Journal of Materials Processing Technology. 78:1-3 (1998) 171-176.
86. M.S. Ong, Y. Li, D.J. Blackwood, S.C. Ng, and C.H. Kam, Effect of heat treatment on the corrosion behaviour of amorphous Mg-18 at% Ni alloy. Journal of Alloys and Compounds. 279:2 (1998) 252-258.
87. K. Mondal, B.S. Murty, and U.K. Chatterjee, Electrochemical behaviour of amorphous and nanoquasicrystalline Zr-Pd and Zr-Pt alloys in different environments. Corrosion Science. 47 (2005) 2619-2635.
88. P.Y. Park, E. Akiyama, H. Habazaki, A. Kawashima, K. Asami, and K. Hashimoto, The corrosion behavior of sputter-deposited amorphous Mo-Zr alloys in 12 M HCl. Corrosion Science. 37:2 (1995) 307-320.
89. M.D. Archer, C.C. Corke, and B.H. Harji, The electrochemical properties of metallic glasses. Electrochimica Acta. 32:1 (1987) 13.
90. K. Mondal, B.S. Murty, and U.K. Chatterjee, Electrochemical behavior of multicomponent amorphous and nanocrystalline Zr-based alloys in different environments. Corrosion Science. 48 (2006) 2212-2225.
91. G.K. Dey, R.T. Savalia, S.K. Sharma, and S.K. Kulkarni, Corrosion studies on amorhpous and crystalline $Zr_{67}Ni_{33}$. Corrosion Science. 29:7 (1989) 823-831.
92. M. Naka, K. Hashimoto, and T. Masumoto, Corrosion behavior of amorphous and crystalline $Cu_{50}Ti_{50}$ and $Cu_{50}Zr_{50}$ alloys. Journal of Non-Crystalline Solids 30 (1978) 29-36.
93. H. Bala and S. Szymura, Acid corrosion of amorhpus and crystalline Cu-Zr alloys. Applied Surface Science. 35 (1988) 41-51.
94. K. Asami, H. Habazaki, A. Inoue, and K. Hashimoto, Recent Development of Highly Corrosion Resistant Bulk Glassy Alloys. Materials Science Forum. 502 (2005) 225-230.
95. F.X. Qin, H.F. Zhang, Y.F. Deng, B.Z. Ding, and Z.Q. Hu, Corrosion resistance of Zr-based bulk amorphous alloys containing Pd. Journal of Alloys and Compounds. 375:1-2 (2004) 318-323.
96. F.X. Qin, H.F. Zhang, P. Chen, F.F. Chen, D.C. Qiao, and Z.Q. Hu, Corrosion behavior of bulk amorphous $Zr_{55}Al_{10}Cu_{30}Ni_{5-x}Pd_x$ alloys. Materials Letters. 58 (2004) 1246-1250.

97. S.J. Pang, T. Zhang, K. Asami, and A. Inoue, Formation, corrosion behavior, and mechanical properties of bulk glassy Zr-Al-Co-Nb alloys. Journal of Materials Research. 18:7 (2003) 1652-1658.
98. M.K. Tam, S.J. Pang, and C.H. Shek, Corrosion behavior and glass-forming ability of Cu-Zr-Al-Nb alloys. Journal of Non-Crystalline Solids. 353 (2007) 3596-3599.
99. L. Liu, C.L. Qiu, H. Zou, and K.C. Chan, The effect of the microalloying of Hf on the corrosion behavior of ZrCuNiAl bulk metallic glass. Journal of Alloys and Compounds. 399:1-2 (2005) 144-148.
100. L. Liu, C.L. Qiu, Q. Chen, K.C. Chan, and S.M. Zhang, Deformation behavior, corrosion resistance and cytoxicity of Ni-free Zr-based bulk metallic glasses. Journal of Biomedical Materials Research Part A. 86A:1 (2008) 160-169
101. L. Huang, D.C. Qiao, B.A. Green, P.K. Liaw, J.F. Wang, S.J. Pang, and T. Zhang, Bio-corrosion study on Zirconium-based bulk-metallic glasses. submitted to Intermetallics, (2008).
102. K.U. Mudali UK, Eckert J, Schultz l, Gebert A, Corrosion behaviour of zirconium based bulk metallic glasses. Transactions of the Indian Institute of Metals. 59:1 (2006) 123-138.
103. B.A. Green, R.A. Buchanan, Y. Yokoyama, and P.K. Liaw, unpublished data.
104. U.K. Mudali, S. Baunack, J. Eckert, L. Schultz, and A. Gebert, Pitting corrosion of bulk glass-forming zirconium-based alloys. Journal of Alloys and Compounds. 377 (2004) 290-297.
105. H.B. Lu, L.C. Zhang, A. Gebert, and L. Schultz, Pitting corrosion of Cu-Zr metallic glasses in hydrochloric acid solutions. Journal of Alloys and Compounds. 462:1-2 (2008) 60-67.
106. M.L. Morrison, *The Mechanical and Electrochemical Properties of Bulk Metallic Glasses*, in *Materials Science and Engineering*. 2005, The University of Tennessee: Knoxville.
107. H.H. Willard, L.L. Merritt, and J.A. Dean, Thermal Analysis, Instrumental Methods of Analysis, D. Van Nostrand Company: New York. 1974. pp. 496-521.
108. E.E. Stansbury and R.A. Buchanan, *Fundamentals of electrochemical corrosion*. 2000, Materials Park, Oh: ASM International.
109. R.P. Gunnawardane and C.R. Arumainayagam, Auger Electron Spectroscpy, in D.R. Vij (Ed.) Handbook of Applied Solid State Spectroscopy, Springer: New York. 2006. pp. 451-483.
110. J.F. Watts and J. Wolstenholme, *An Introduction to Surface Analysis by XPS and AES*. second ed. 2003: John Wiley & Sons.
111. Y. Yokoyama, Y. Akeno, T. Yamasaki, P.K. Liaw, R.A. Buchanan, and A. Inoue, Evolution of mechanical properties of cast Zr50Cu40Al10 glassy alloys by structural relaxation. Materials Transactions. 46:12 (2005) 2755-2761.
112. Y. Yokoyama, P.K. Liaw, M. Nishijima, K. Hiraga, R.A. Buchanan, and A. Inoue, Fatigue-strength enhancement of cast Zr50Cu40Al10 glassy alloys. Materials Transactions. 47:5 (2006) 1286-1293.
113. Y. Yokoyama, T. Yamasaki, P.K. Liaw, R.A. Buchanan, and A. Inoue, Volume change in Zr50Cu40Al10 glassy alloys. Journal of Alloys and Compounds. 434 (2007) 160-163.

114. Y. Yokoyama, T. Yamasaki, P.K. Liaw, R.A. Buchanan, and A. Inoue, Glass-structure changes in tilt-cast Zr-Cu-Al glassy alloys. Materials Science and Engineering a-Structural Materials Properties Microstructure and Processing. 449 (2007) 621-626.
115. Y. Yokoyama, T. Yamasaki, P.K. Liaw, and A. Inoue, Relations between the thermal and mechanical properties of cast Zr-TM-Al (TM : Cu, Ni, or Co) bulk glassy alloys. Materials Transactions. 48:7 (2007) 1846-1849.
116. Y. Yokoyama and A. Inoue. in *Japan Institute of Metals Autumn Meeting*. 2001.
117. Y. Yokoyama, Ductility improvement of Zr-Cu-Ni-Al glassy alloy. Journal of Non-Crystalline Solids. 316:1 (2003) 104-113.
118. Y. Yokoyama, E. Mund, A. Inoue, and L. Schultz, Production of $Zr_{55}Cu_{30}Ni_5Al_{10}$ Glassy Alloy Rod of 30mm in Diameter by a Cap-Cast Technique. Materials Transactions. 48:12 (2007) 3190-3192.
119. D.A. Jones, *Principles and Prevention of Corrosion*. second ed. 1995: Prentice Hall.
120. M. Pourbaix, *Atlas of Electrochemical Equilibria*. 1966, Oxford: Pergamon Press.
121. D.D. Wagman, W.H. Evans, V.B. Parker, R.H. Schumm, I. Halow, S.M. Bailey, K.L. Churney, and R.L. Nuttall, The NBS tables of chemical thermodynamic properties selected values for inorganic C_1 and C_2 organic substances in SI units. Journal of Physical and Chemical Reference Data. Volume 11:2 (1982).
122. S. Baunack, U.K. Mudali, and A. Gebert, Characterization of oxide layers on amorphous Zr-based alloys by Auger electron spectroscopy with sputter depth profiling. Applied Surface Science. 252:1 (2005) 162.
123. B.A. Green, P.K. Liaw, and R.A. Buchanan, Corrosion Behavior, in M.K. Miller and P.K. Liaw (Eds), Bulk Metallic Glasses, Springer US. 2007. pp. 205-234.
124. J.G. Speight, *Lange's Handbook of Chemistry*. 2005, McGraw-Hill.
125. G. Wulfsberg, *Principles of Descriptive Inorganic Chemistry*. 1992: University Science Books.
126. W.H. Peter. 2002, The University of Tennessee, Knoxville.
127. M. Pourbaix, *Lectures on Electrochemical Corrosion*. 1973, New York, NY: Plenum Press. 336.

Appendix of Tables

Table 1. Transition temperatures and GFA parameters.

	T_g (K)	T_x (K)	T_l (K)	T_{rg}	ΔT_{xg} (K)	γ
$Zr_{50}Cu_{40}Al_{10}$	695	778	1154	0.60	83	0.42
$Zr_{50}Cu_{40}Al_{10}Pd_7$	710	775	1164	0.61	65	0.41
Vitreloy 105	672	727	1101	0.61	55	0.41

$T_{rg} = T_g / T_l$
$\Delta T_{xg} = T_x - T_g$
$\gamma = T_x / (T_g + T_l)$

Table 2. Mean polarization parameters for $Zr_{50}Cu_{40}Al_{10}$ in NaCl electrolytes of varying chloride concentration.

$[Cl^-]$ (M)	E_{corr} (mV)	m_1 (mV/half decade)	m_2 (mV/half decade)	i_{corr} (10^7*Acm^{-2})	CPR (μm/yr)
0.1	-467	35	7	97	120
0.6	-518 ± 4	21 ± 6	9 ± 3	128 ± 50	160 ± 60

Potentials versus SCE
95% student t confidence intervals
Note: Two experiments were performed in 0.1 M NaCl; thus, confidence intervals were not calculated.

Table 3. Polarization parameters for $Zr_{50}Cu_{33}Al_{10}Pd_7$ in 0.6 M NaCl electrolytes of varying chloride concentration.

Scan #	E_{corr} (mV)	m_1 (mV/half decade)	m_2 (mV/half decade)	i_{corr} (10^7*A cm^{-2})	CPR (μm/yr)
1	-322	46	2	130	161
2	-321	15	11	635	786
3	-338	9	7	201	250
4	-315	11	6	129	157
5	-334	10	2	129	160

Potentials versus SCE

Table 4 . Atomic concentrations of positions given in Figure 61.

Position	Zr	Cu	Al	Pd	O	Na	Cl	C
1	20.2	3.2	2.6	1.5	25.5	3.7	33.1	10.1
2	19.6	5.0	3.4	1.6	28.2	0.0	30.2	12.0
3	11.6	9.5	2.4	0.5	17.7	1.8	44.5	11.9
4	31.8	4.2	5.5	0.0	40.0	0.0	0.0	18.6

Table 5. Standard Gibbs free energies of formation of selected oxides.

Molecular Formula	Name	ΔG_f^o (kJ/mol)
Al_2O_3 (corundum)	aluminum (III) oxide	-1582.3*
Cu_2O	copper(I) oxide	-146.0*
CuO	copper (II) oxide	-129.7*
Ni_3O_4	nickelo-nickelic oxide	-711.9**
PdO	hydrated palladium oxide	-64.1**
TiO_2 (rutile)	titanium (IV) oxide	-889.5*
ZrO_2 (monoclinic)	zirconium(IV) oxide	-1042.8*

* and ** denote values obtained from references 121 and 122 , respectively.

Table 6. Selected Standard Electrode Potentials in Aqueous Solutions.

Electrode reaction	E, mV (SCE)
$Al = Al^{3+} + 3e$	-1917
$Ti = Ti^{2+} + 2e$	-1871
$Zr = Zr^{4+} + 4e$	-1791
$Ni = Ni^{2+} + 2e$	-498
$Cu = Cu^{2+} + 2e$	99
$Cu = Cu^{+} + e$	279
$Pd = Pd^{2+} + 2e$	674

Values from references 109 and 121.

Appendix of Figures

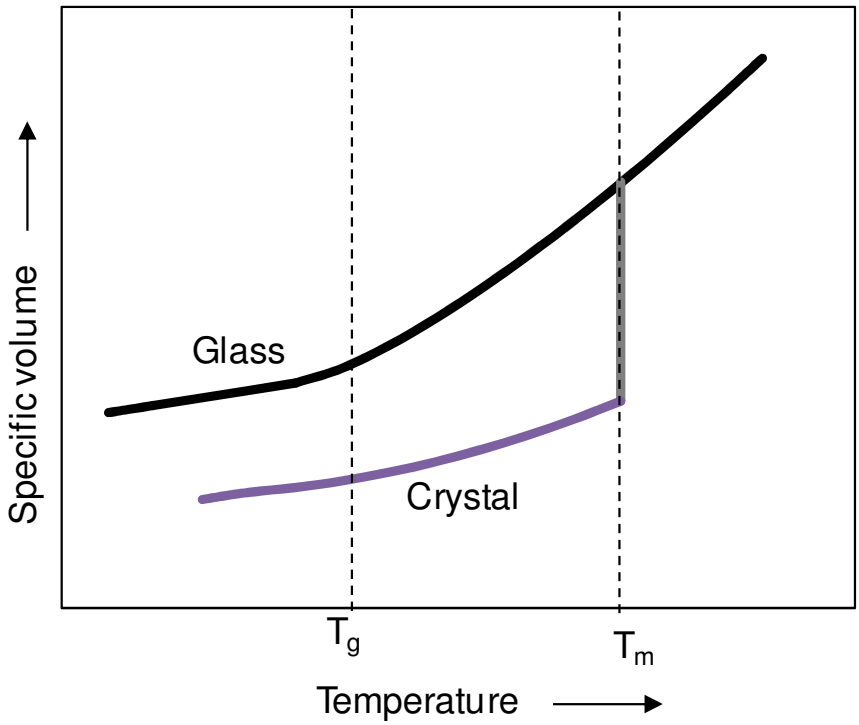

Figure 1. Temperature dependence of the specific volume of a molten metal that undergoes solidification by crystallization (gray curve) or by vitrification (black curve).

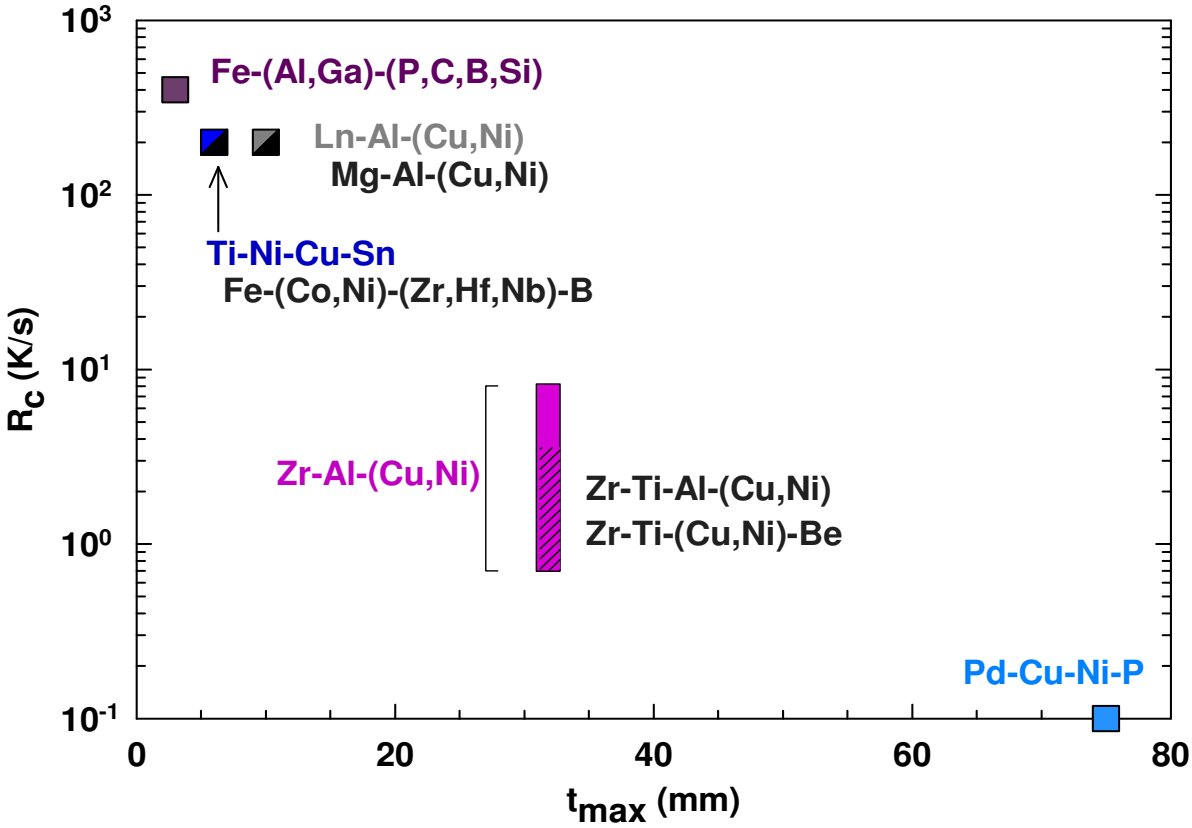

Figure 2. Critical cooling rate (R_c) versus maximum thickness (t_{max}) for various BMG systems. Figure was generated from data published by Inoue [3].

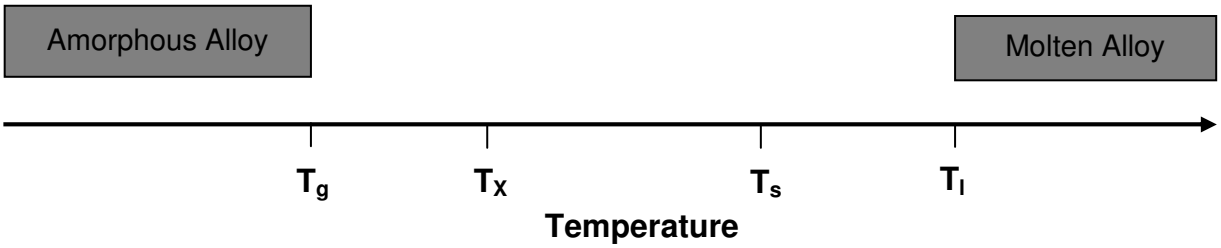

Figure 3. Temperatures that can be obtained from thermal analysis techniques. T_g, T_x, T_s, and T_l represent the glass transition, crystallization, solidus, and liquidus temperatures, respectively.

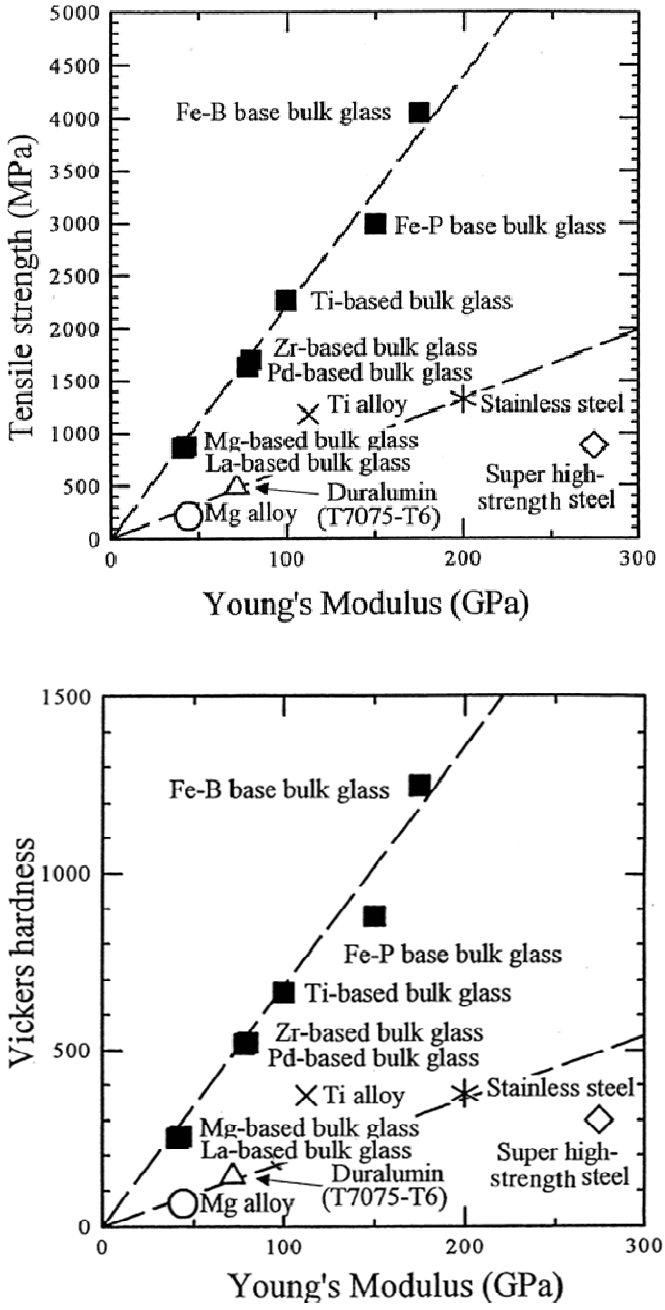

Figure 4. (top) Tensile strength versus Young's modulus and (bottom) Vickers hardness versus Young's modulus for various BMG systems and crystalline alloys [3].[3]

[3] The figure was Reprinted with permission from Acta Materialia, 48, Akihisa Inoue, Stabilization of metallic supercooled liquid and bulk amorphous alloys, 279-306, Copyright (2000), with permission from Elsevier.

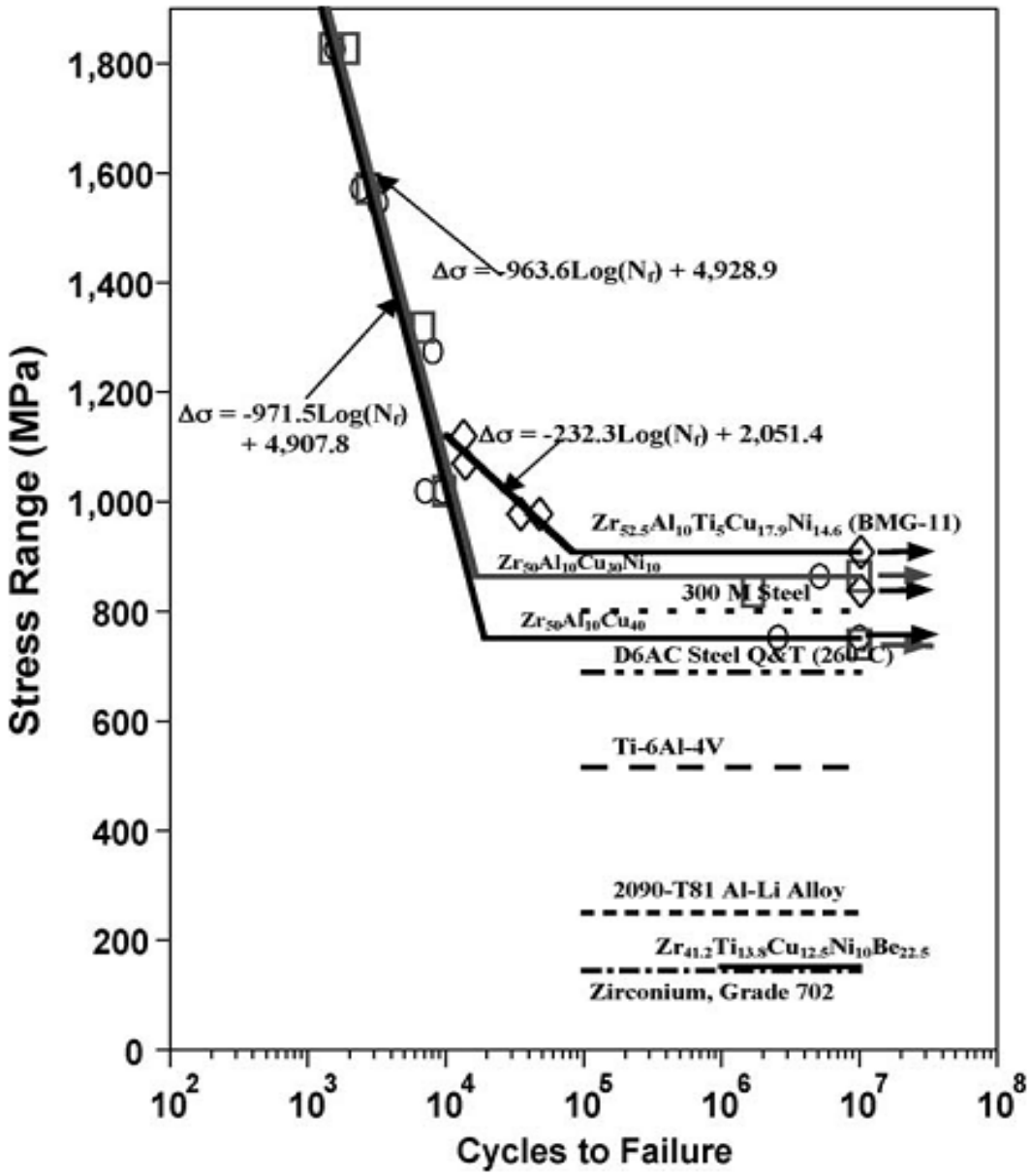

Figure 5. S-N fatigue curves of conventional crystalline alloys and Zr-based BMGs [9].[4]

[4] Reprinted from Intermetallics, 12, G. Y. Wang, P. K. Liaw, W. H. Peter, B. Yang, Y.Yokoyama, M. L. Benson, B. A. Green, M. J. Kirkham, S. A. White, T. A. Saleh, R. L. McDaniels, R. V. Steward, R. A. Buchanan, C. T. Liu and C. R. Brooks, Fatigue behavior of bulk-metallic glasses, 885-892, Copyright (2004), with permission from Elsevier.

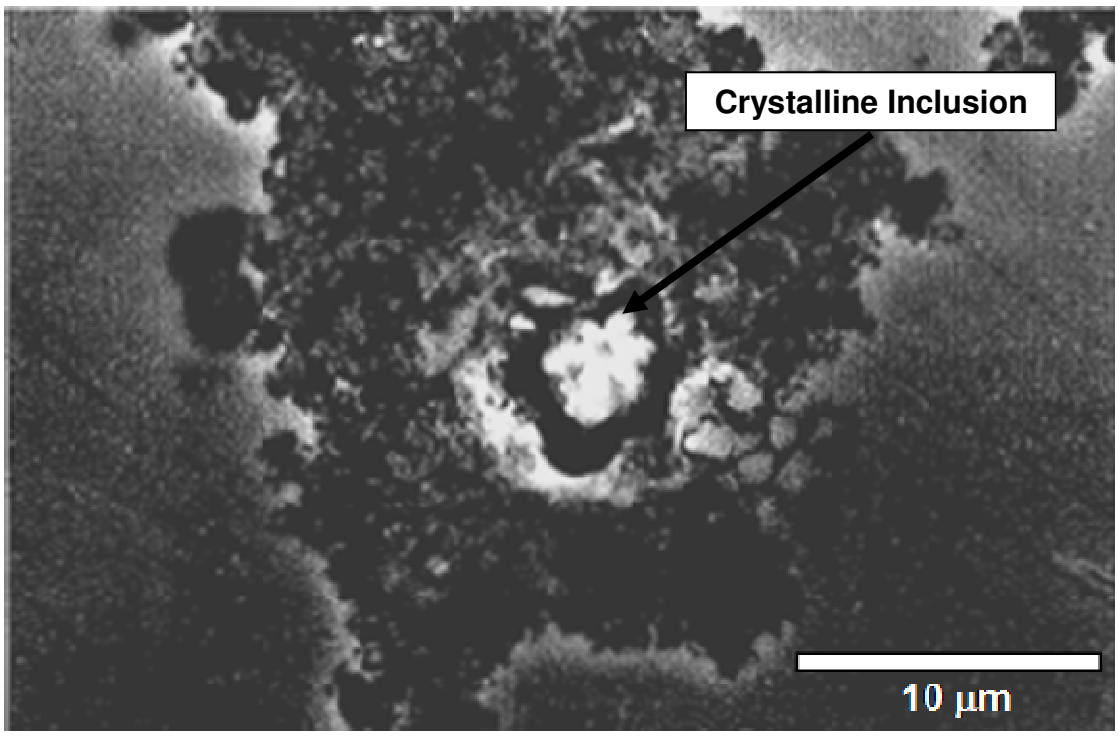

Figure 6. Scanning electron microscopy (SEM) image [11] demonstrating local attack generated at a crystalline inclusion in a $Zr_{55}Cu_{30}Al_{10}Ni_5$ amorphous alloy. The experiment was performed in a 10^{-3} M NaCl electrolyte.[5]

[5] A. Gebert, K. Mummert, J. Eckert, L. Schultz, and A. Inoue: Electrochemical investigations on the bulk glass forming $Zr_{55}Cu_{30}Al_{10}Ni_5$ alloy. Materials and Corrosion-Werkstoffe und Korrosion. 1997. 48. 293-297. Copyright Wiley-VCH Verlag GmbH & Co. KGaA. Reproduced with permission

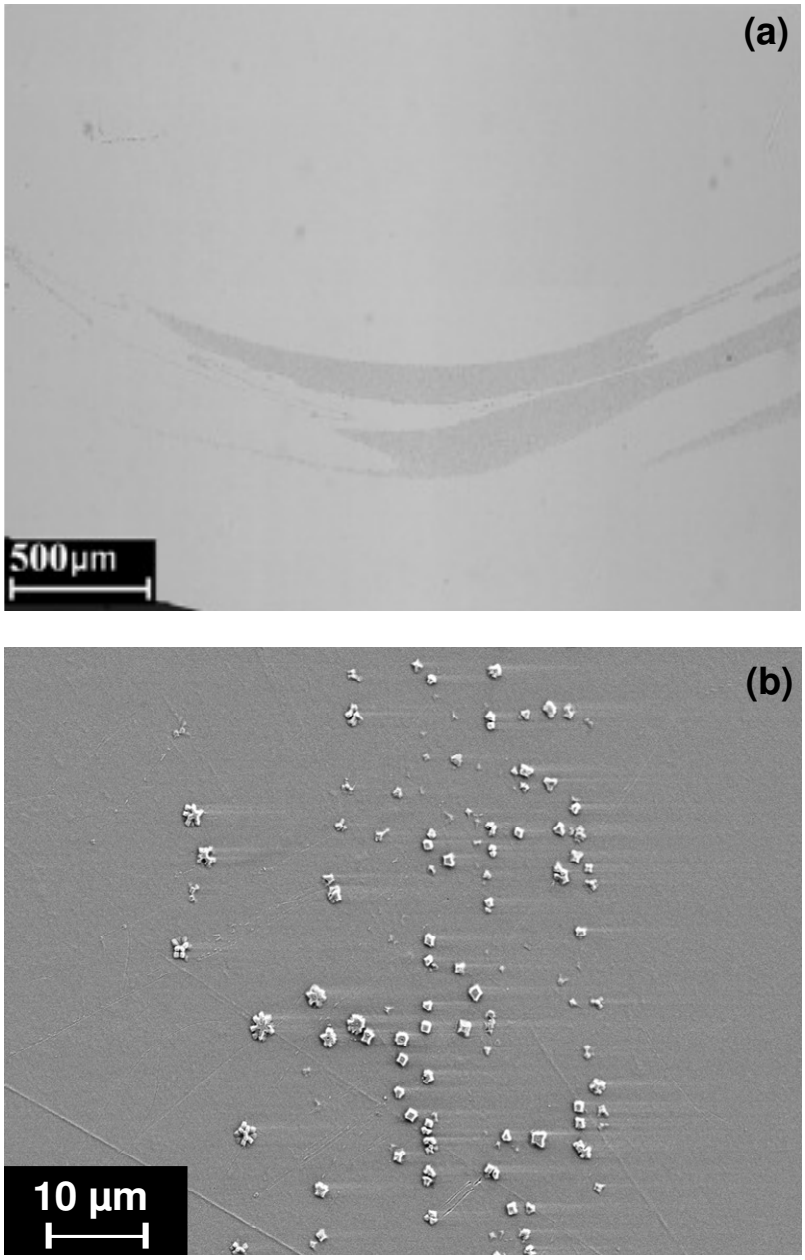

Figure 7 (a) Optical micrograph of a crystalline "swirl" region on the surface of Vitreloy 105 [106]. (b) SEM image of microstarlets on Vitreloy 105 [126].

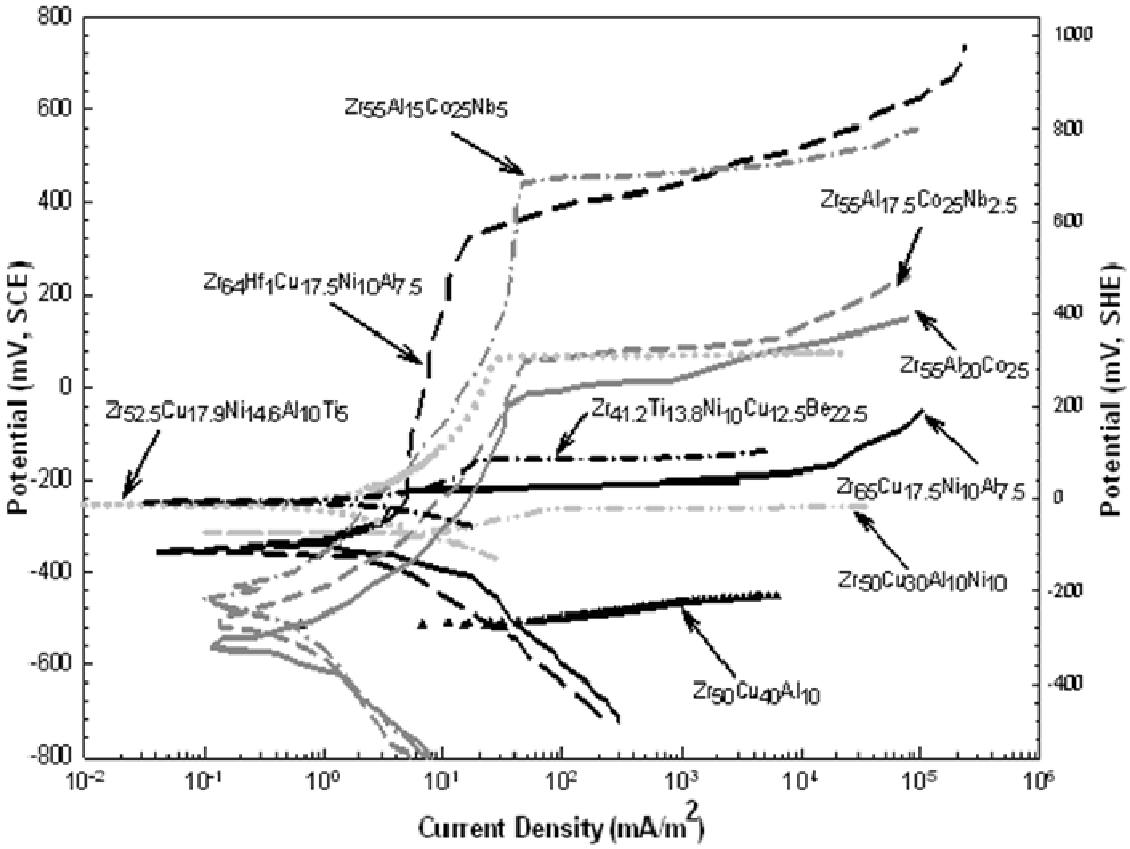

Figure 8. Polarization curves of selected Zr-based BMGs generated in 0.5 and 0.6 M NaCl electrolytes from various literature reports [15, 27, 97, 99, 103].[6]

[6] The figure was obtained from Bulk Metallic Glasses, 2007, M.K. Miller and P.K. Liaw (Eds), p 220, Chapter 8: Corrosion Behavior, B.A. Green, P.K. Liaw, and R.A. Buchanan, Figure 8-6, © 2008 Springer Science+Business Media, LLC With kind permission of Springer + Business Media.

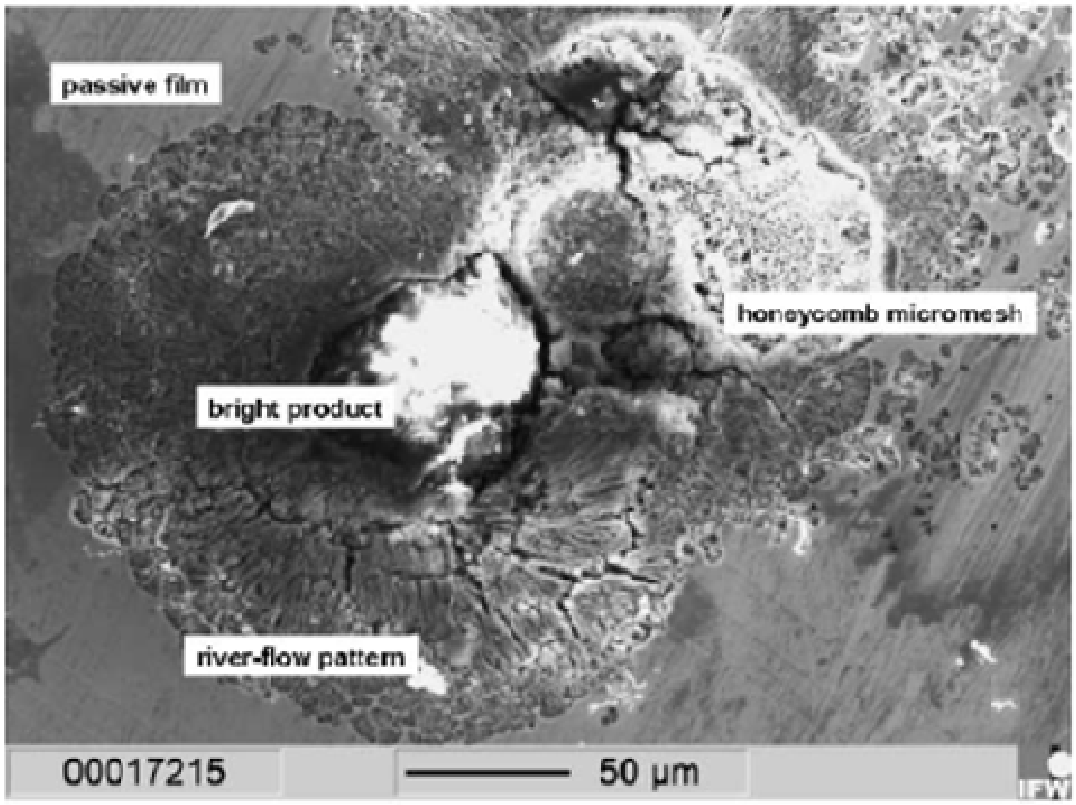

Figure 9. Corrosion pit on the surface of a $Zr_{59}Ti_3Cu_{20}Al_{10}Ni_8$ BMG illustrating cracked and honeycomb (porous) morphologies of pits [104].[7]

[7] The figure was Reprinted from Journal of Alloys and Compounds, 377, U. Kamachi Mudali, S. Baunack, J. Eckert, L. Schultz, and A. Gebert, Pitting corrosion of bulk glass-forming zirconium-based alloys, 290-297, Copyright (2004), with permission from Elsevier.

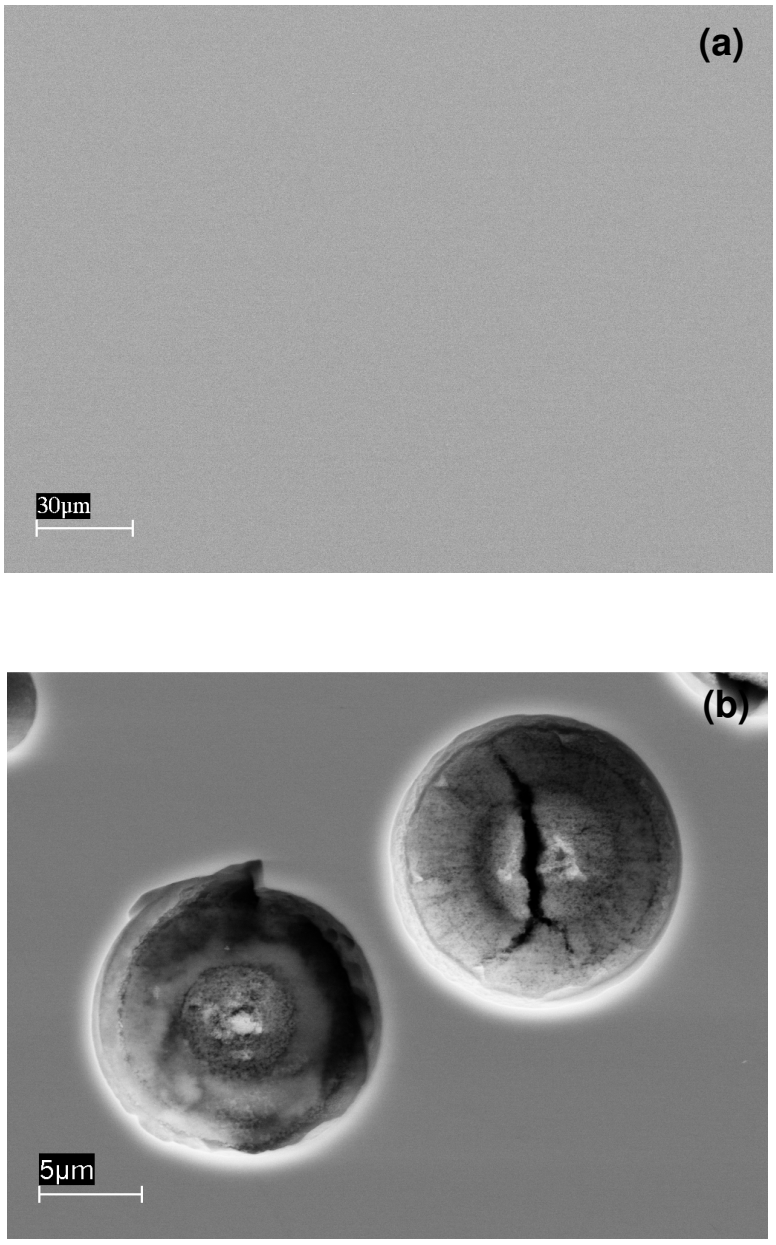

Figure 10. SEM images of Vitreloy 105 (a) before an anodic-polarization experiment and (b) after the anodic-polarization experiment [106].

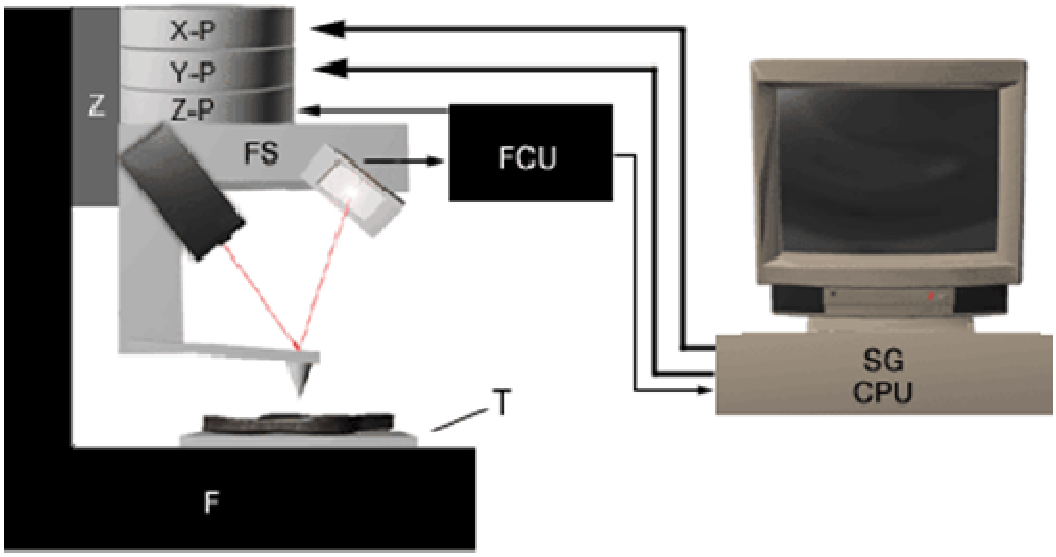

Figure 11. A schematic illustrating the components of an atomic force microscope (AFM). The x-, y-, and z piezoelectric devices are represented as X-P, Y-P, and Z-P, respectively. FS is the force sensor, and FCU is the feedback control unit. The frame of the AFM unit is denoted by F.[8]

[8] Image obtained from http://www.pacificnanotech.com/afm-tutorial_afm-instrumentation.html with permission granted by Pacific Nanotechnology, Inc.

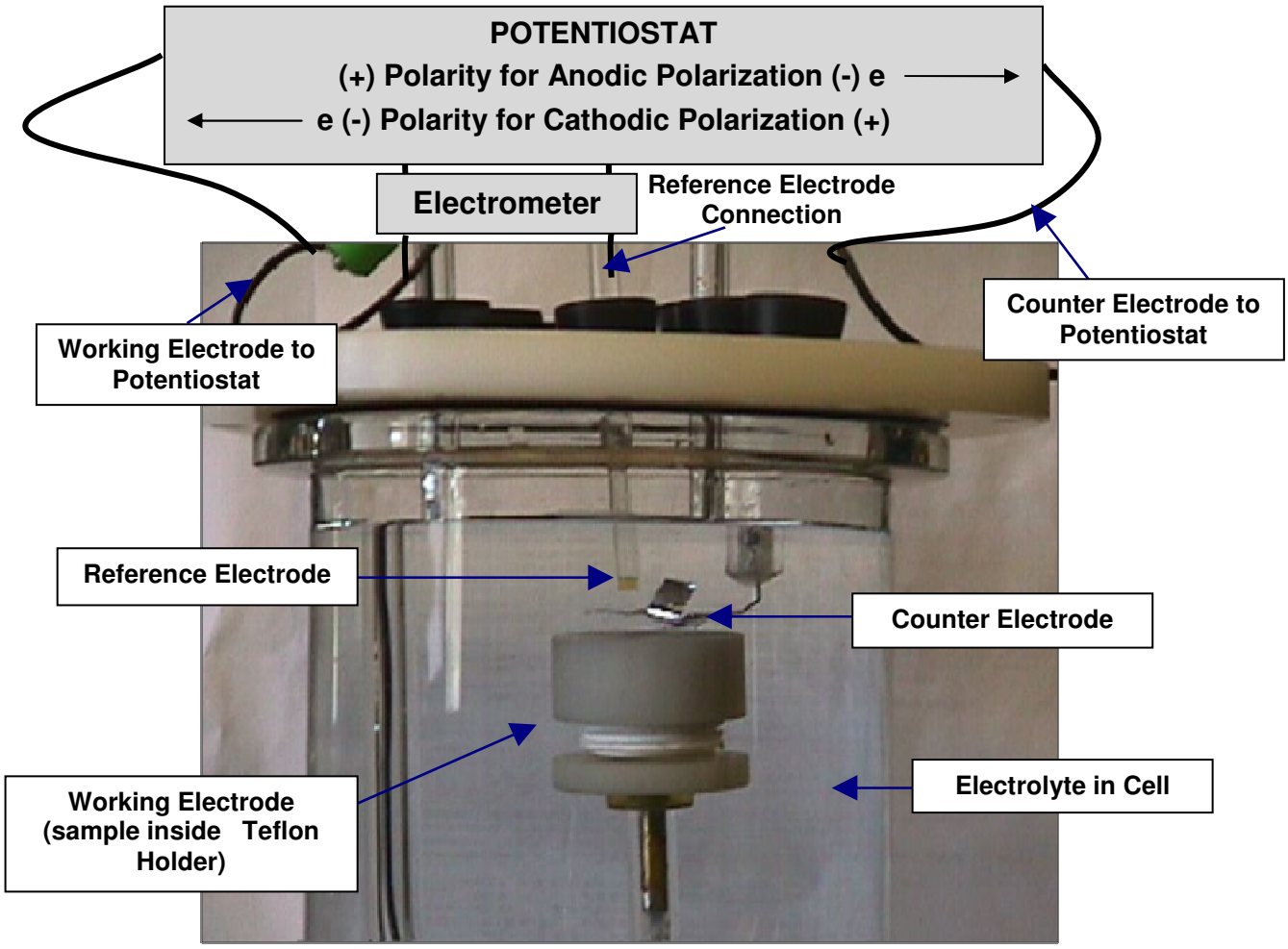

Figure 12. Components of the electrochemical cell.

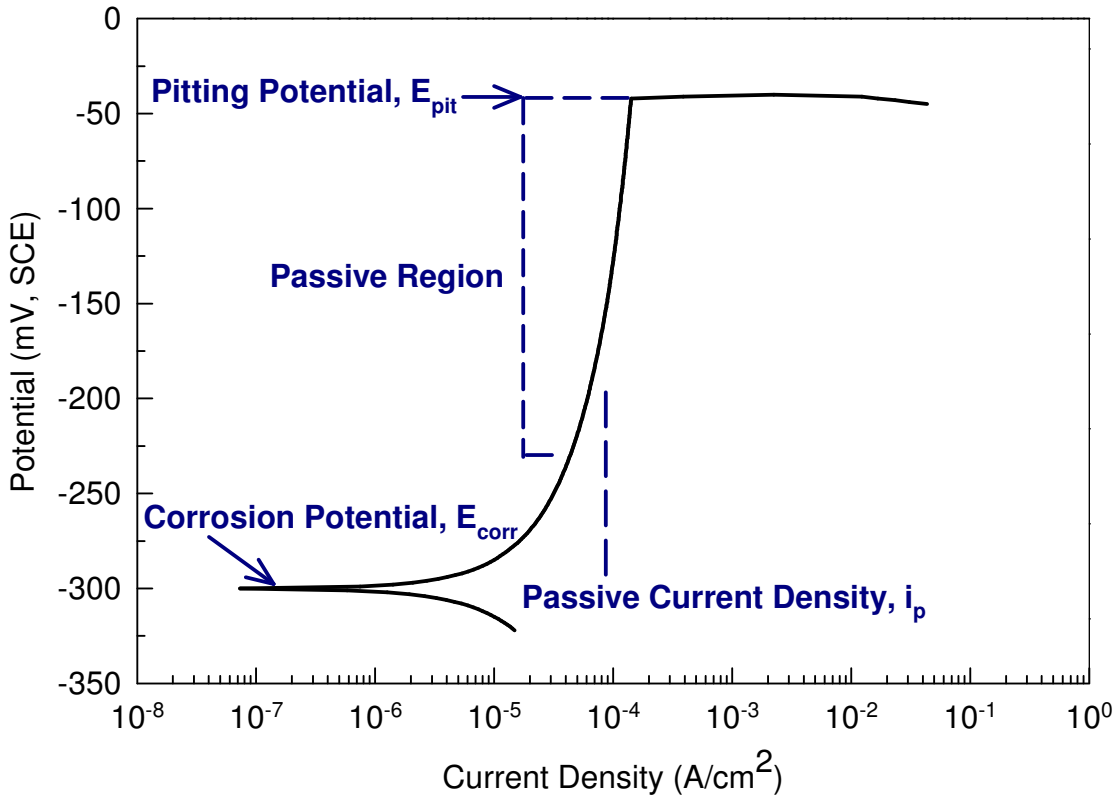

Figure 13. Polarization curve of a passivating alloy with important corrosion parameters denoted.

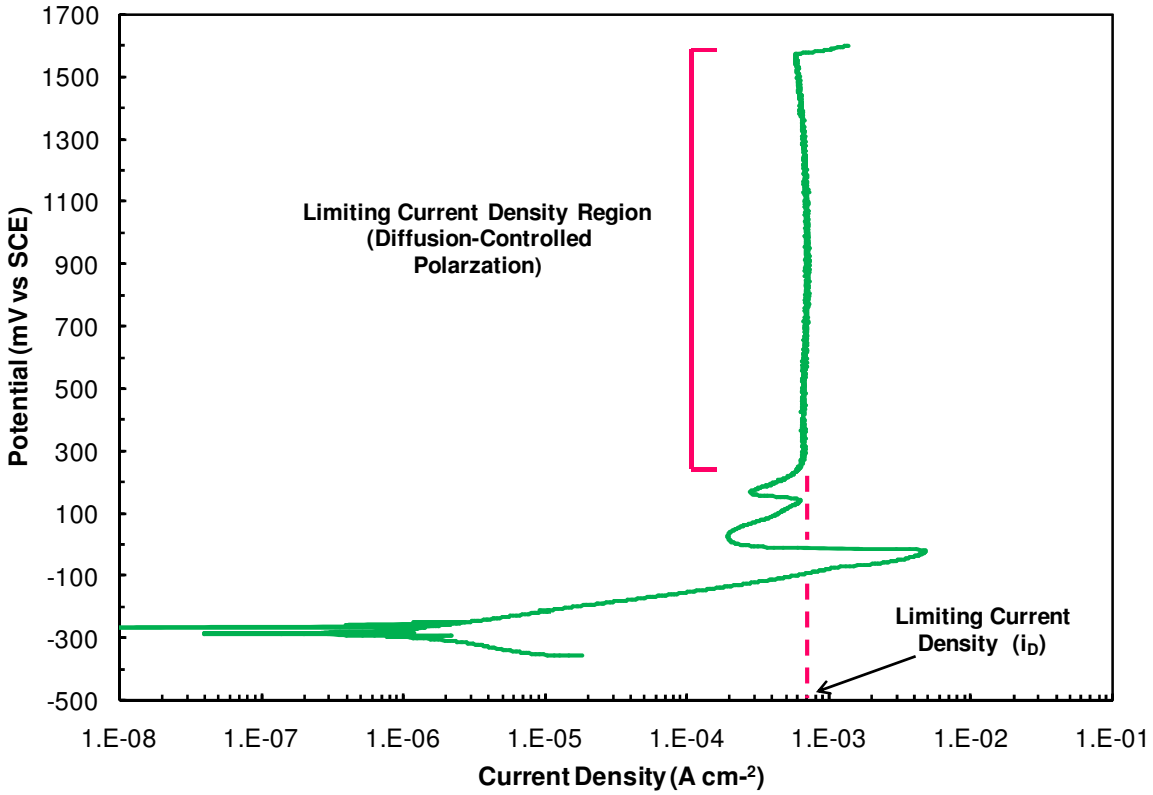

Figure 14. Polarization curve of a material that exhibits Tafel behavior with an anodic diffusion limiting current density.

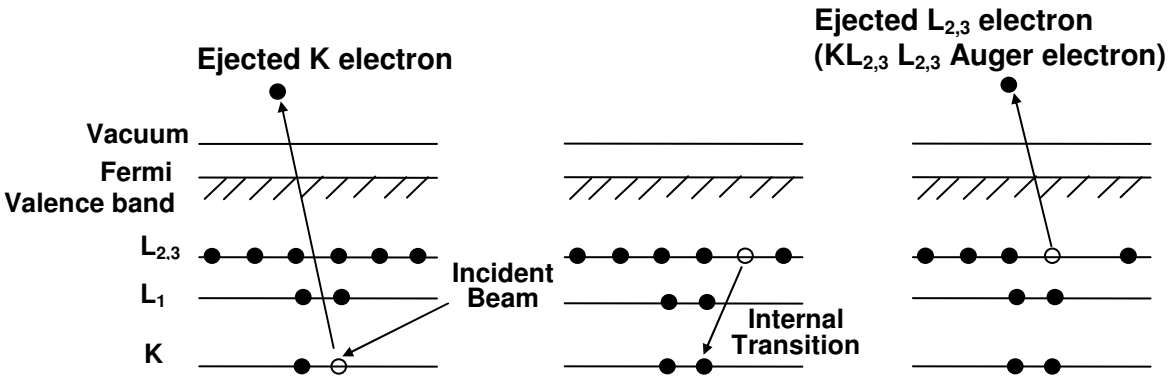

Figure 15. Relaxation process of a surface bombarded with an electron beam by the ejection of an Auger electron [50].[9]

[9] The figure was obtained from, An Introduction to Surface Analysis by XPS and AES, J. F. Watts and J. Wolstenholme, 2003, Copyright John Wiley & Sons Limited, Reproduced with permission.

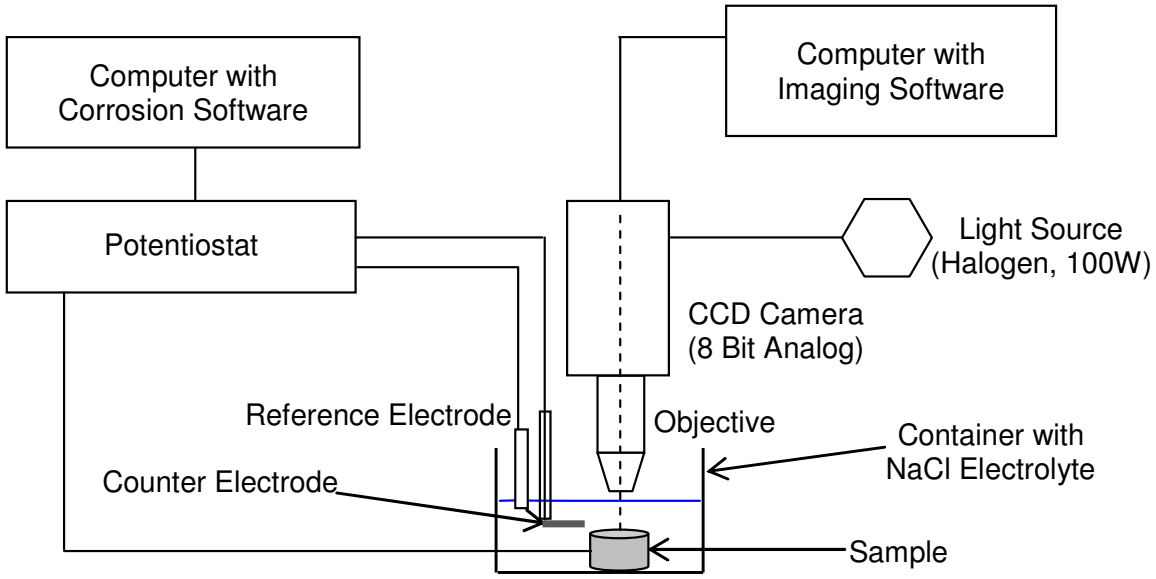

Figure 16. Experimental setup of the in-situ OM technique. The electrochemical cell is placed on the microscope stage. Electrodes from the electrochemical cell are connected to a potentiostat that is interfaced to a computer with corrosion software. The optical microscope is attached to a CCD camera that is interfaced to a computer containing a frame grabber.

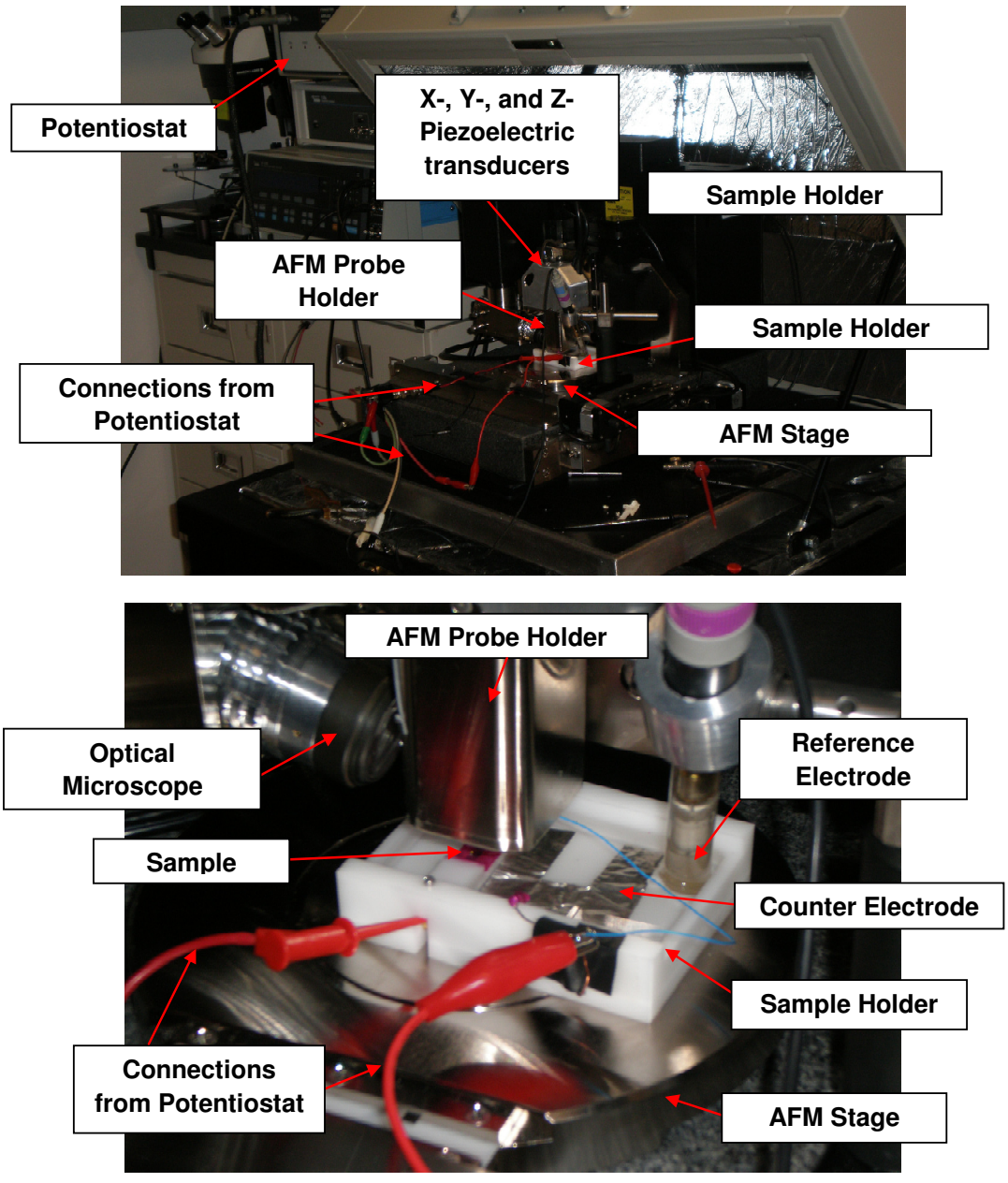

Figure 17. (a) View of the AFM in-situ corrosion set-up. (b) Close up of the AFM stage showing the AFM probe holder and the electrochemical cell within the sample holder. The holder houses the sample and the electrolyte.

Figure 18. (a) Front view of the sample holder for the AFM in-situ corrosion experiments. (b) Back view of the sample holder.

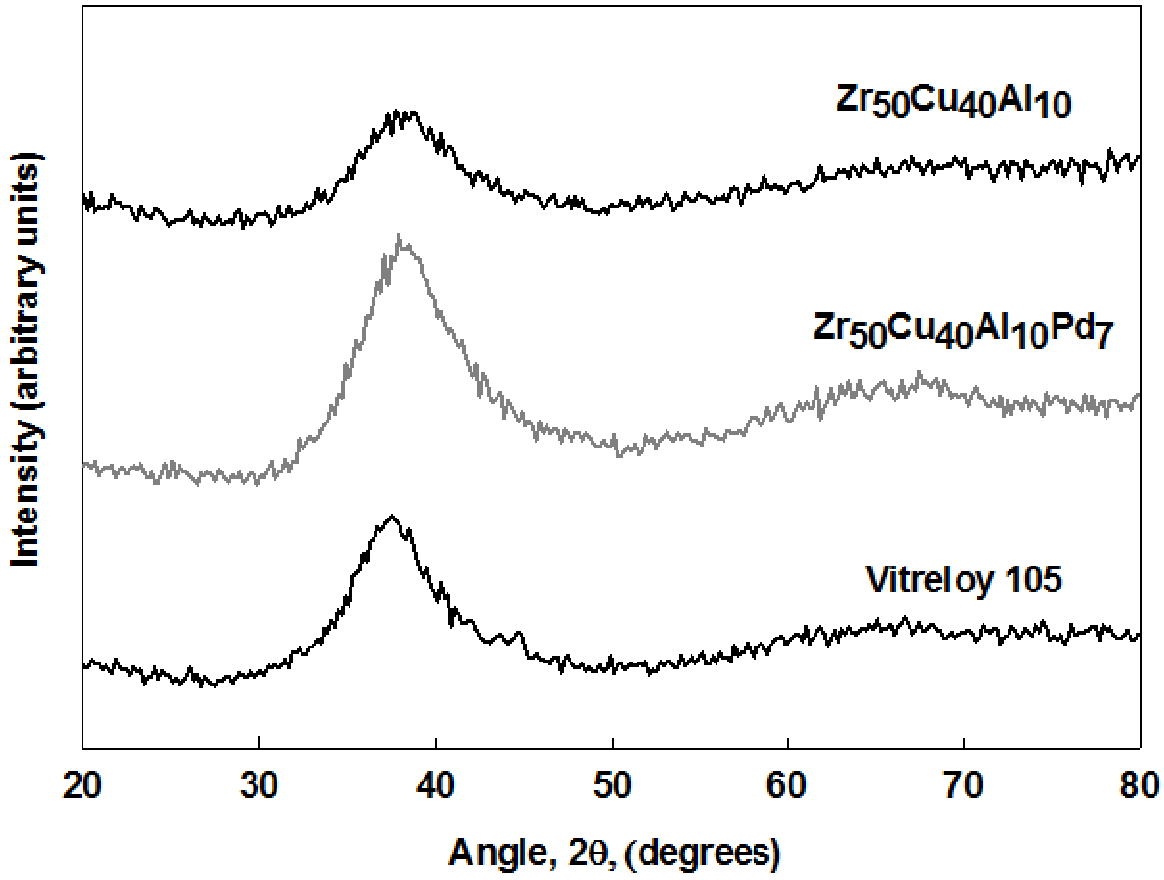

Figure 19. Representative XRD patterns for the $Zr_{50}Cu_{40}Al_{10}$, $Zr_{50}Cu_{33}Al_{10}Pd_7$, and Vitreloy 105 BMGs.

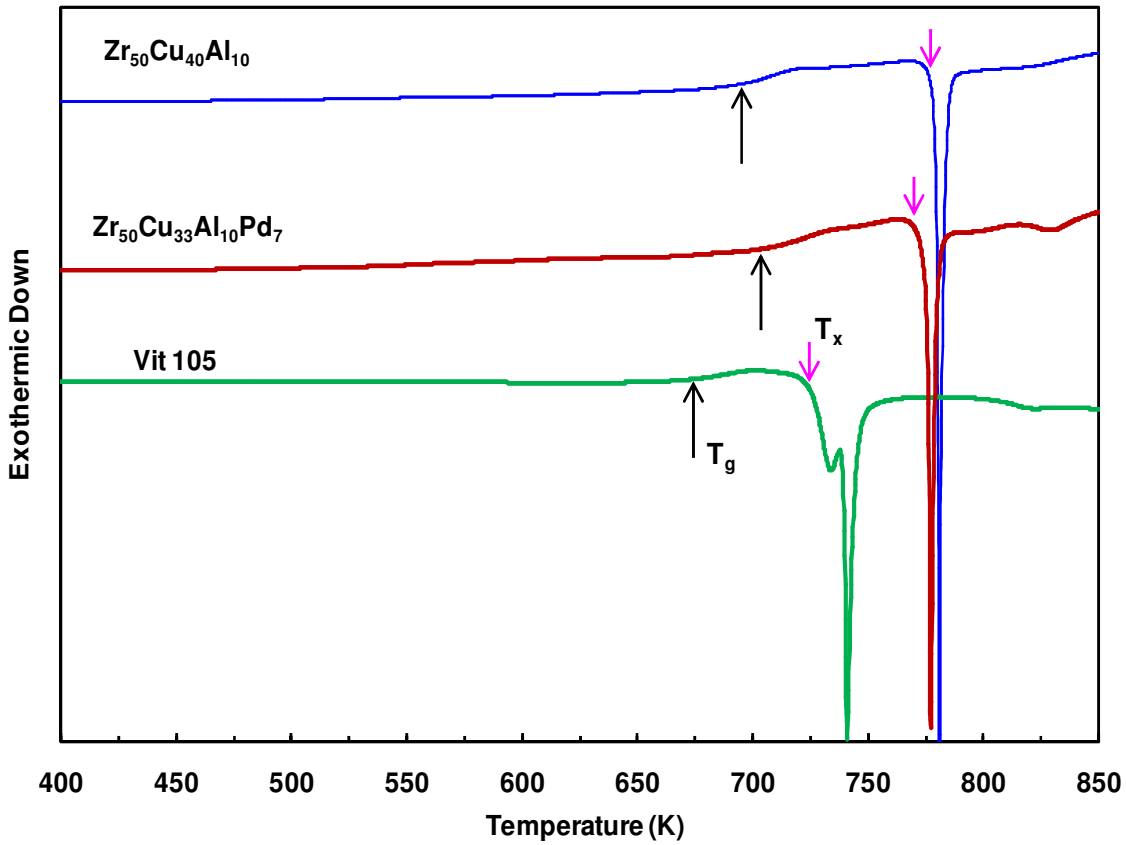

Figure 20. Representative DSC thermograms of $Zr_{50}Cu_{40}Al_{10}$, $Zr_{50}Cu_{33}Al_{10}Pd_7$, and Vitreloy 105 indicating T_g and T_x.

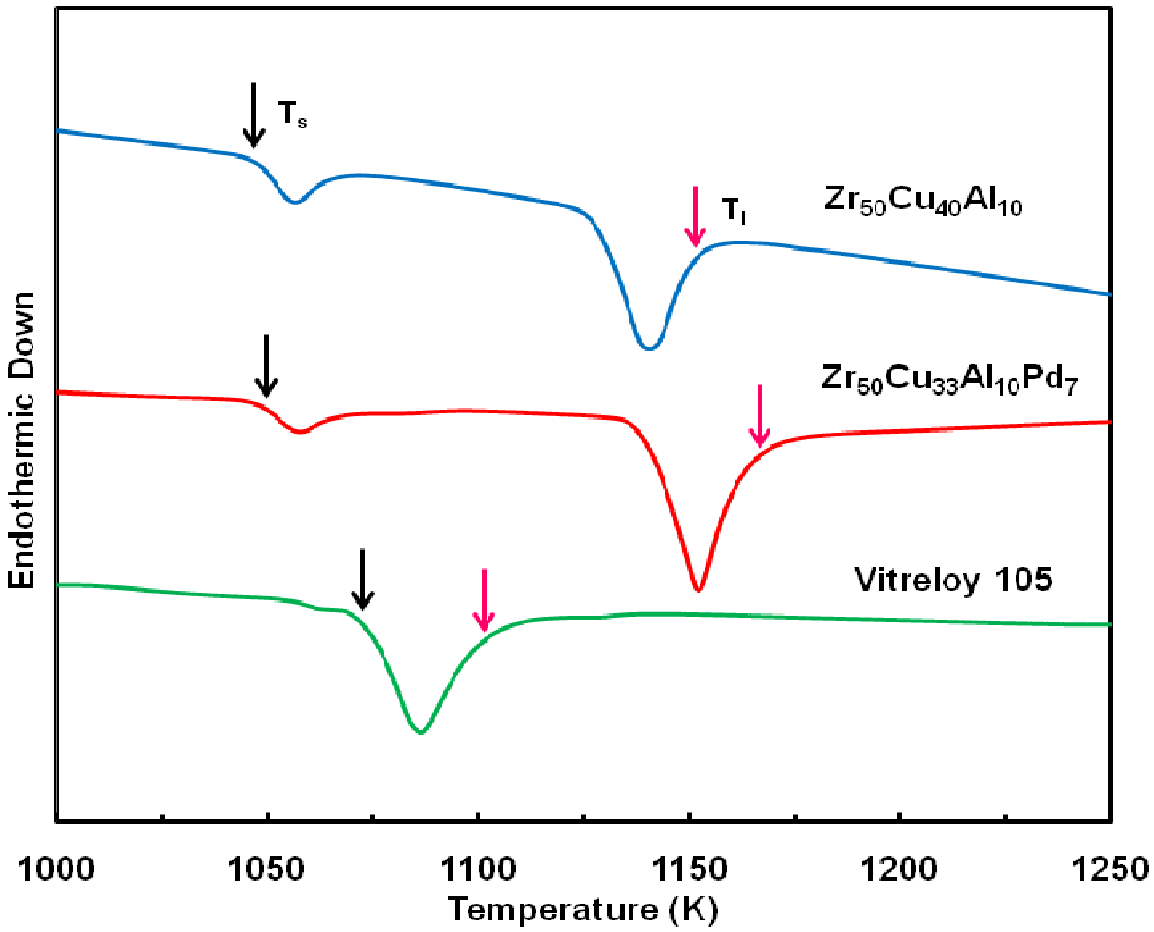

Figure 21. Thermograms of fusion of $Zr_{50}Cu_{40}Al_{10}$, $Zr_{50}Cu_{33}Al_{10}Pd_7$, and Vitreloy 105 generated with DTA. Black and pink arrows denote the solidus temperature (T_s) and liquidus temperature (T_l), respectively, for each alloy.

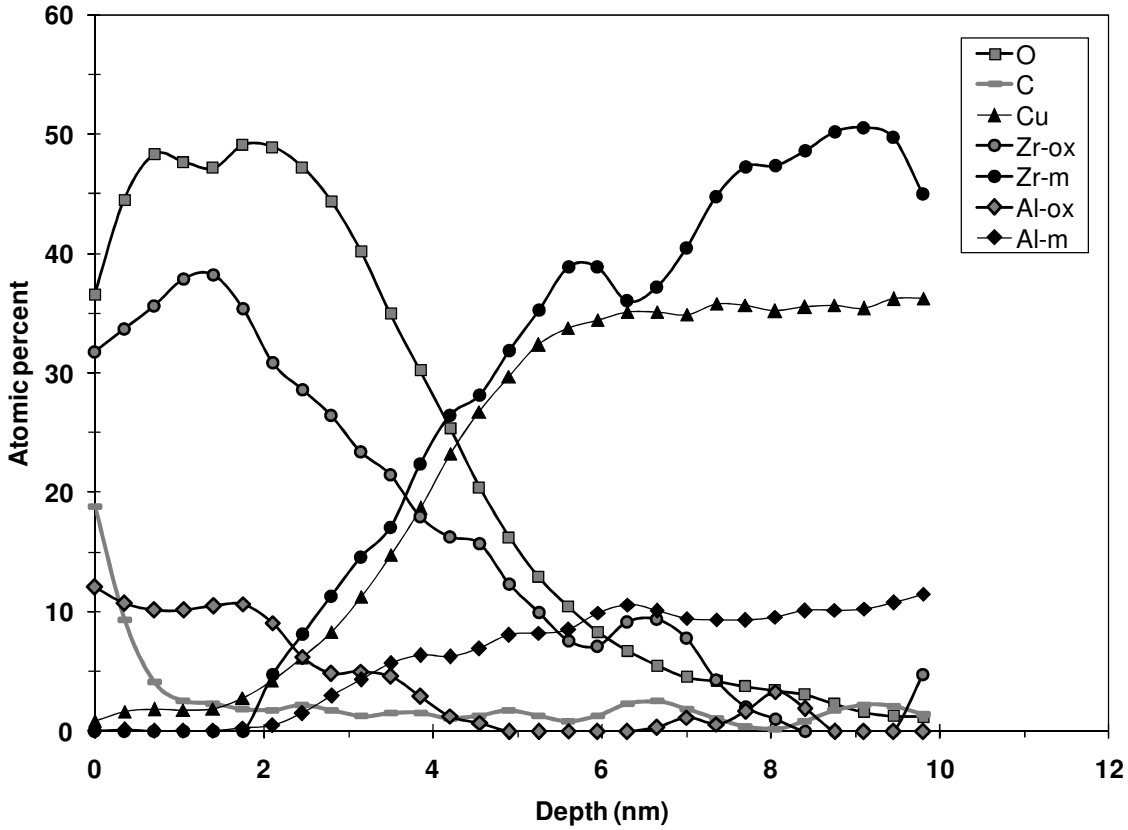

Figure 22. Auger sputter depth profiles of the as-received $Zr_{50}Cu_{40}Al_{10}$ BMG. Sputter rate = 0.025 nm/s.

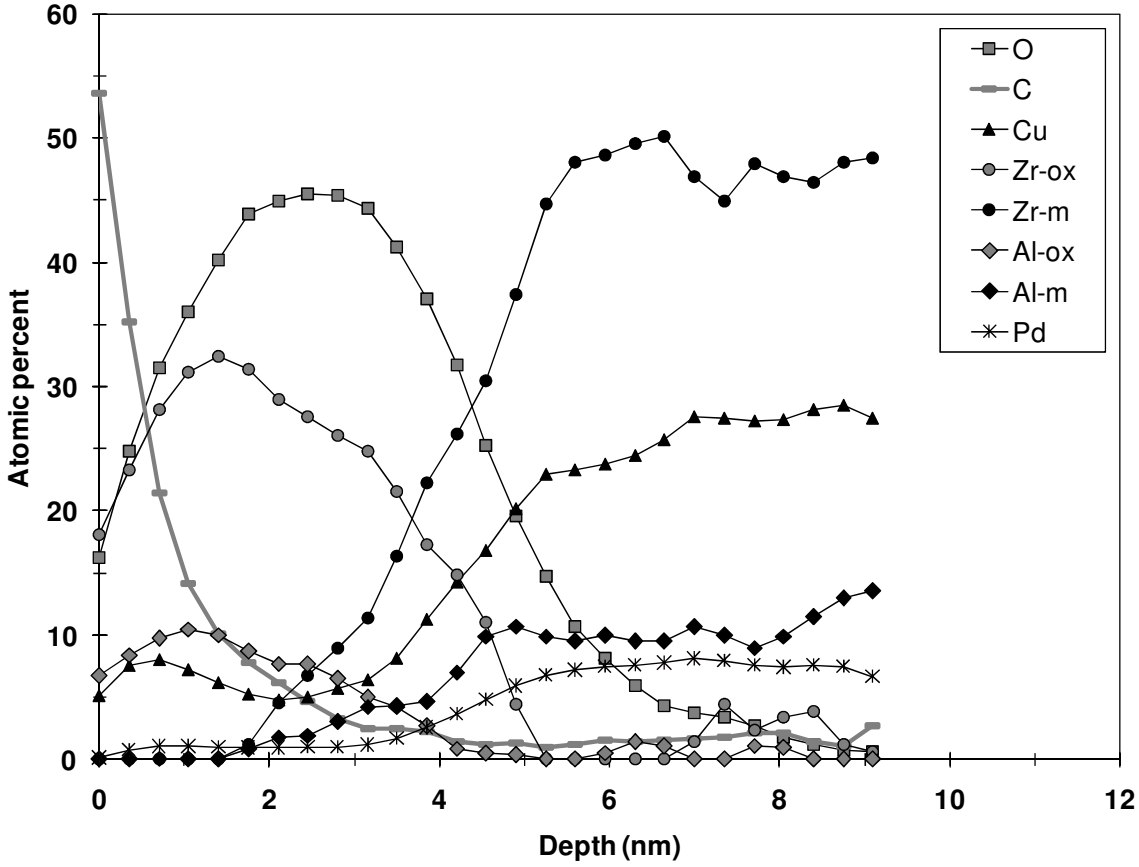

Figure 23. Auger sputter depth profiles of the as-received $Zr_{50}Cu_{33}Al_{10}Pd_7$ BMG. Sputter rate = 0.025 nm/s.

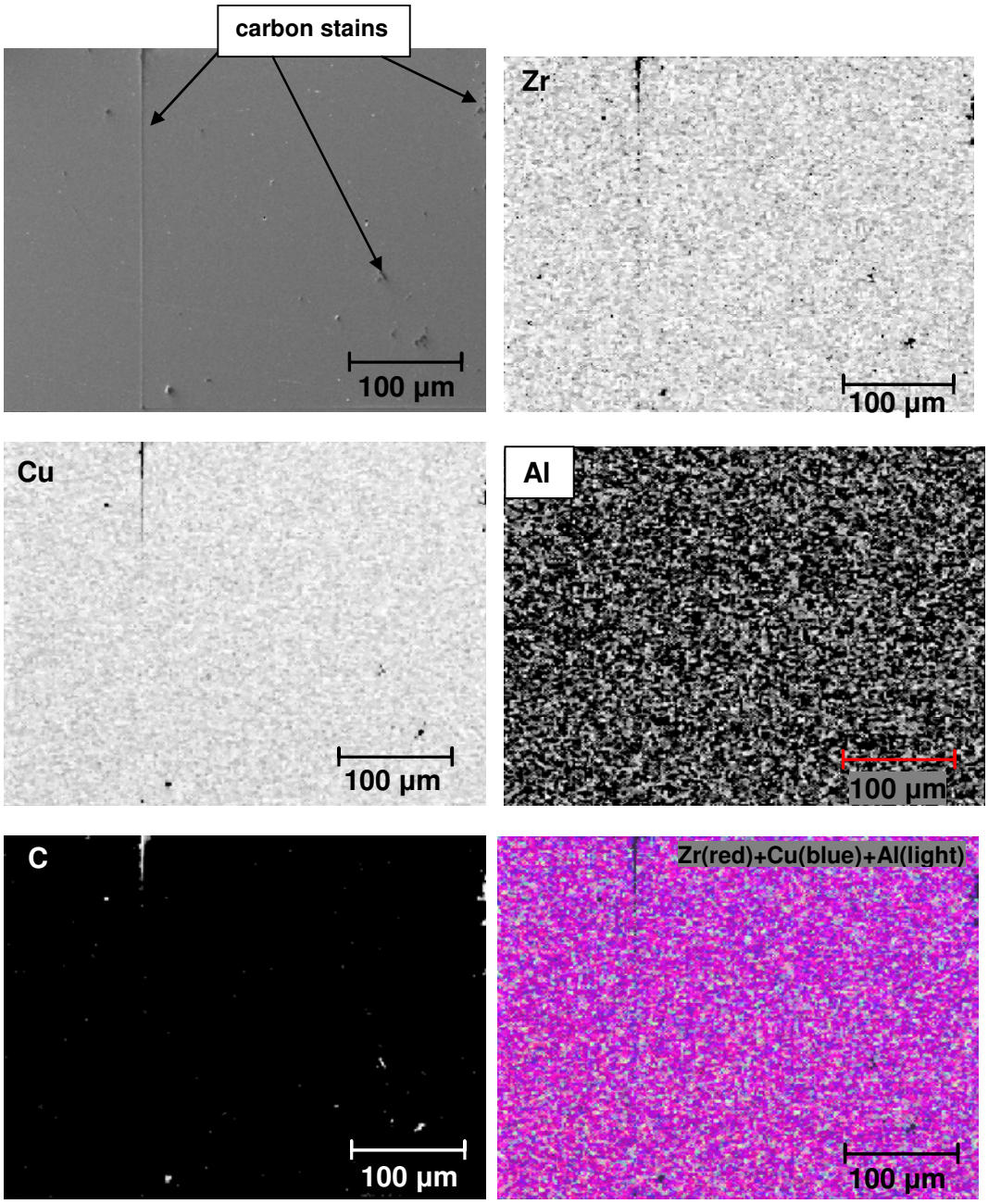

Figure 24. (top left) SEM image of the as-polished surface of $Zr_{50}Cu_{40}Al_{10}$ after sputter etching. Zr, Cu, Al, C Auger elemental maps of the surface are presented. A combined Auger map of Zr, Cu, and Al is also shown (lower right).

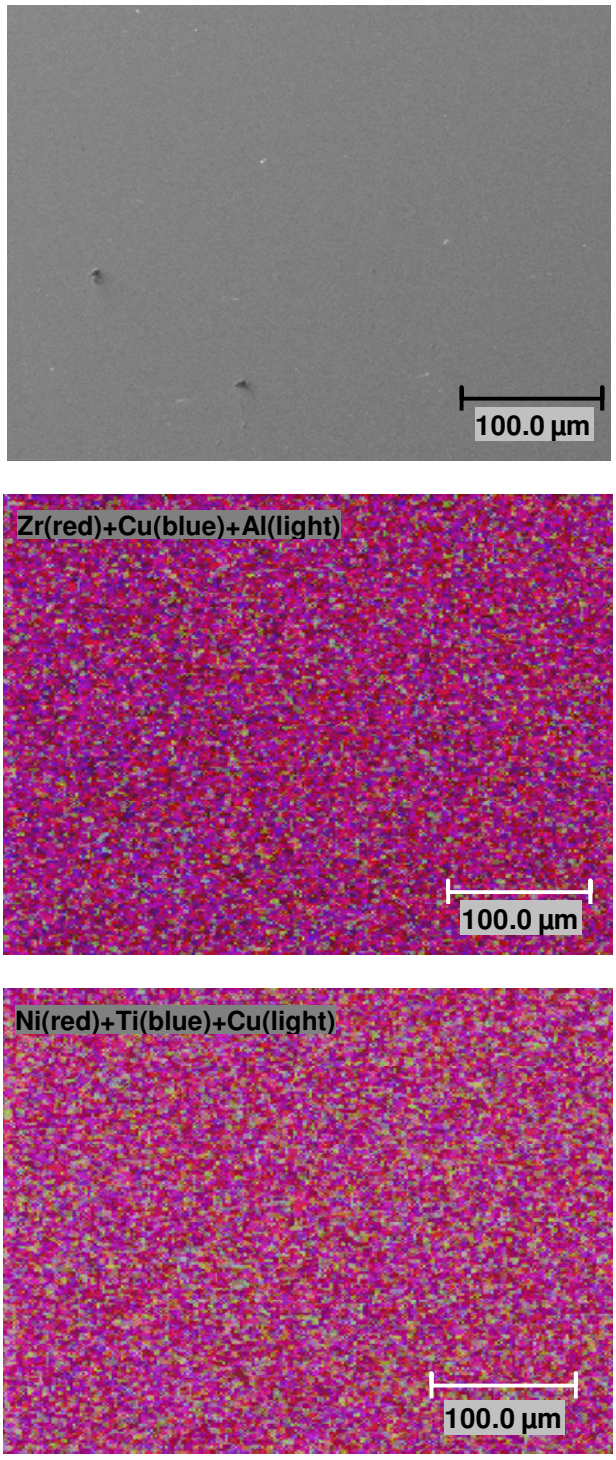

Figure 25. SEM image of the as-polished surface of Vitreloy 105 after sputter etching. Auger combined maps of the area are displayed.

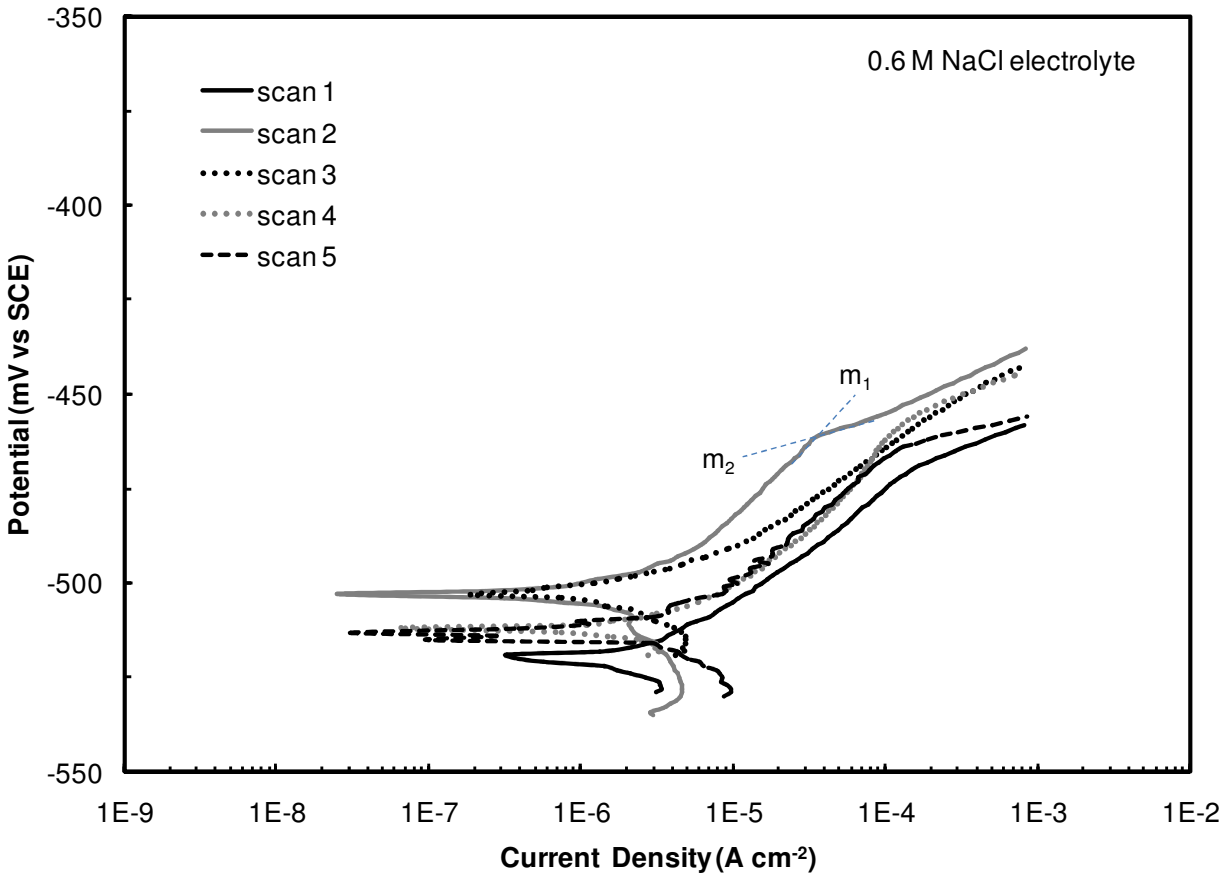

Figure 26. Polarization curves of $Zr_{50}Cu_{40}Al_{10}$ generated in naturally aerated 0.6 M NaCl electrolytes. The initial and final slopes (m_1 and m_2, respectively) are indicated on scan 2.

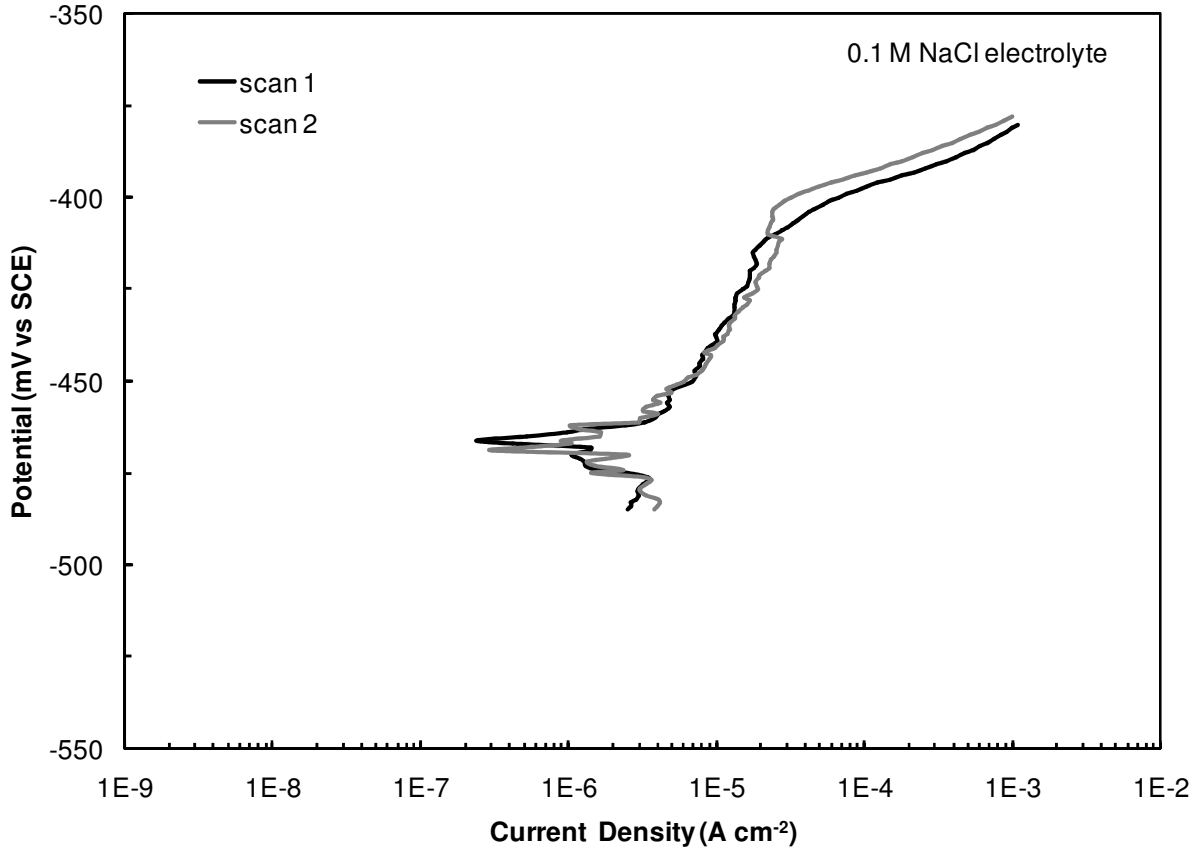

Figure 27. Polarization curves of $Zr_{50}Cu_{40}Al_{10}$ generated in naturally aerated 0.1 M NaCl electrolytes.

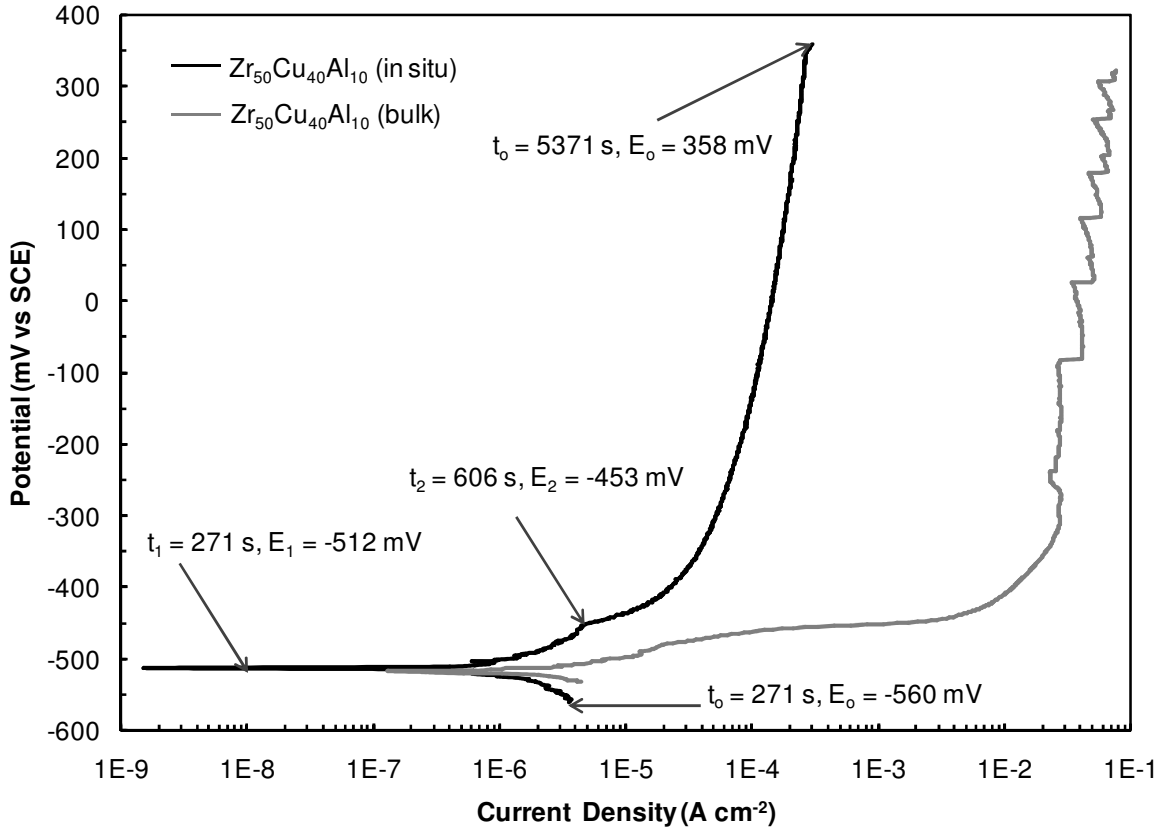

Figure 28. Representative polarization curves of $Zr_{50}Cu_{40}Al_{10}$ obtained from an in-situ experiment in 0.6 M NaCl (black curve) and from a bulk experiment in 0.6 M NaCl. Both experiments were performed open to air.

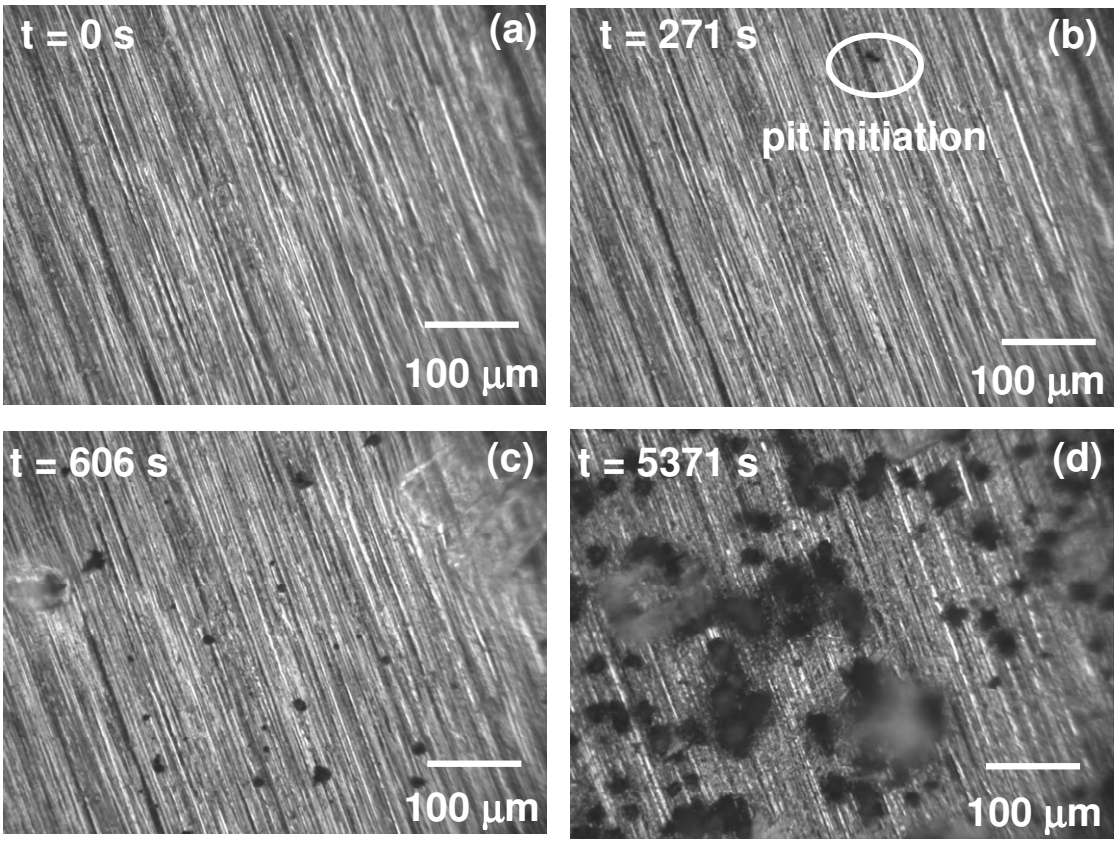

Figure 29. OM dark-field images (a) – (d) corresponding to the four conditions denoted on the polarization curve in Figure 28.

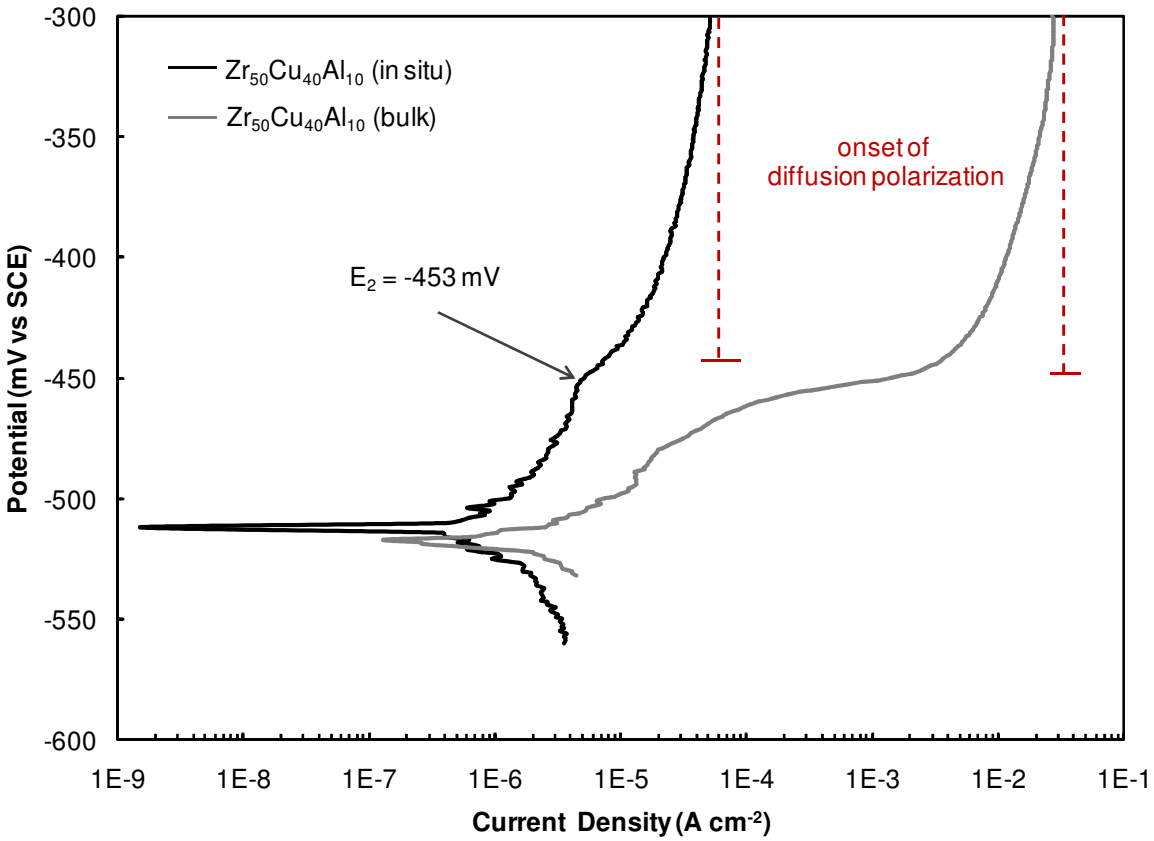

Figure 30. Magnification of Figure 28 indicating the onset of diffusion (concentration) polarization for $Zr_{50}Cu_{40}Al_{10}$ polarization curves generated in the in situ setup and in a bulk volume of solution.

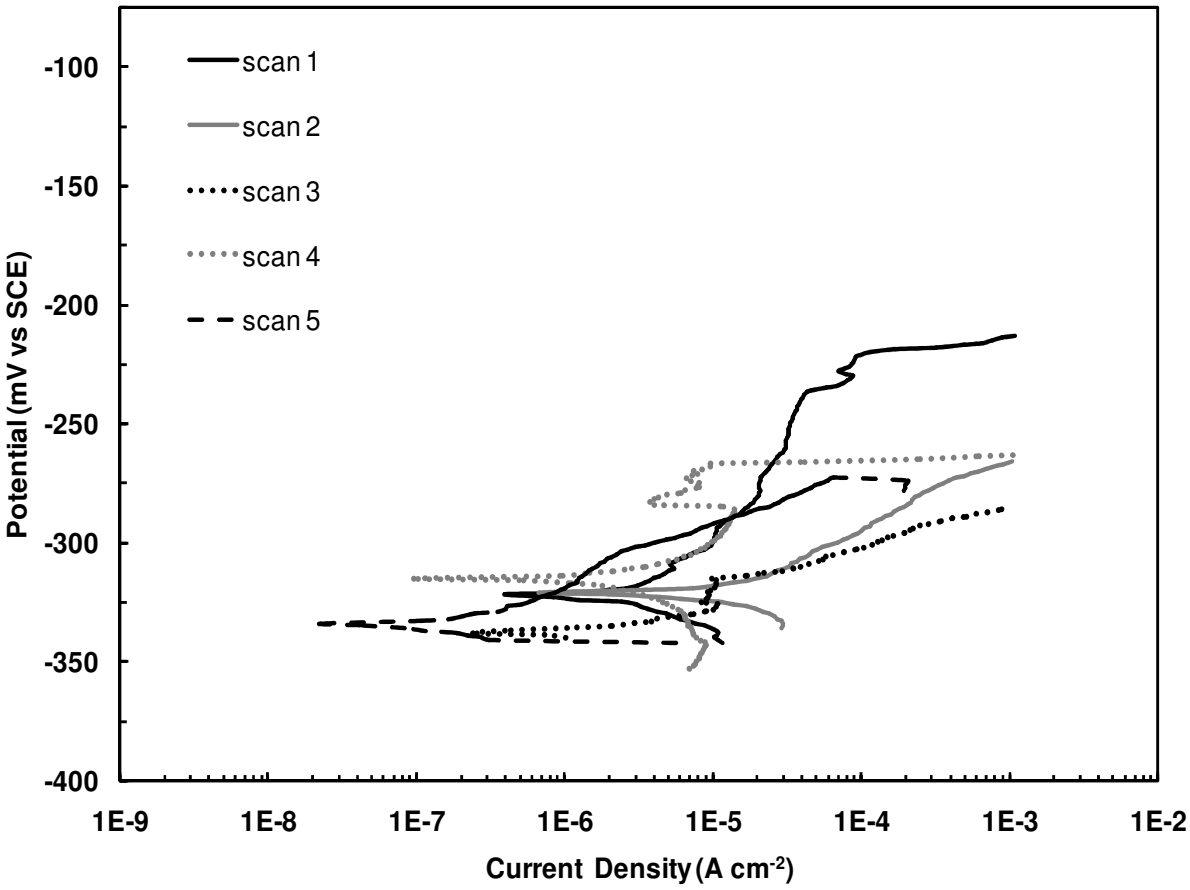

Figure 31. Polarization curves of $Zr_{50}Cu_{33}Al_{10}Pd_7$ generated in naturally aerated 0.6 M NaCl electrolytes.

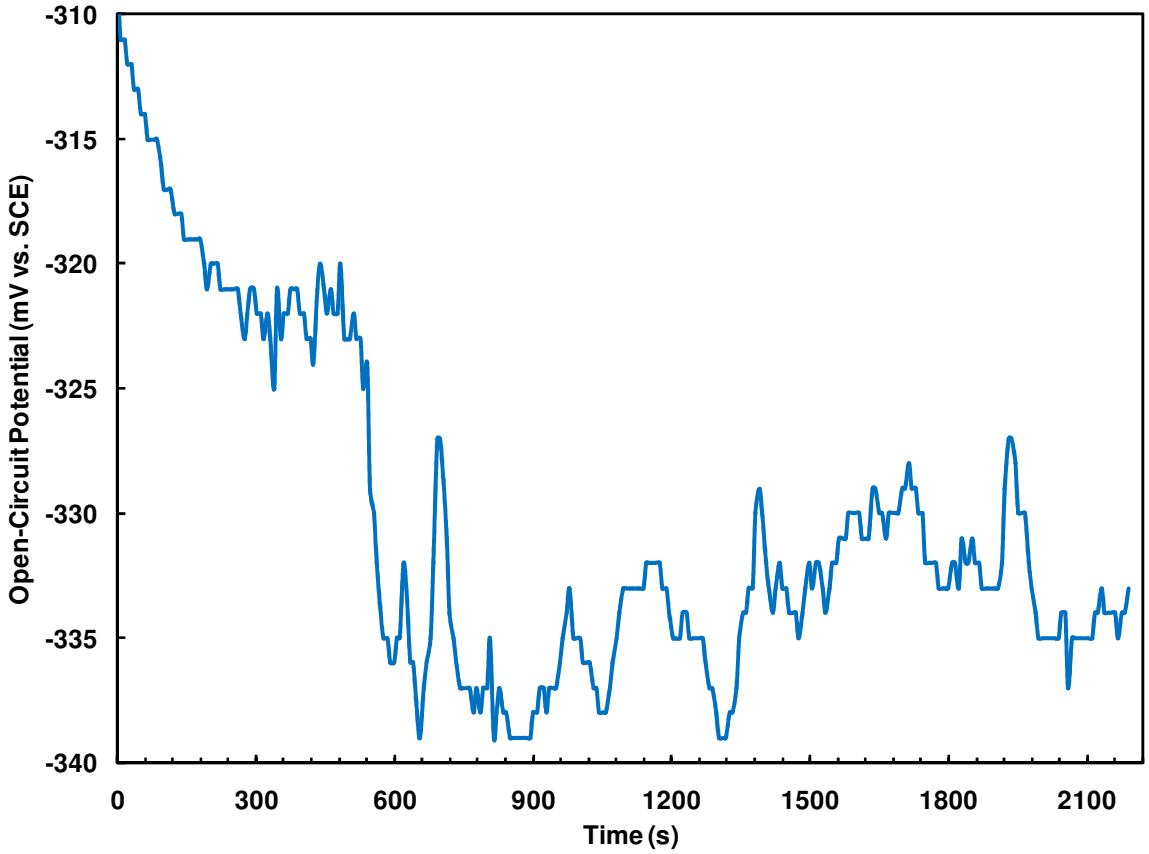

Figure 32. Open-circuit potential versus time potential illustrating the variation of the E_{corr} of $Zr_{50}Cu_{33}Al_{10}Pd_7$ in a naturally aerated 0.6 M NaCl electrolyte.

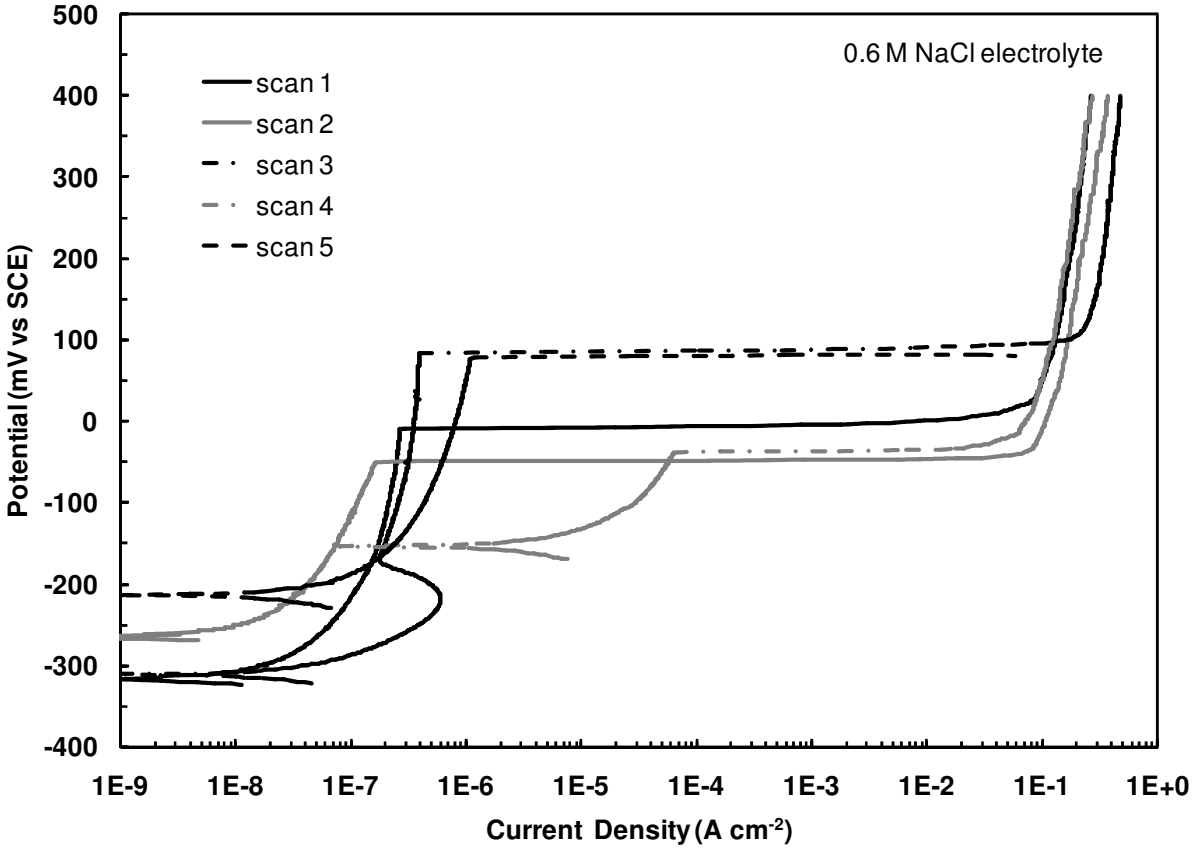

Figure 33. Polarization curves of Vitreloy 105 generated in naturally aerated 0.6 M NaCl electrolytes.

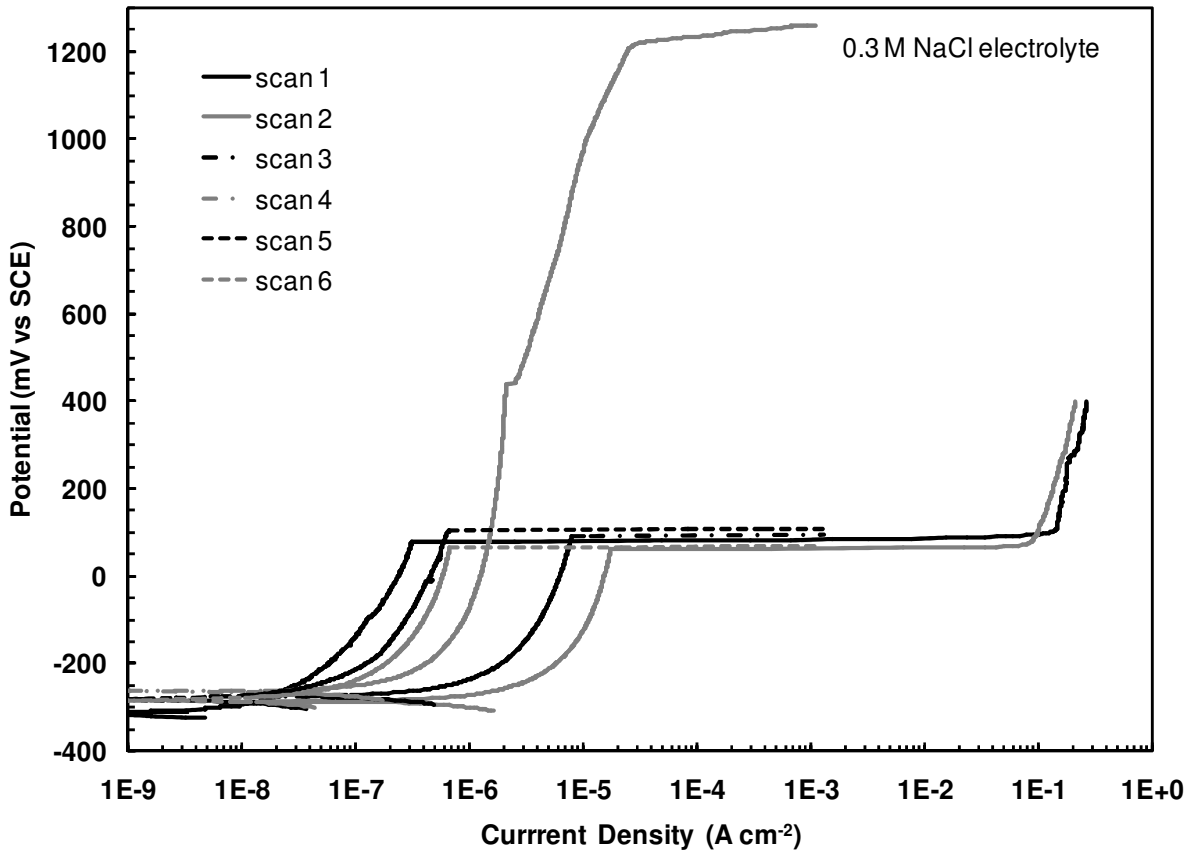

Figure 34. Polarization curves of Vitreloy 105 generated in naturally aerated 0.3 M NaCl electrolytes.

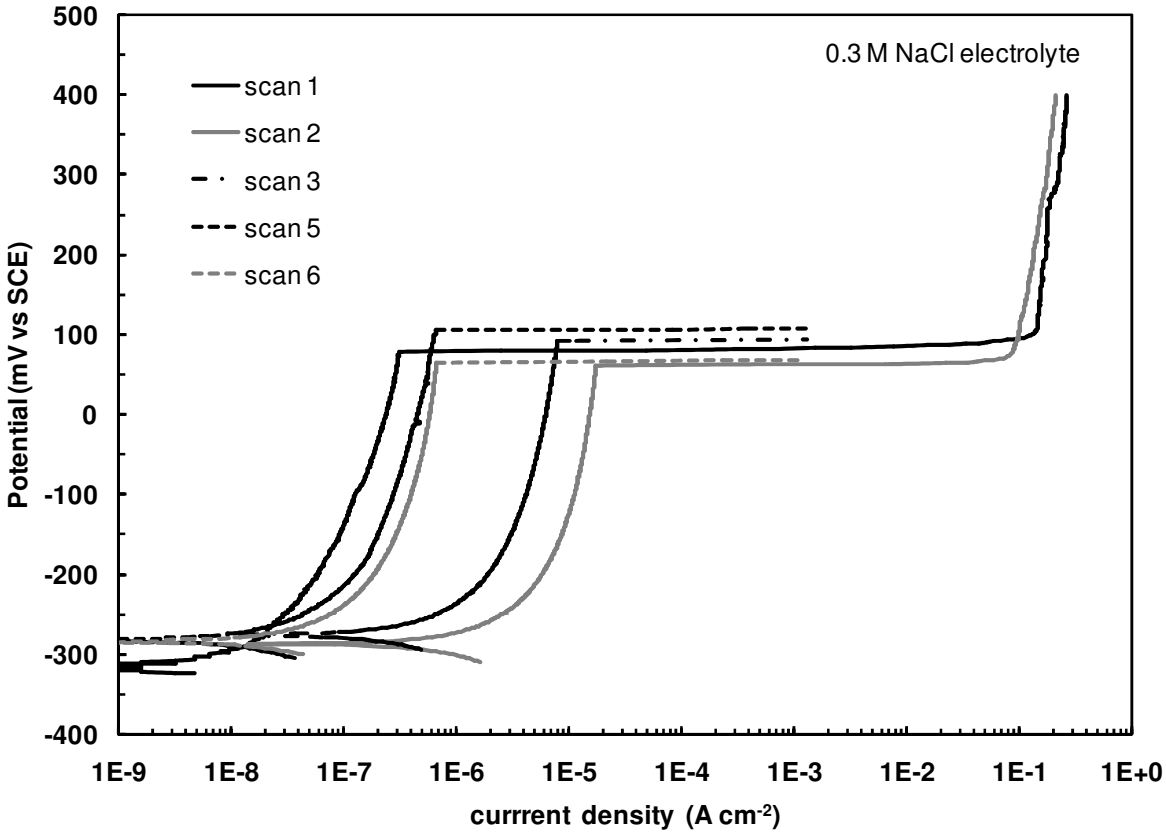

Figure 35. Polarization curves of Vitreloy 105 generated in naturally aerated 0.3 M NaCl electrolytes excluding the outlier (scan 4).

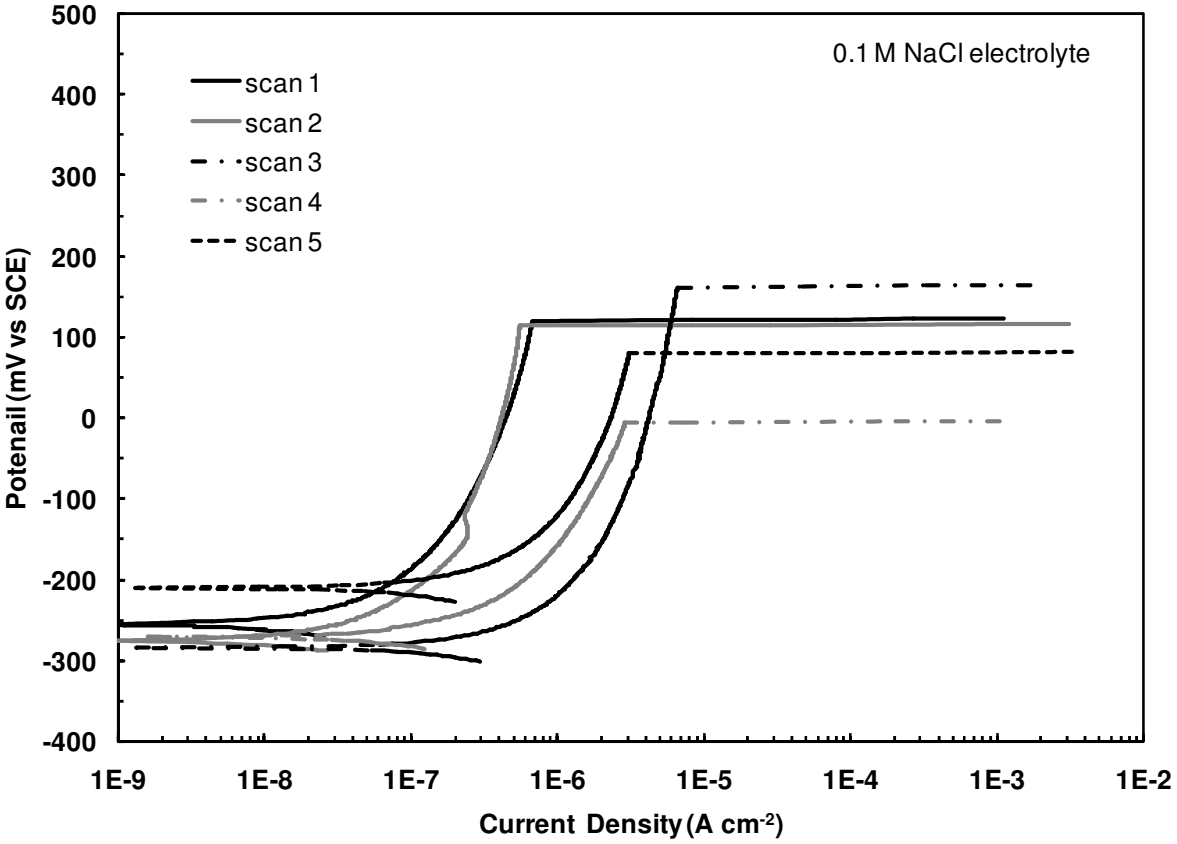

Figure 36. Polarization curves of Vitreloy 105 generated in naturally aerated 0.1 M NaCl.

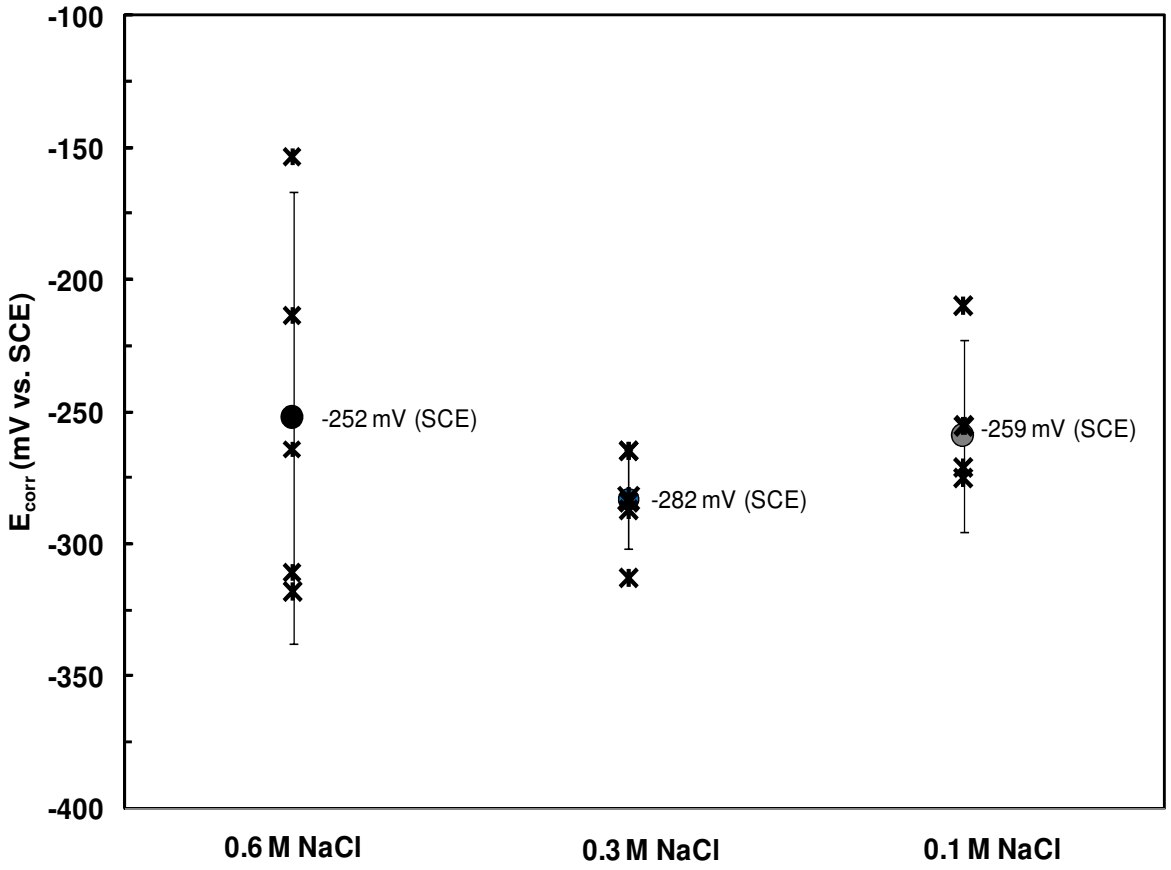

Figure 37. Corrosion potentials (E_{corr}) of Vitreloy 105 as a function of chloride concentration. Circles and error bars represent mean values and 95% confidence intervals, respectively.

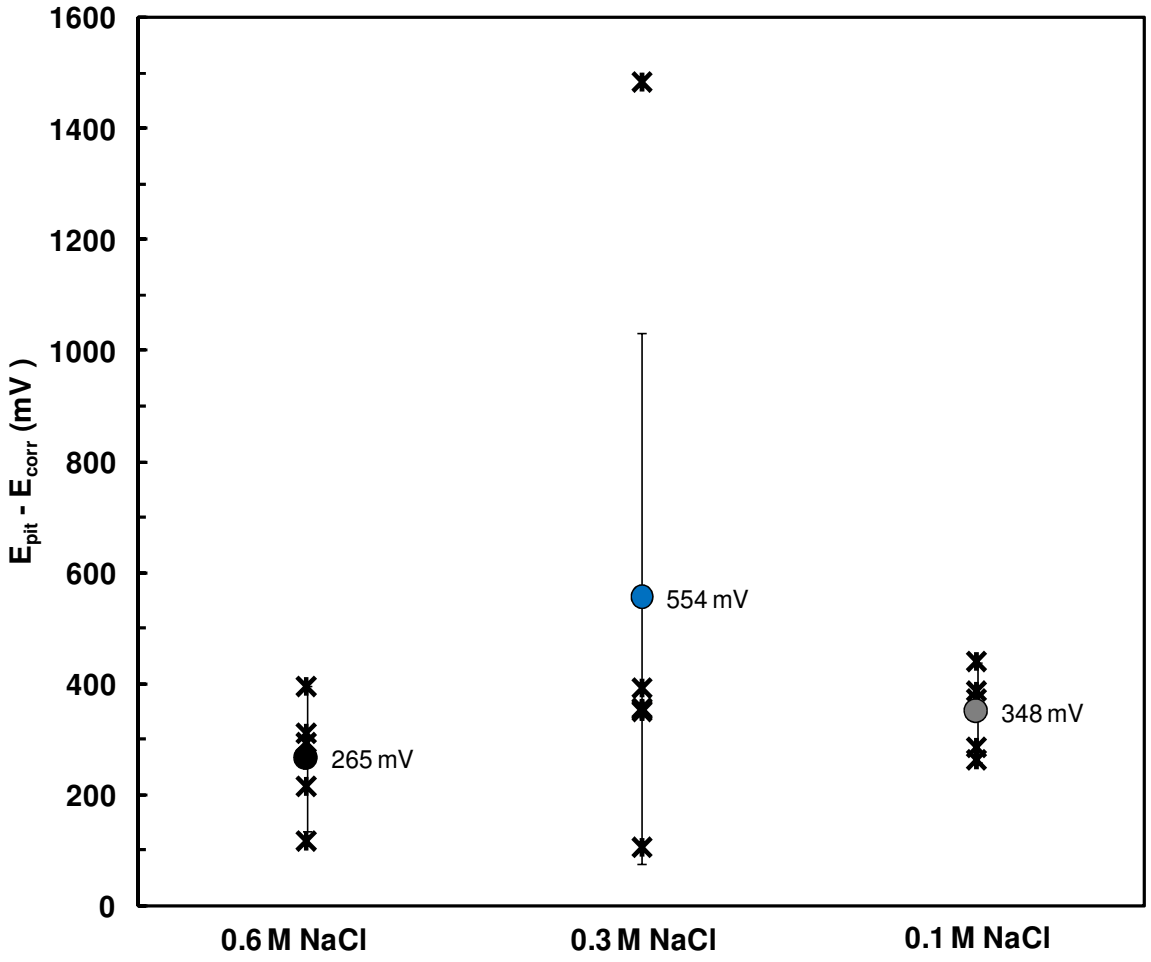

Figure 38. The pitting resistance parameters (E_{pit} –E_{corr}) of Vitreloy 105 as a function of chloride concentration. Circles and error bars represent mean values and 95% confidence intervals, respectively. Mean values are noted on the chart.

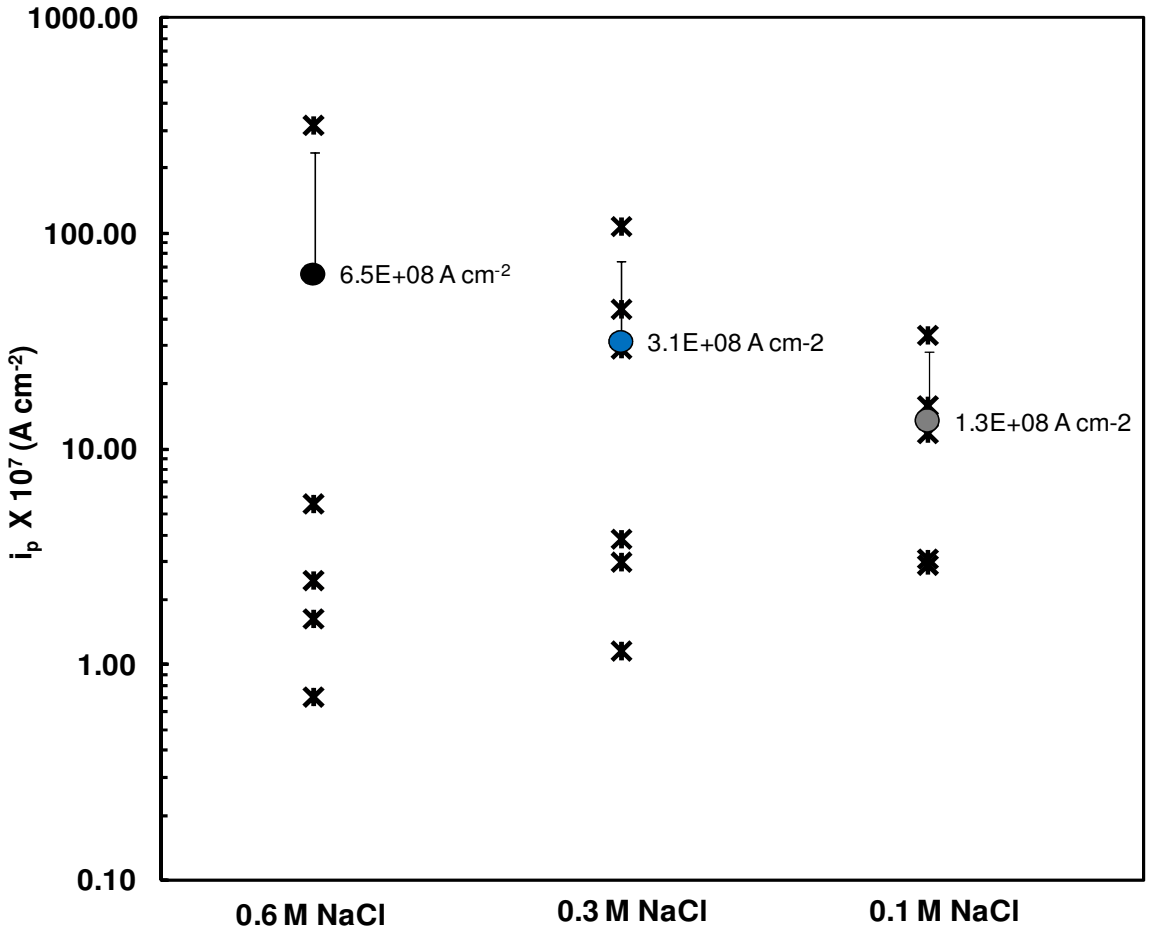

Figure 39. The passive current densities (i_p) of Vitreloy 105 as a function of chloride concentration. Circles and upper error bars represent mean values and upper 95% confidence intervals, respectively. Lower confidence intervals were omitted if they resulted in negative i_p values. Mean values are noted on the chart.

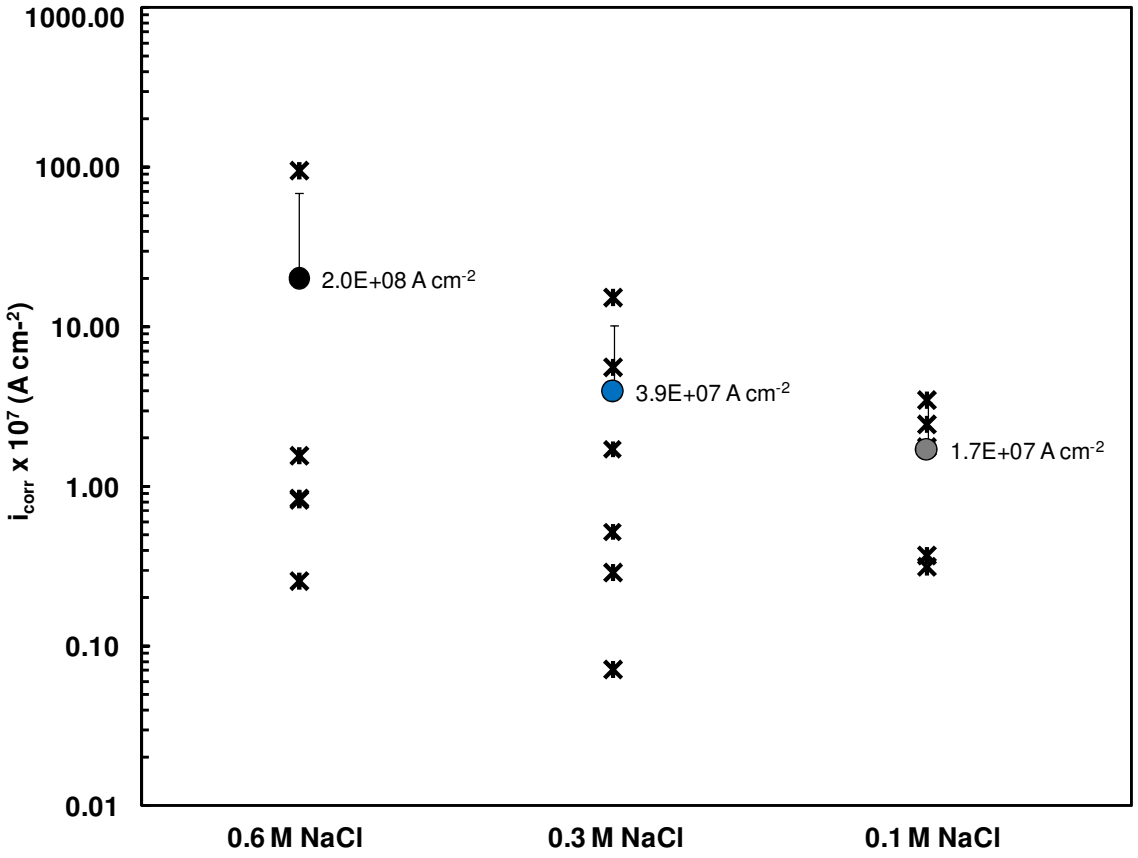

Figure 40. The corrosion current densities (i_{corr}) of Vitreloy 105 as a function of chloride concentration. Circles and upper error bars represent mean values and upper 95% confidence intervals, respectively. Lower confidence intervals were omitted if they resulted in negative i_{corr} values. Mean values are noted on the chart.

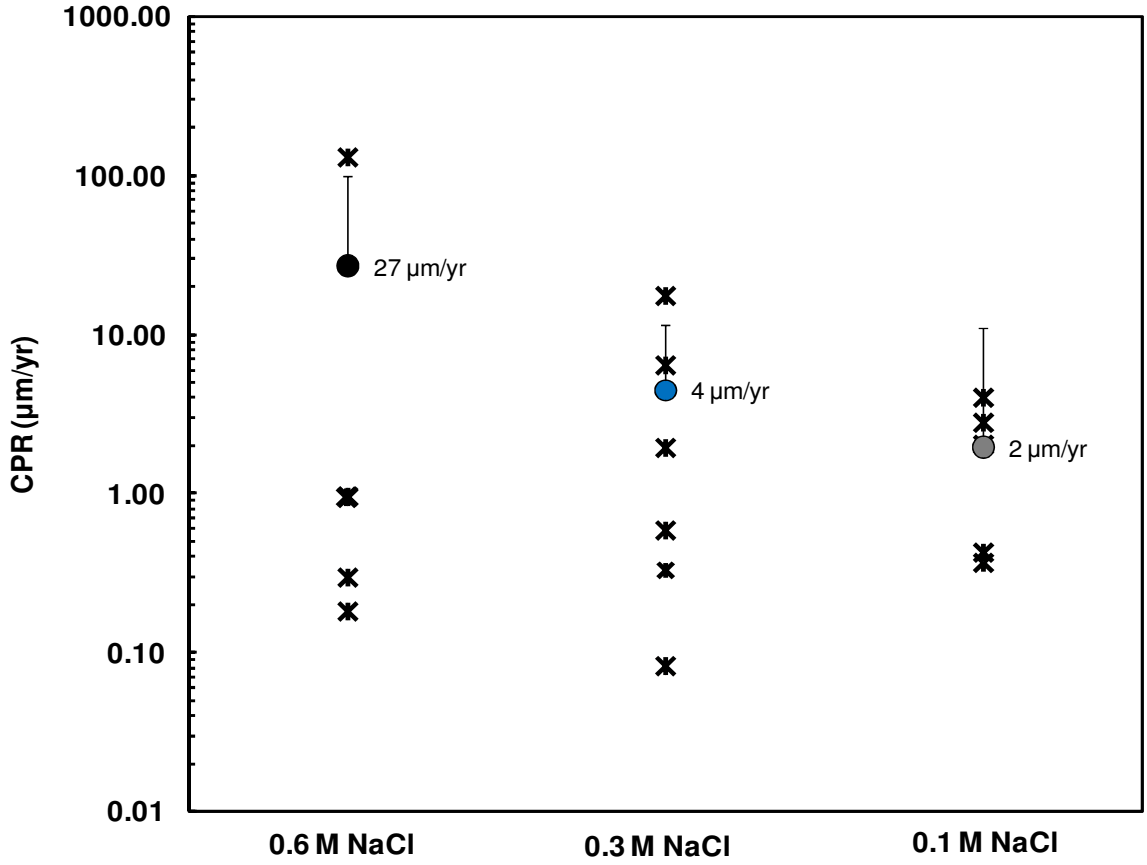

Figure 41. The corrosion penetration rates (CPR) of Vitreloy 105 as a function of chloride concentration. Circles and upper error bars represent mean values and upper 95% confidence intervals, respectively. Lower confidence intervals were omitted if they resulted in negative CPRs. Mean values are noted on the chart.

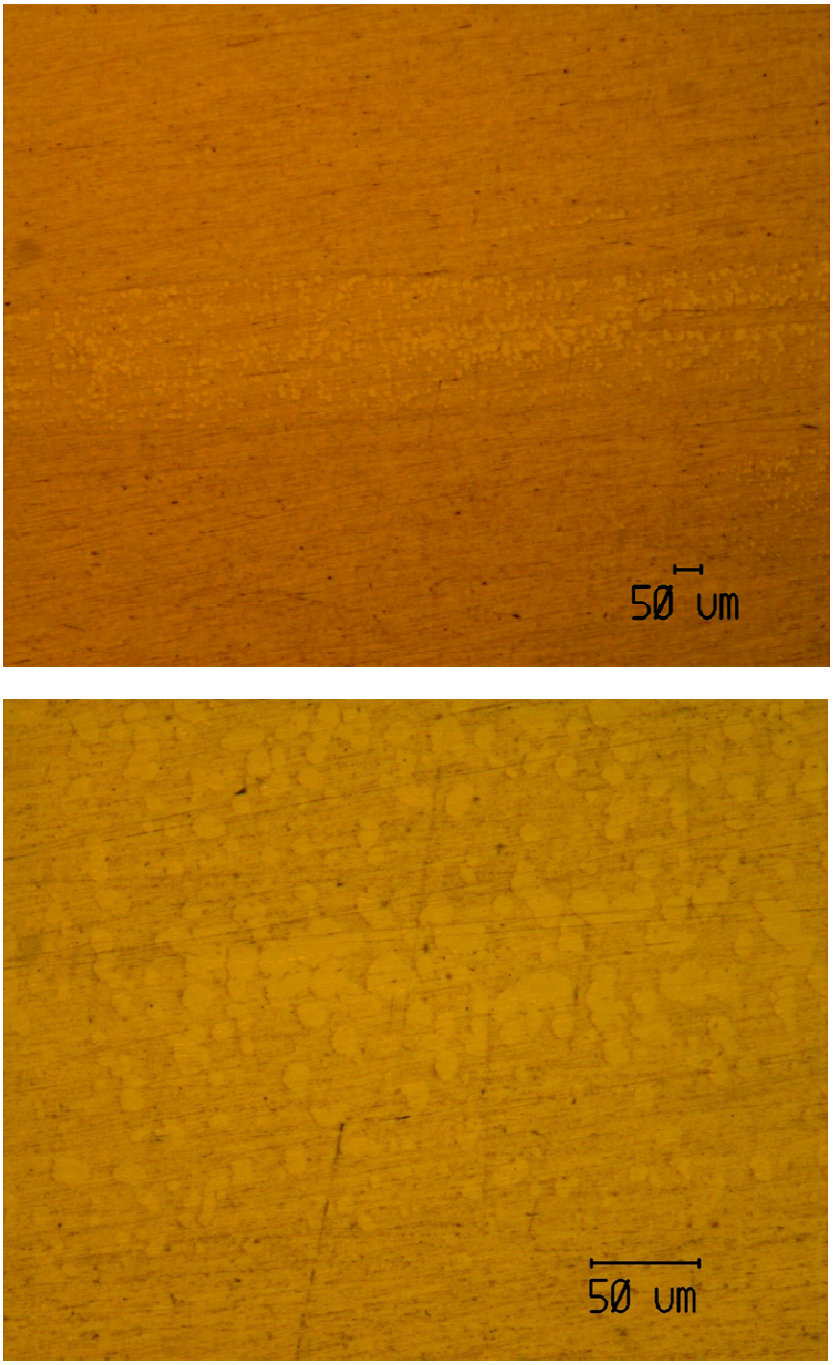

Figure 42. (top) Optical micrographs of “swirl” regions on the Vitreloy 105 BMG. (bottom) magnified image of the region.

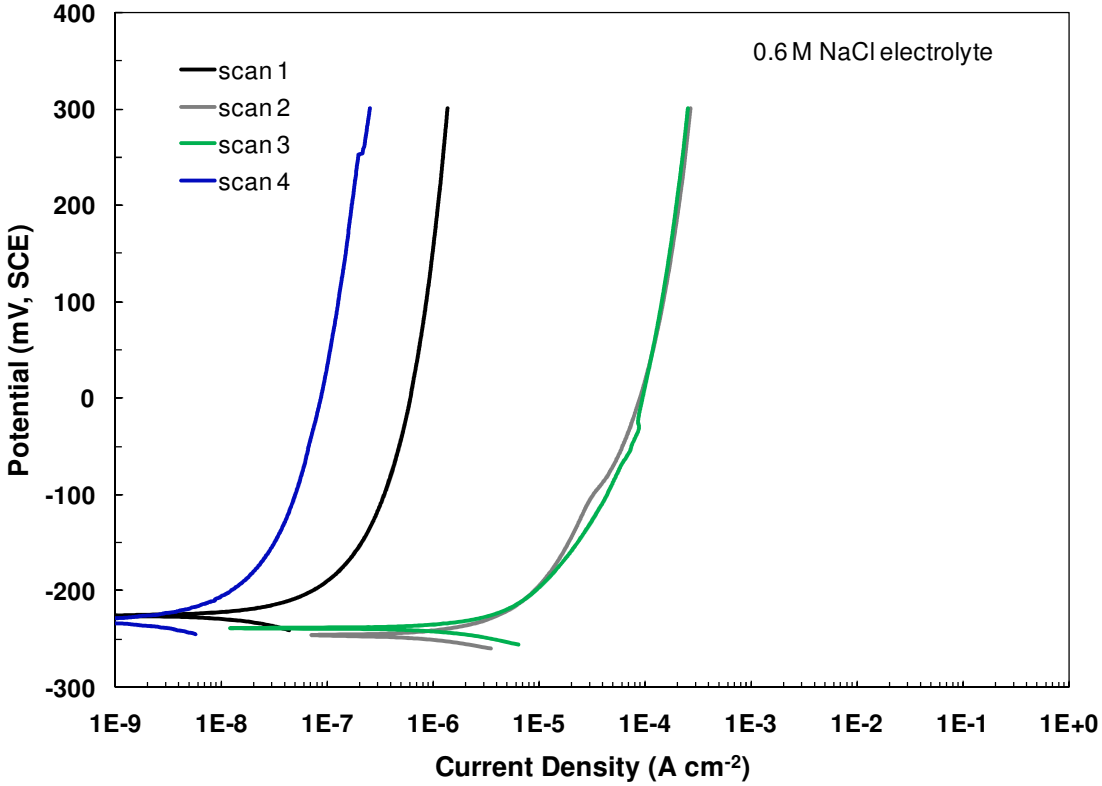

Figure 43. Polarization curves of Vitreloy 105 longitudinal samples. The sample polarized in scan 1 was laser treated.

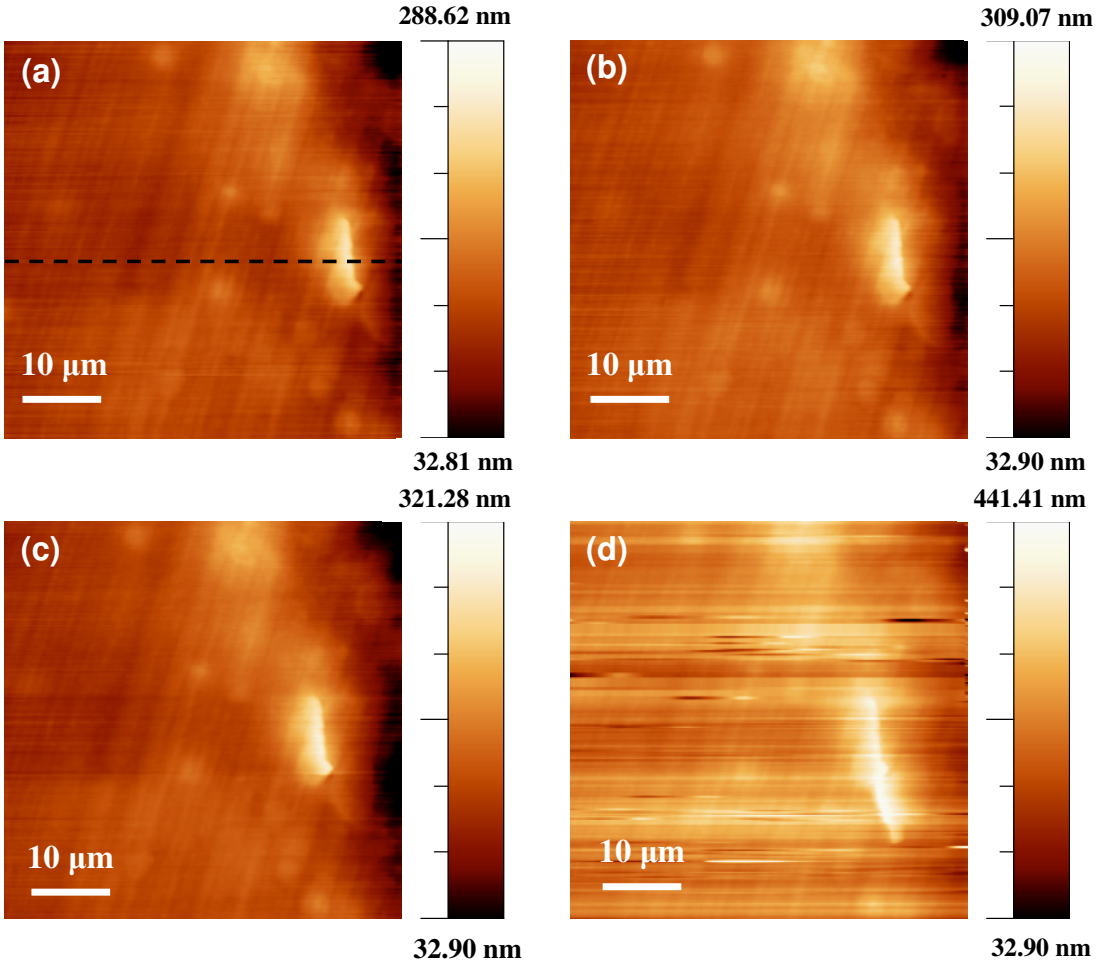

Figure 44. In-situ AFM topographic images of Vitreloy 105. Experiments were performed in a 0.6 M NaCl, and a potential of -190 mV, SCE was applied to the sample. Images (a), (b), (c), and (d) correspond to frames 1, 3, 5, and 7, respectively. The acquisition per frame was 10.7 minutes. Profiles of the four images were obtained at the position denoted by the dashed line in image (a).

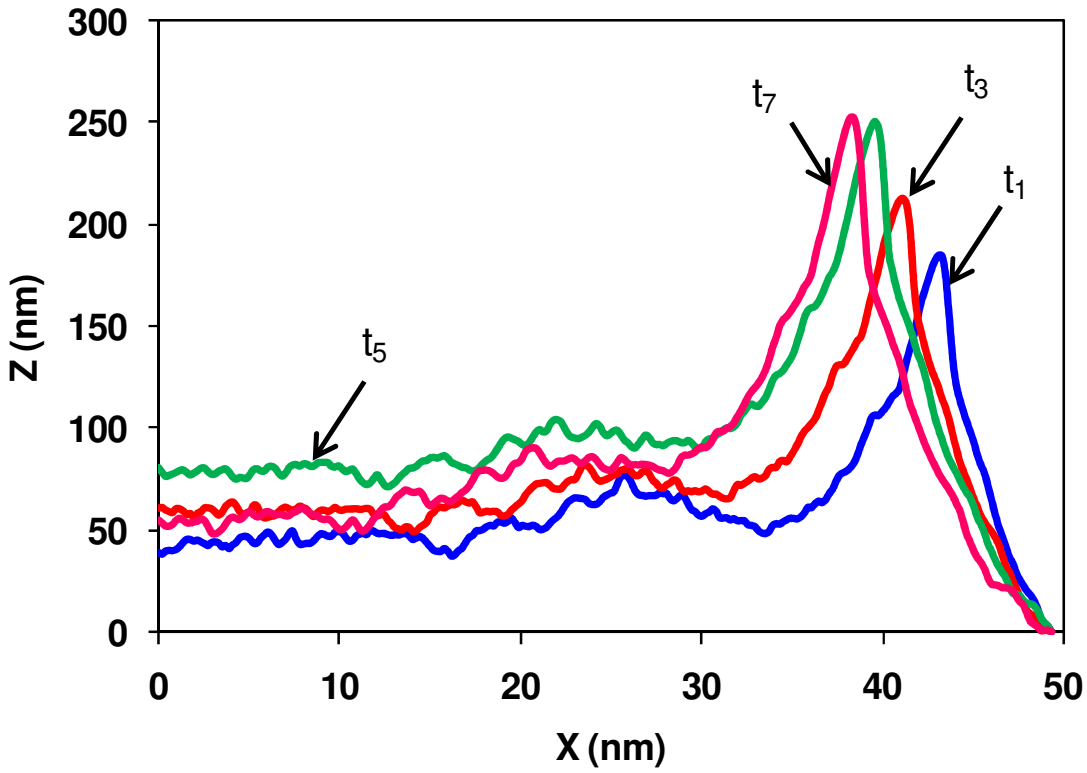

Figure 45. AFM topographic profiles along the dashed line shown in Figure 44 at various times during the potentiostatic experiment. The subscripts correspond to the frame number. The time that had elapsed between the profiles was approximately 21 minutes.

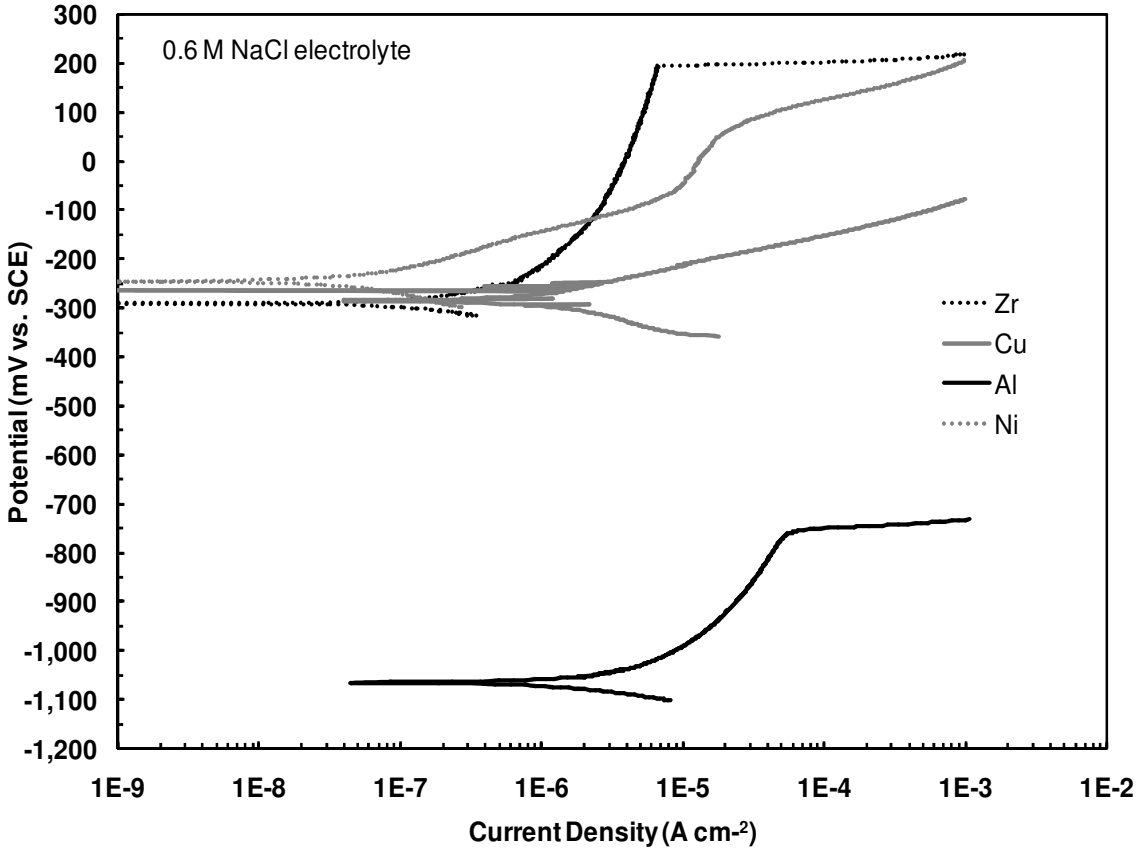

Figure 46. Representative polarization curves of crystalline Zr, Cu, Al, and Ni generated in 0.6 M NaCl electrolytes.

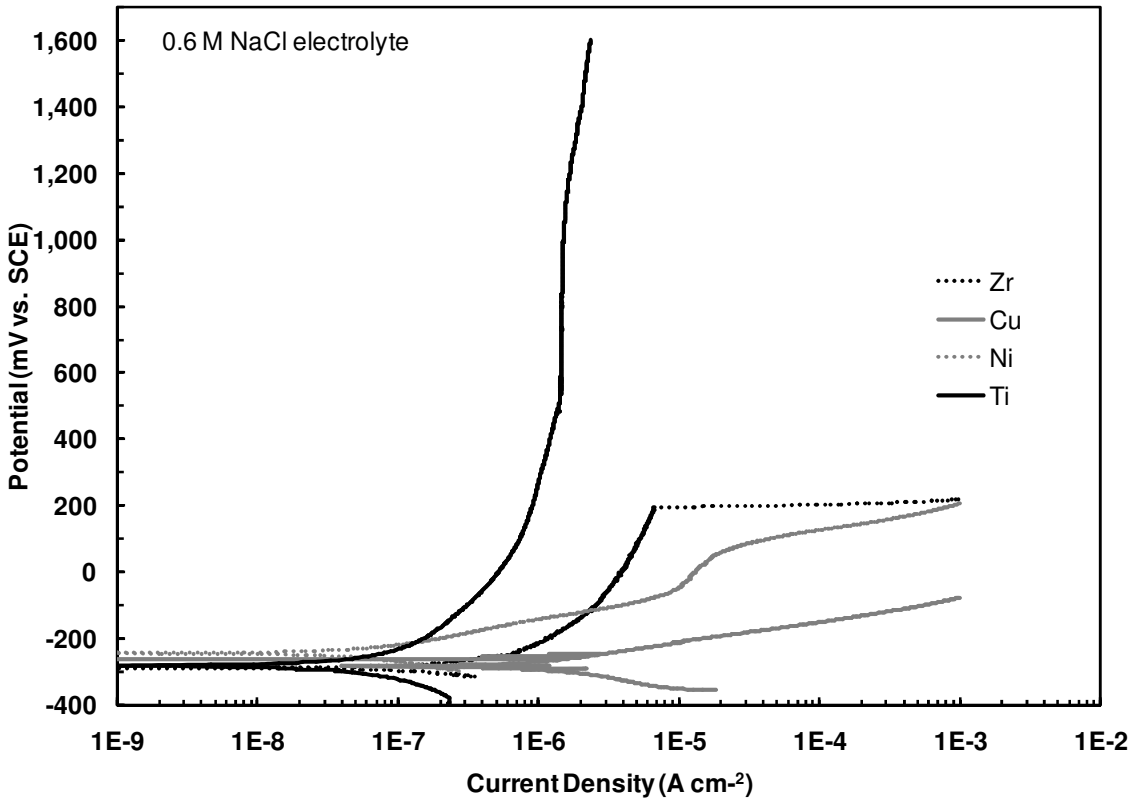

Figure 47. Representative polarization curves of Zr, Cu, Ni, and Ti from experiments performed in 0.6 M NaCl.

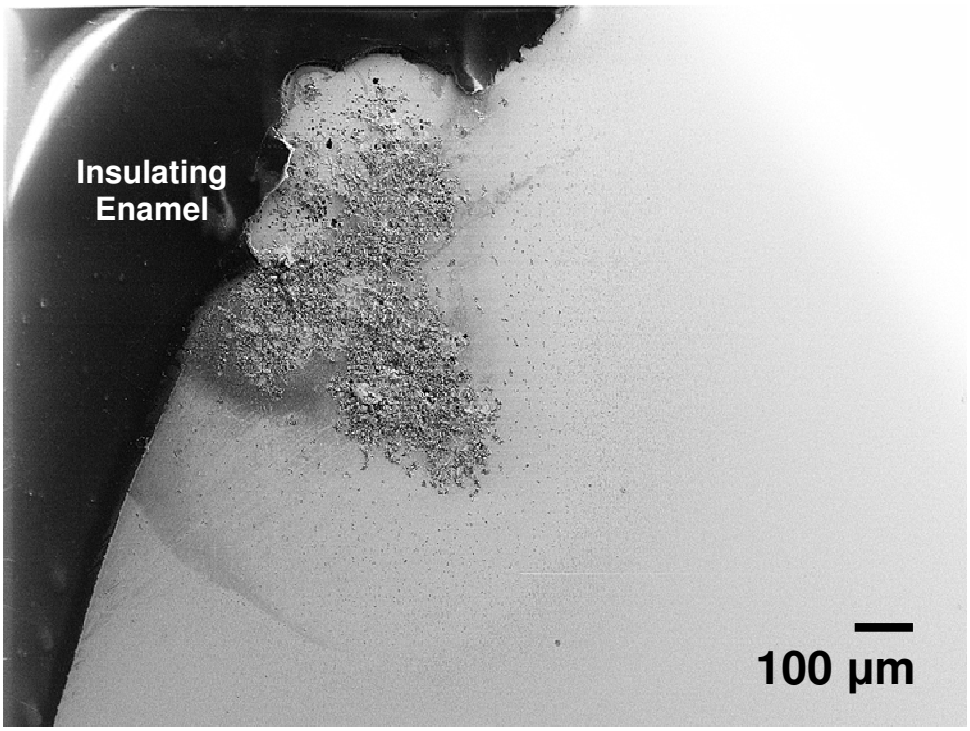

Figure 48. SEM micrograph of a corroded region at the insulating enamel/sample interface $Zr_{50}Cu_{40}Al_{10}$ sample formed at E_{corr} (i.e., not anodically polarized) in a 0.6 M NaCl electrolyte.

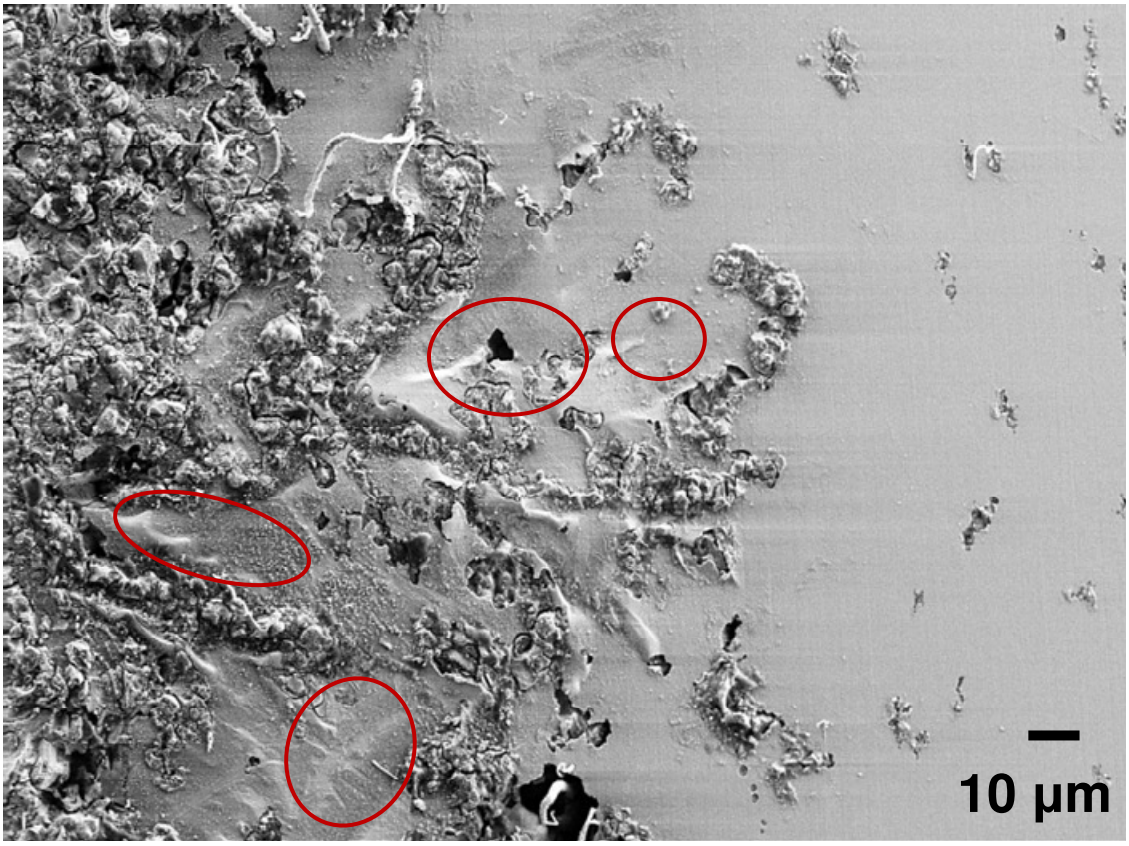

Figure 49. SEM photomicrograph of the surface $Zr_{50}Cu_{40}Al_{10}$ illustrating the corrosion that occurs at E_{corr} (i.e., not anodically polarized) in a 0.6 M NaCl electrolyte. The area is of an area of the corroded region shown in Figure 48. The red circles highlight dendrites.

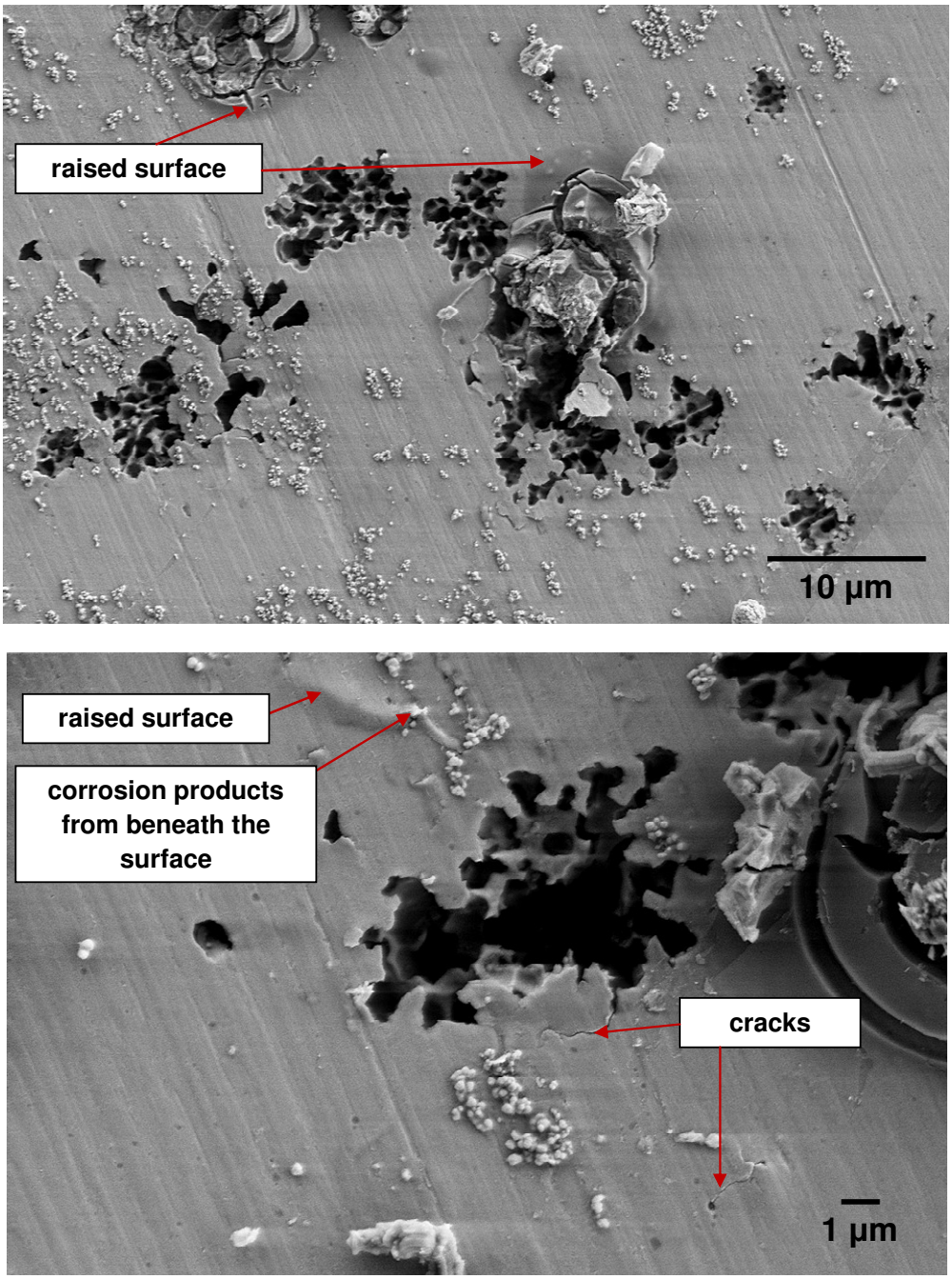

Figure 50. (a) SEM micrograph of $Zr_{50}Cu_{40}Al_{10}$ after a polarization experiment in a 0.1 M NaCl electrolyte illustrating the irregular shape of pits on the surface. (b) Magnified corrosion pit.

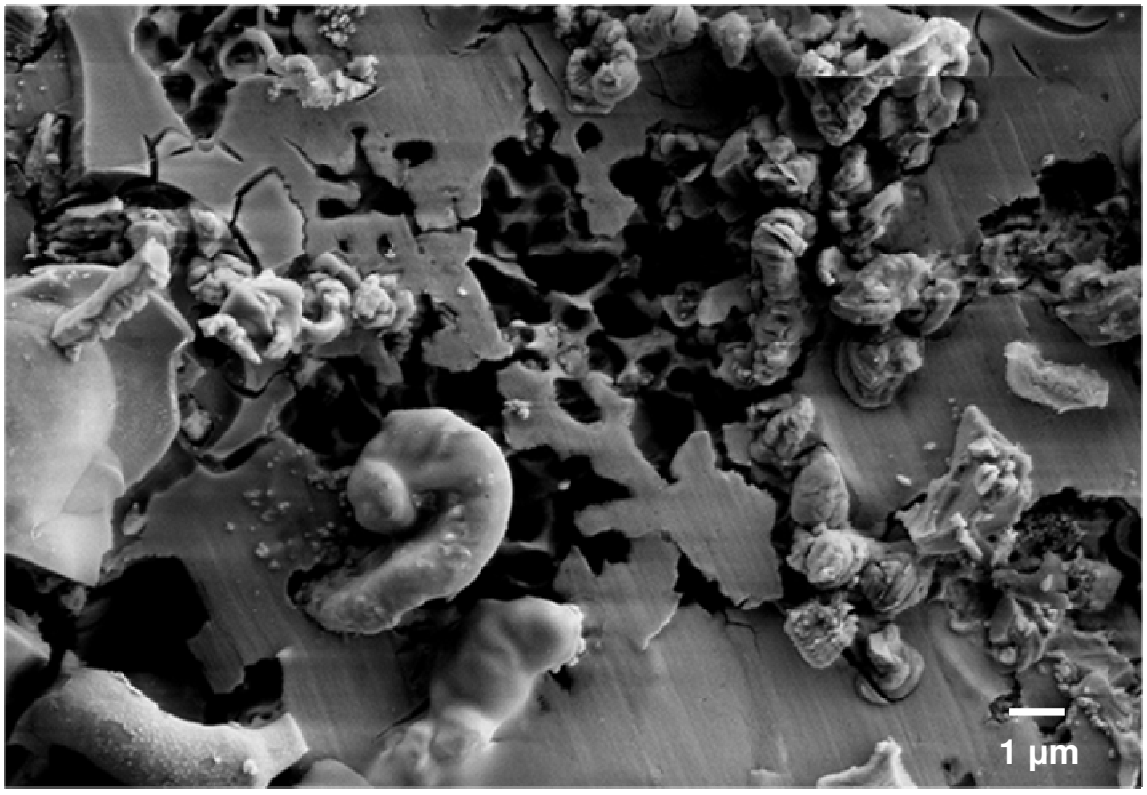

Figure 51. SEM micrograph of $Zr_{50}Cu_{40}Al_{10}$ after a polarization experiment in a 0.1 M NaCl electrolyte illustrating the cracks due to exfoliation corrosion.

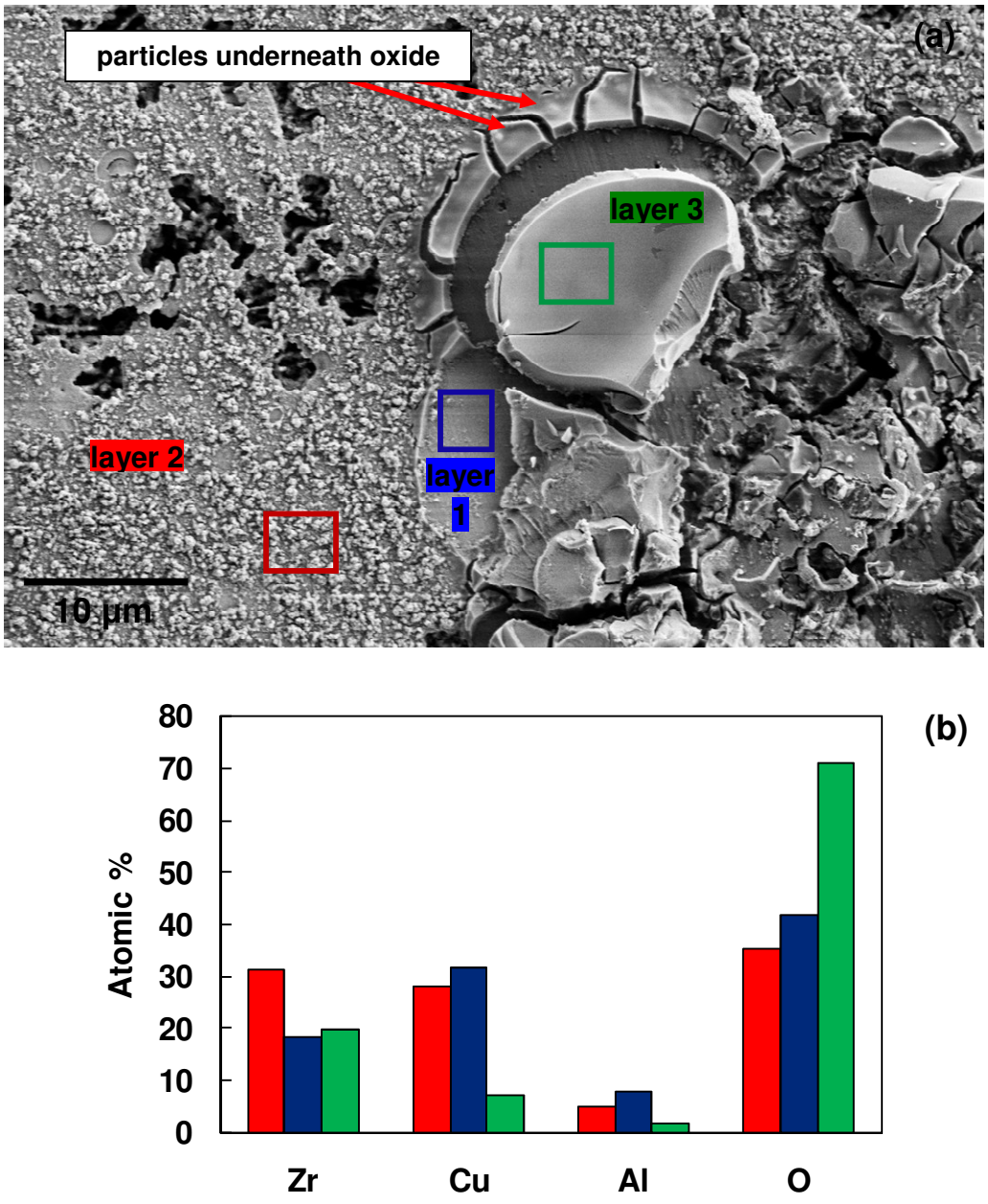

Figure 52. (a) SEM micrograph of $Zr_{50}Cu_{40}Al_{10}$ after a polarization experiment in a 0.1 M NaCl electrolyte showing an area of the surface covered with corrosion products. (b) EDS analysis of the regions of the surface denoted in (a).

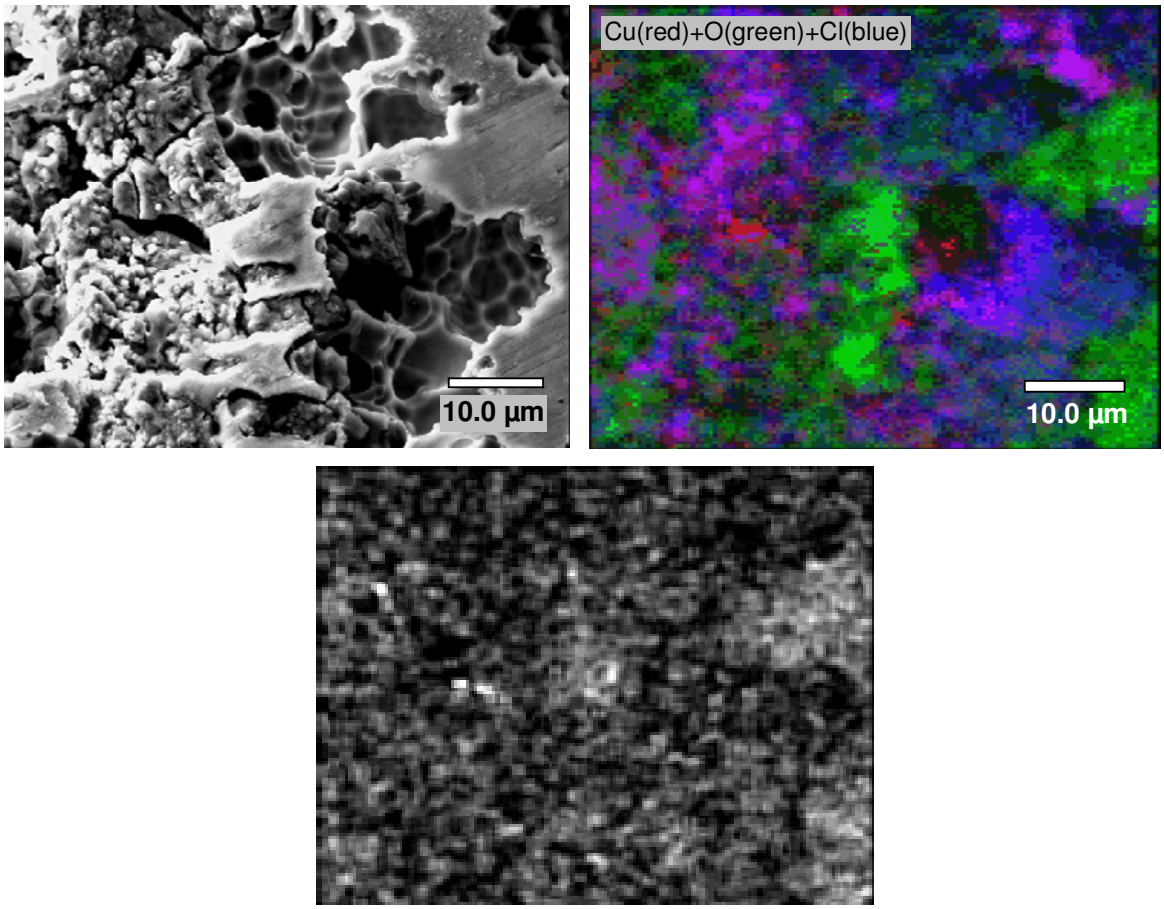

Figure 53. (top left) SEM micrograph image of pits on the surface of a $Zr_{50}Cu_{40}Al_{10}$ sample after polarization in a 0.6 M NaCl electrolyte to 300 mV, SCE. (top right) Color-combined Auger map of Cu (red), Cl (blue), and O (green) corresponding to the area shown in the micrograph. (bottom) Gray-scale Auger map of Zr (white) present in the aforementioned area.

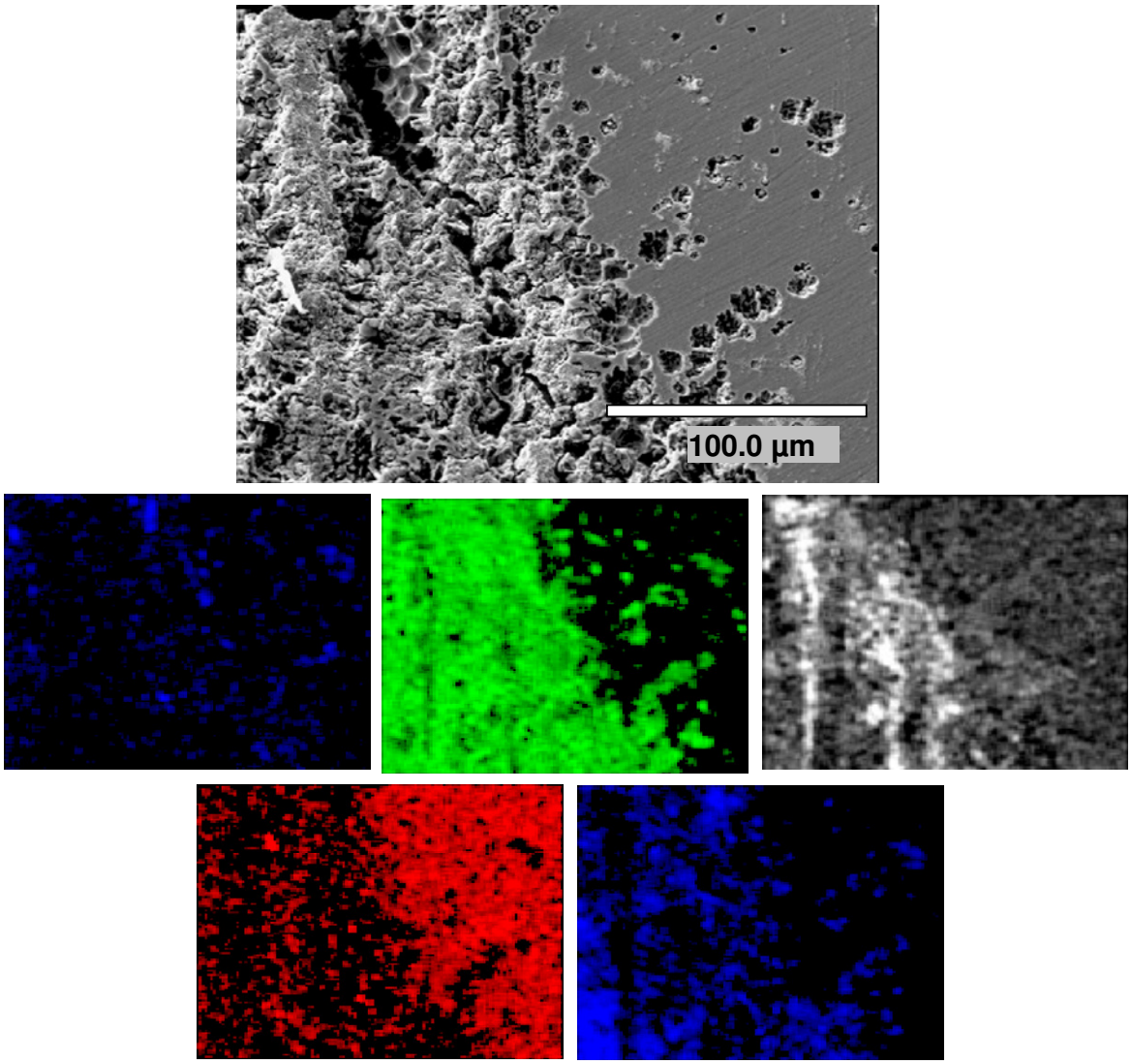

Figure 54. (row 1) Scanning electron image of a heavily corroded portion of the polarized $Zr_{50}Cu_{40}Al_{10}$ sample. (row 2, left to right) Auger maps of C; O; Cu; (row 3, left to right) Zr; and Cl after sputter etching.

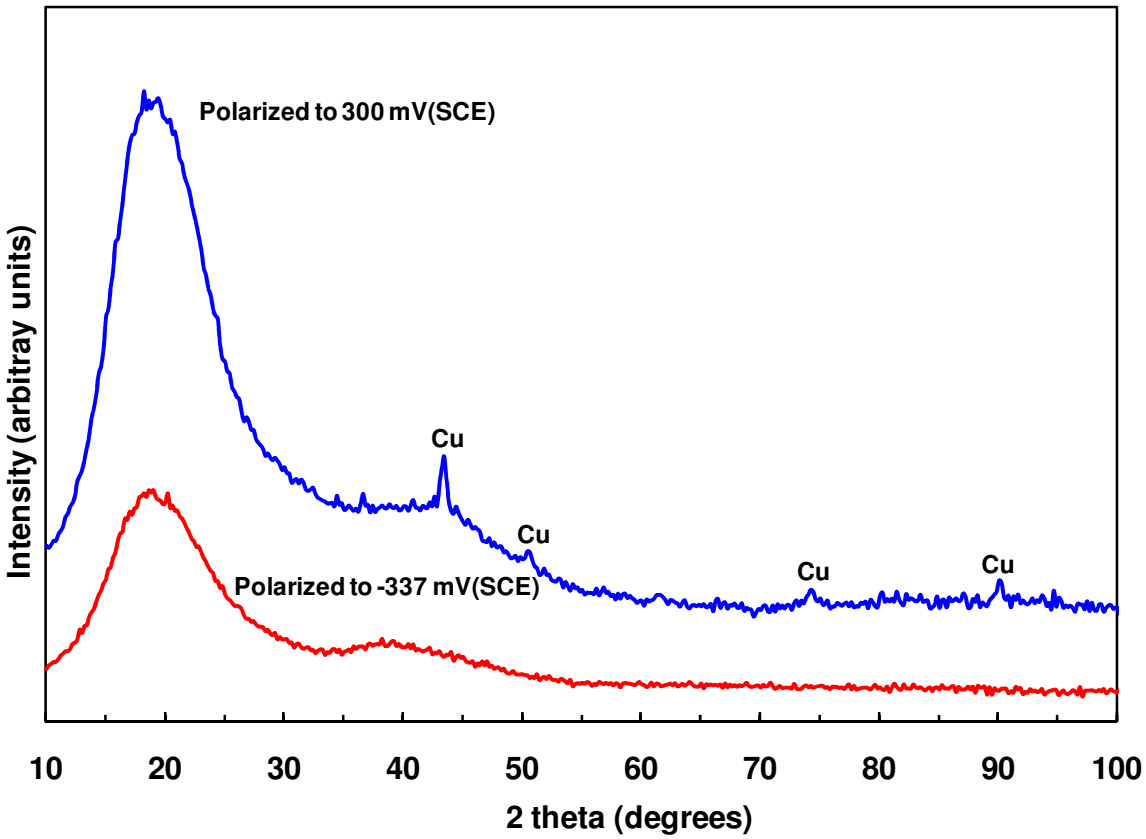

Figure 55. XRD patterns of $Zr_{50}Cu_{40}Al_{10}$ after two different polarization treatments. One sample was anodically polarized to -337 mV, SCE in a 0.1 M NaCl electrolyte. The other sample was polarized to 300 mV, SCE in a 0.6 M NaCl electrolyte.

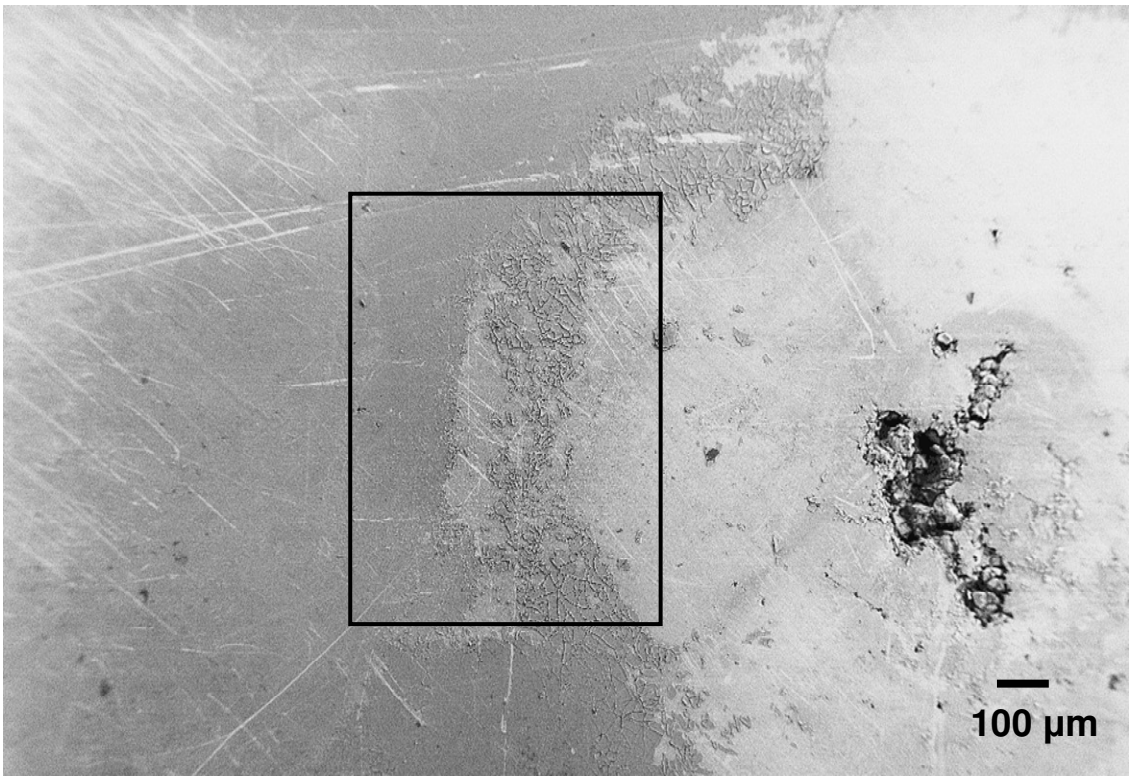

Figure 56. SEM photomicrograph of the corrosion experienced by $Zr_{50}Cu_{33}Al_{10}Pd_7$ while at open-circuit conditions in a 0.3 M NaCl electrolyte.

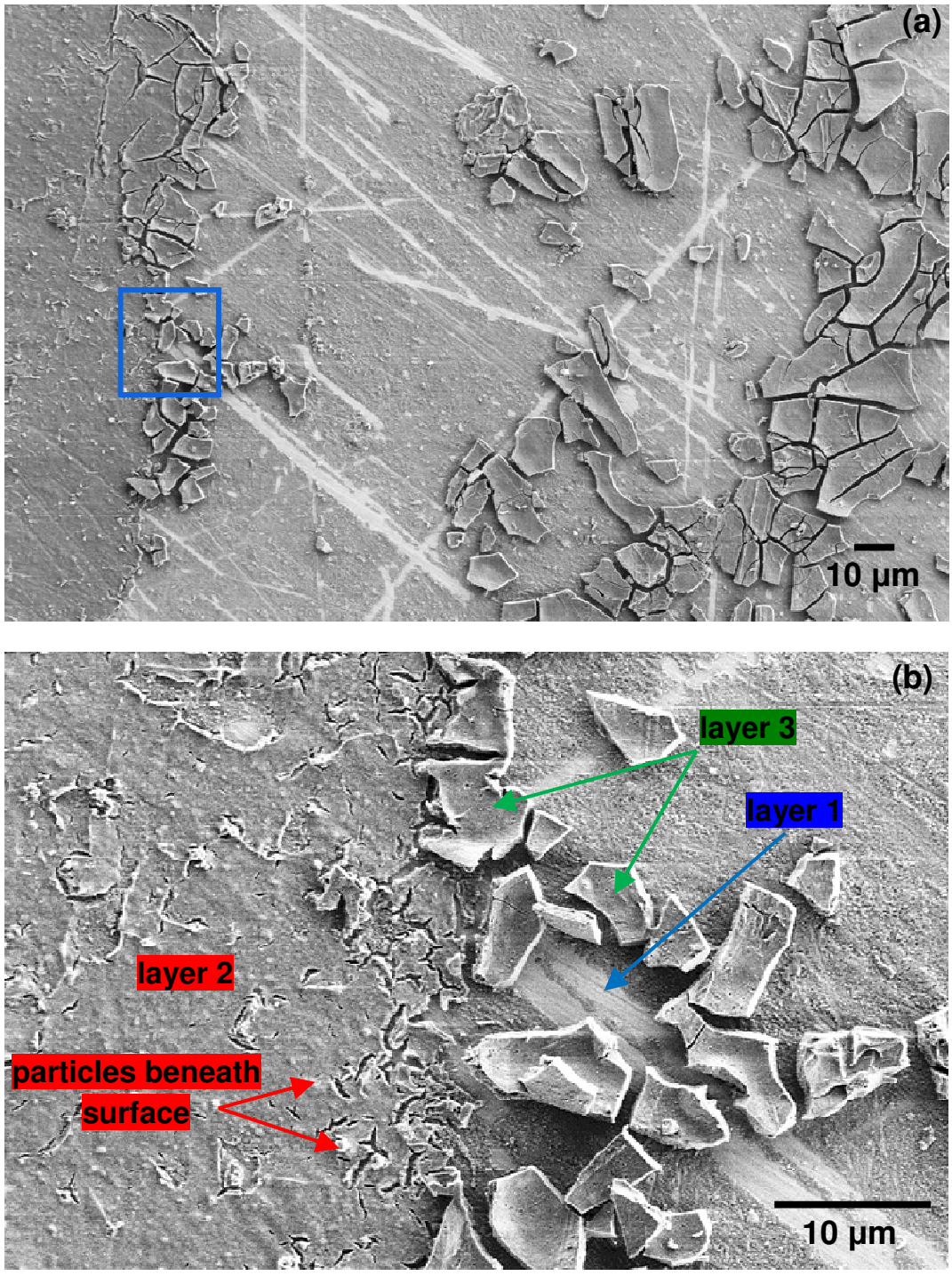

Figure 57. (a) SEM photomicrograph of the area enclosed in the rectangle shown in Figure 56. (b) Magnified; image of area shown in blue rectangle in (a).

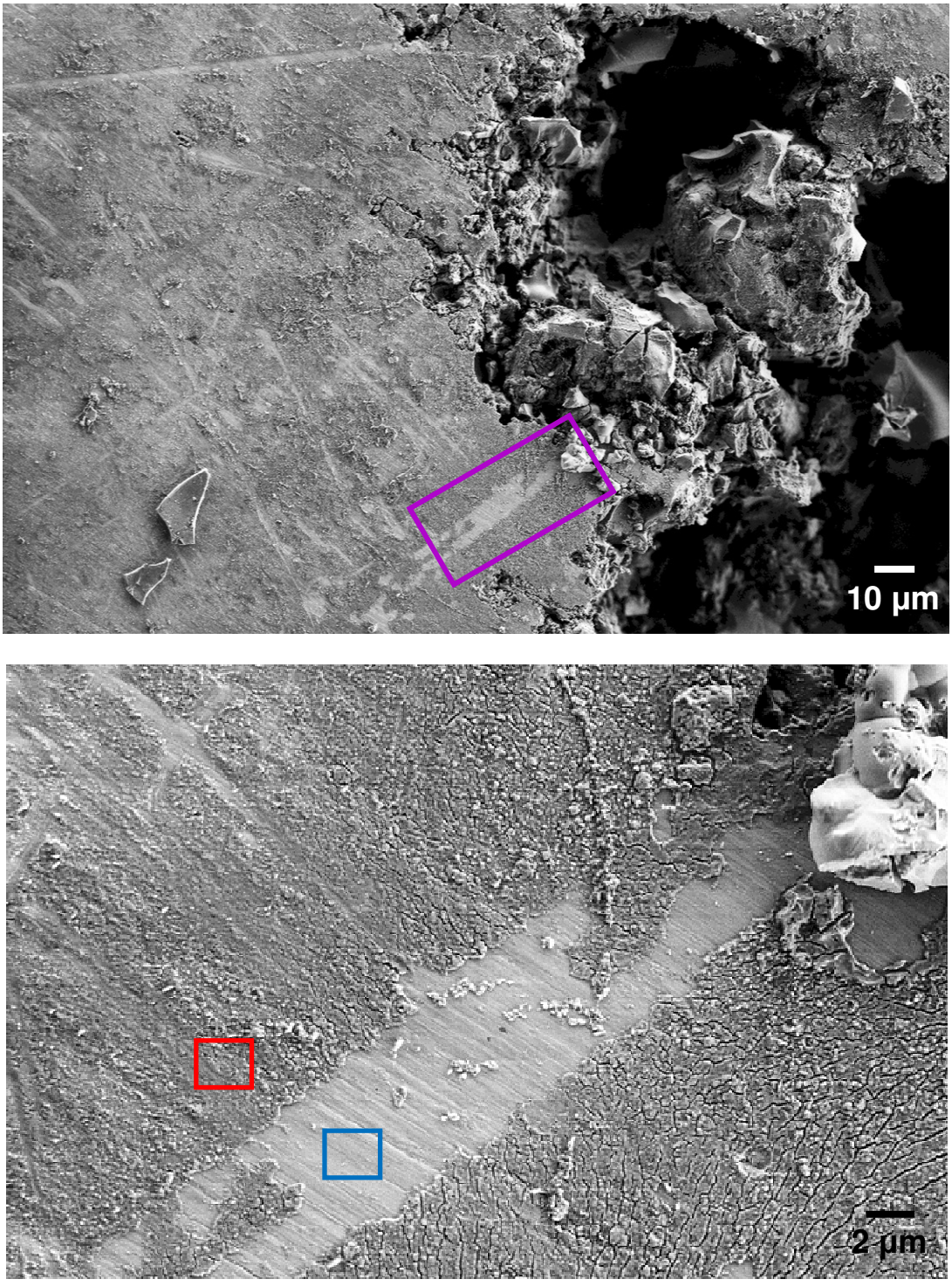

Figure 58. (a) Heavily corroded area on the surface of $Zr_{50}Cu_{33}Al_{10}Pd_7$. (b) Magnified image of the area enclosed by the purple rectangle.

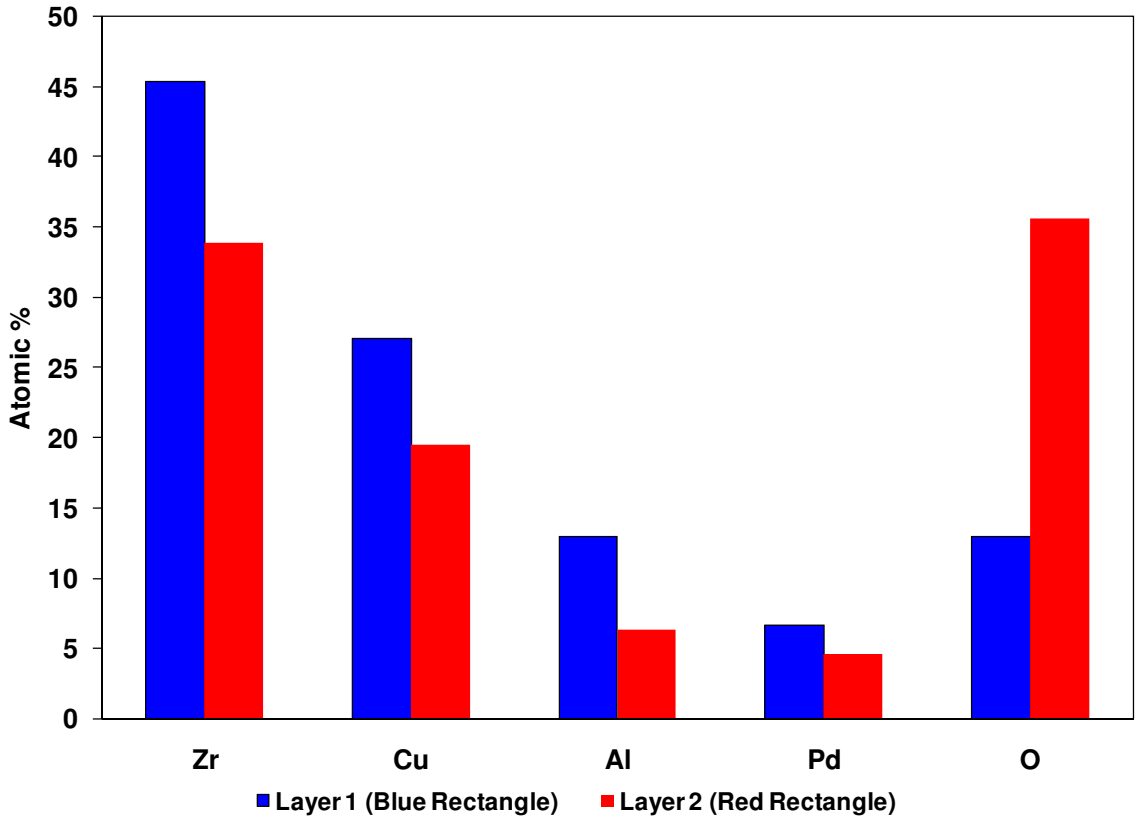

Figure 59. EDS analyses of the surface of $Zr_{50}Cu_{33}Al_{10}Pd_7$ corresponding to the areas shown in Figure 58b.

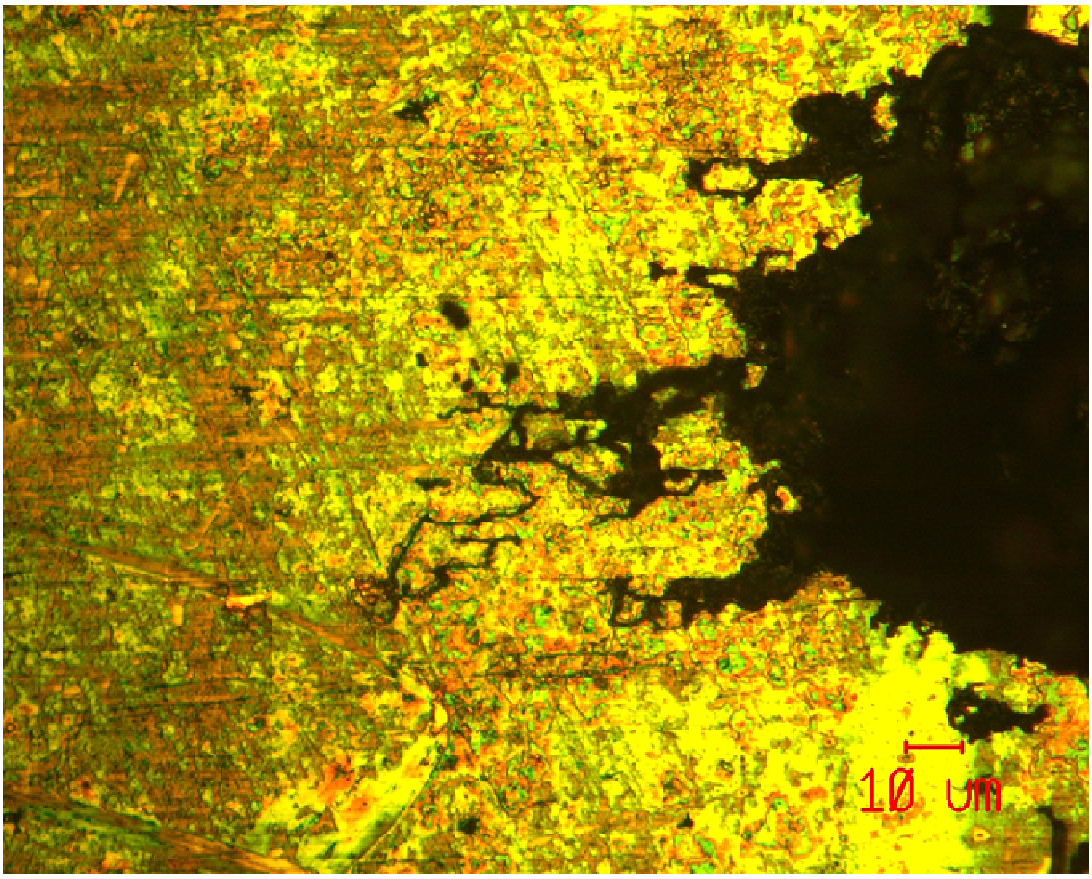

Figure 60. Optical micrograph of the region shown in the top image of Figure 45 illustrating the characteristic channels associated with chloride induced corrosion.

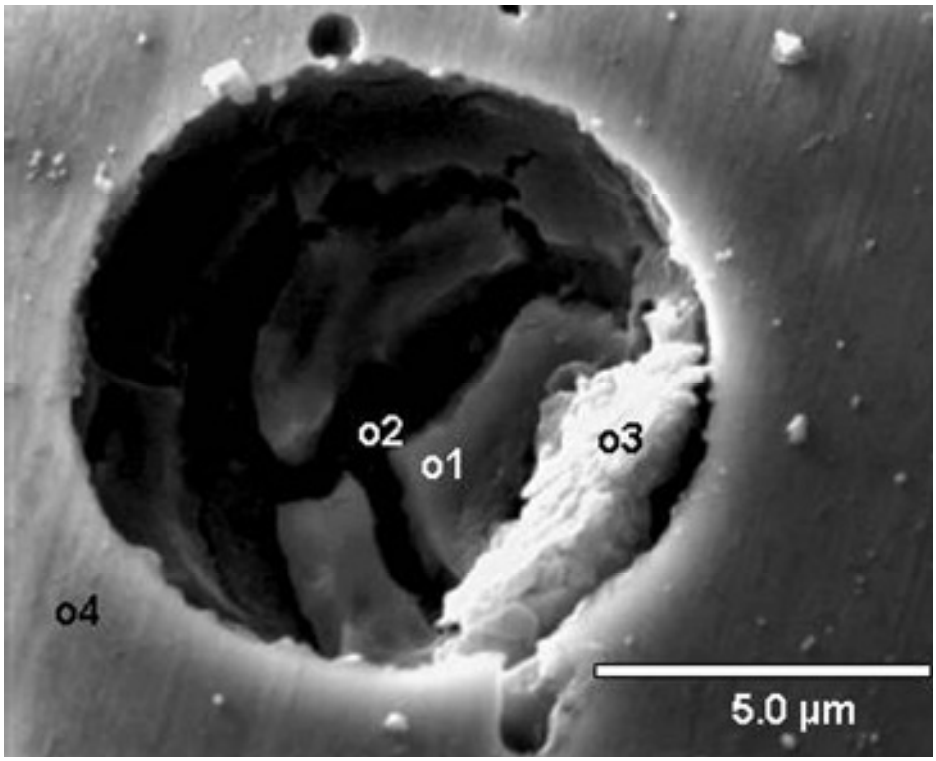

Figure 61. SEM micrograph of a pit on the surface of $Zr_{50}Cu_{33}Al_{10}Pd_7$ after aborting a polarization experiment in 0.6 M NaCl. Numbered positions correspond to points where survey spectra were attained (see Table 4).

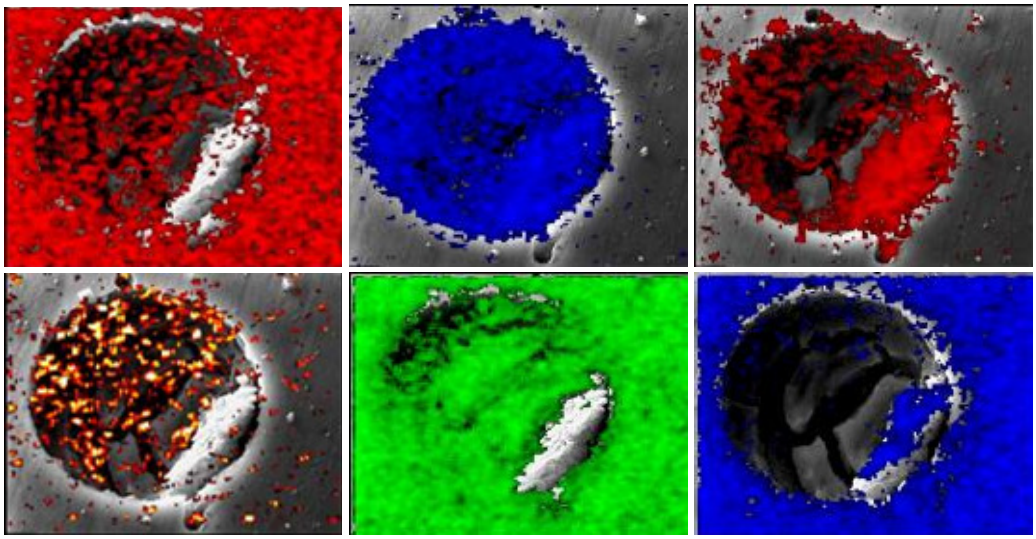

Figure 62. Auger maps obtained prior to sputtering of (top, left to right) Zr, Cl, Cu, (bottom, left to right) Pd, O, and C. Each of the maps is superimposed on the image shown in Figure 61.

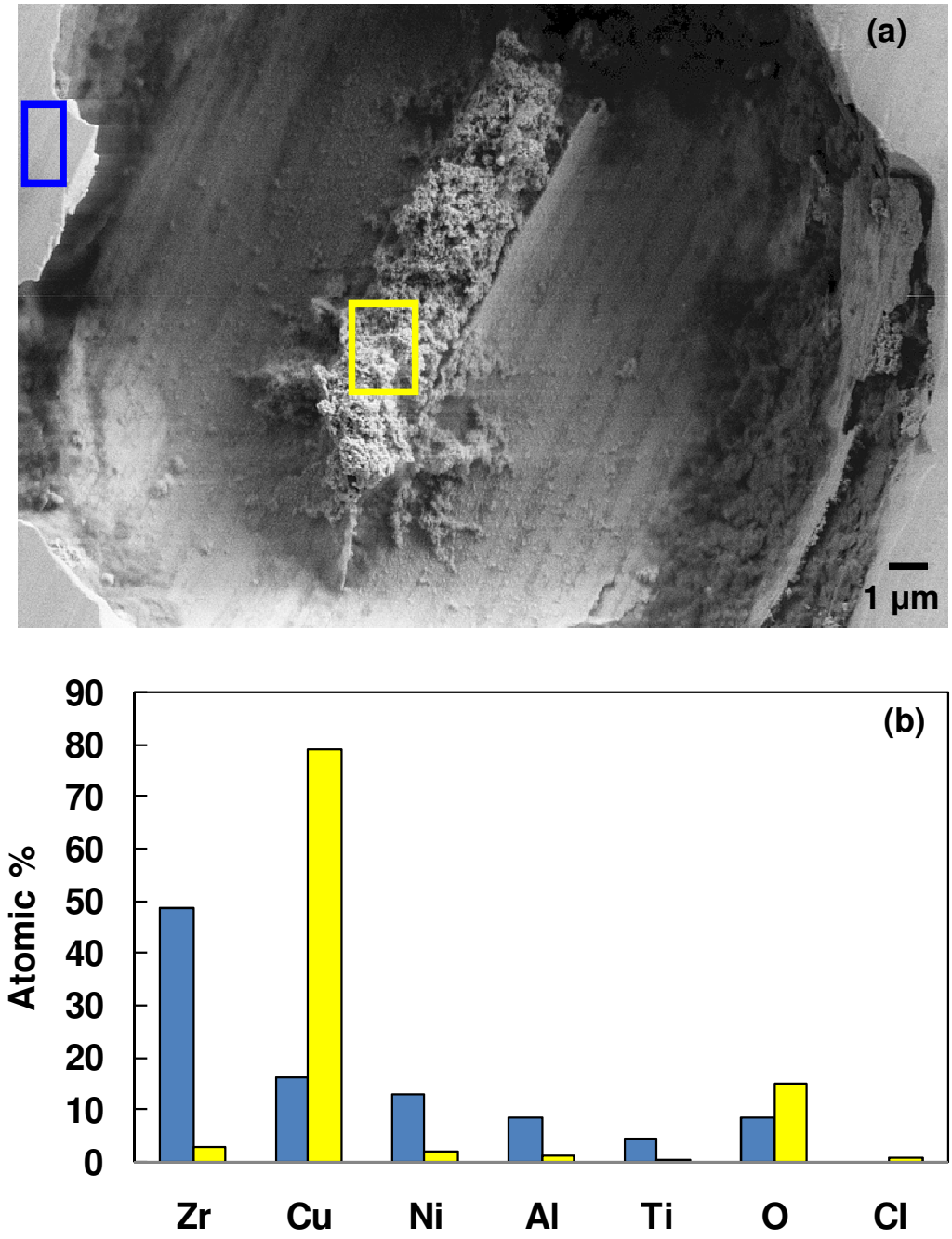

Figure 63. (a) SEM photomicrograph of a pit on Vitreloy 105 after polarization to E_{pit} (mV, SCE). (b) EDS was performed on areas outlined by the blue and yellow rectangles marked on image (a).

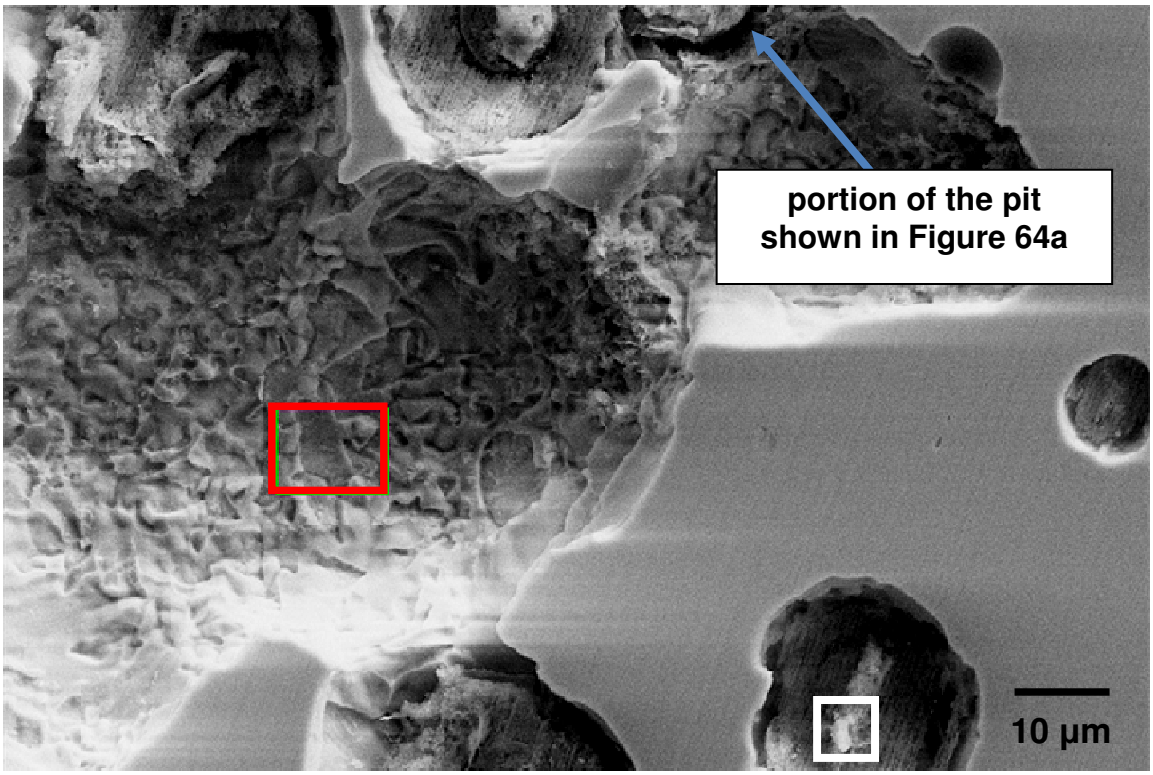

Figure 64. SEM micrograph of a cluster of pits on the surface of Vitreloy 105 after being polarized to E_{pit}. The bottom portion of the pit shown in Figure 63a is denoted. EDS analyses were performed on the areas within the red and white rectangles.

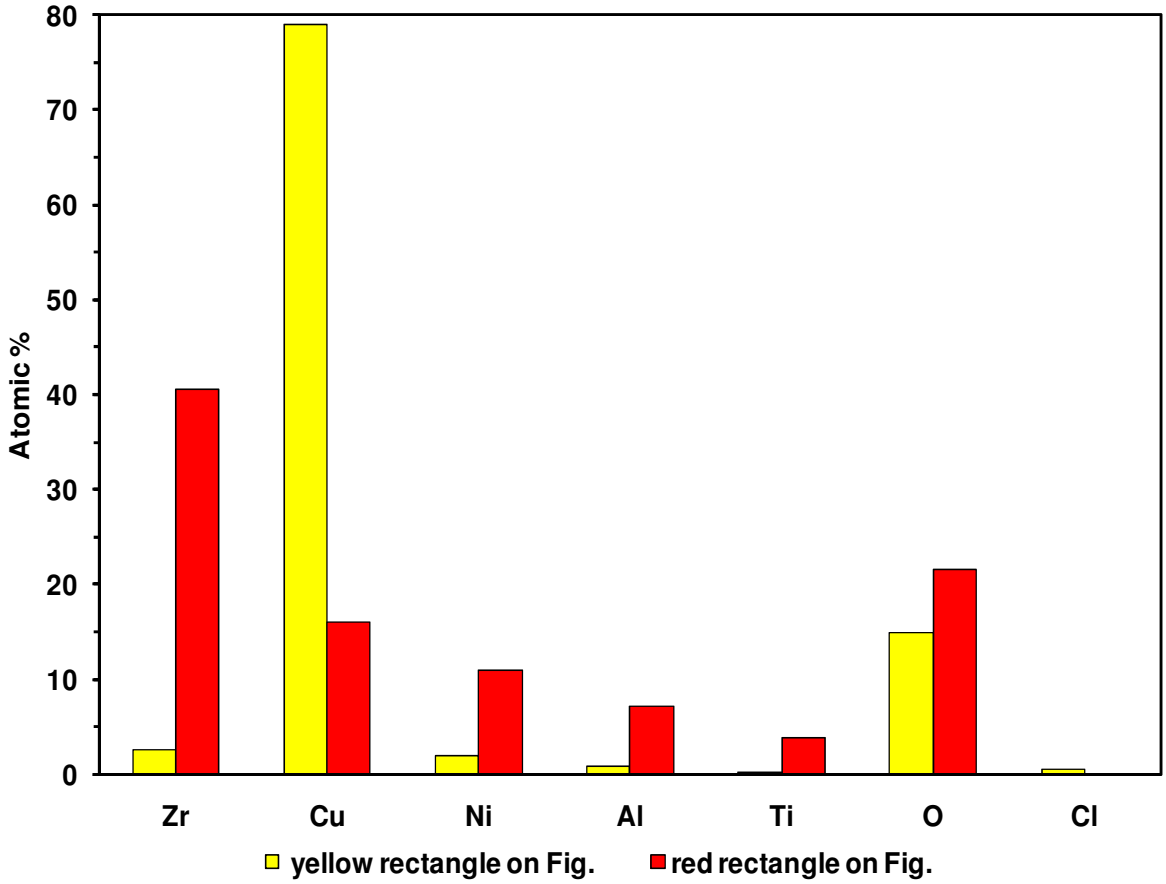

Figure 65. EDS analyses of the area within the yellow rectangle on Figure 63a and the area within the red rectangle in Figure 64.

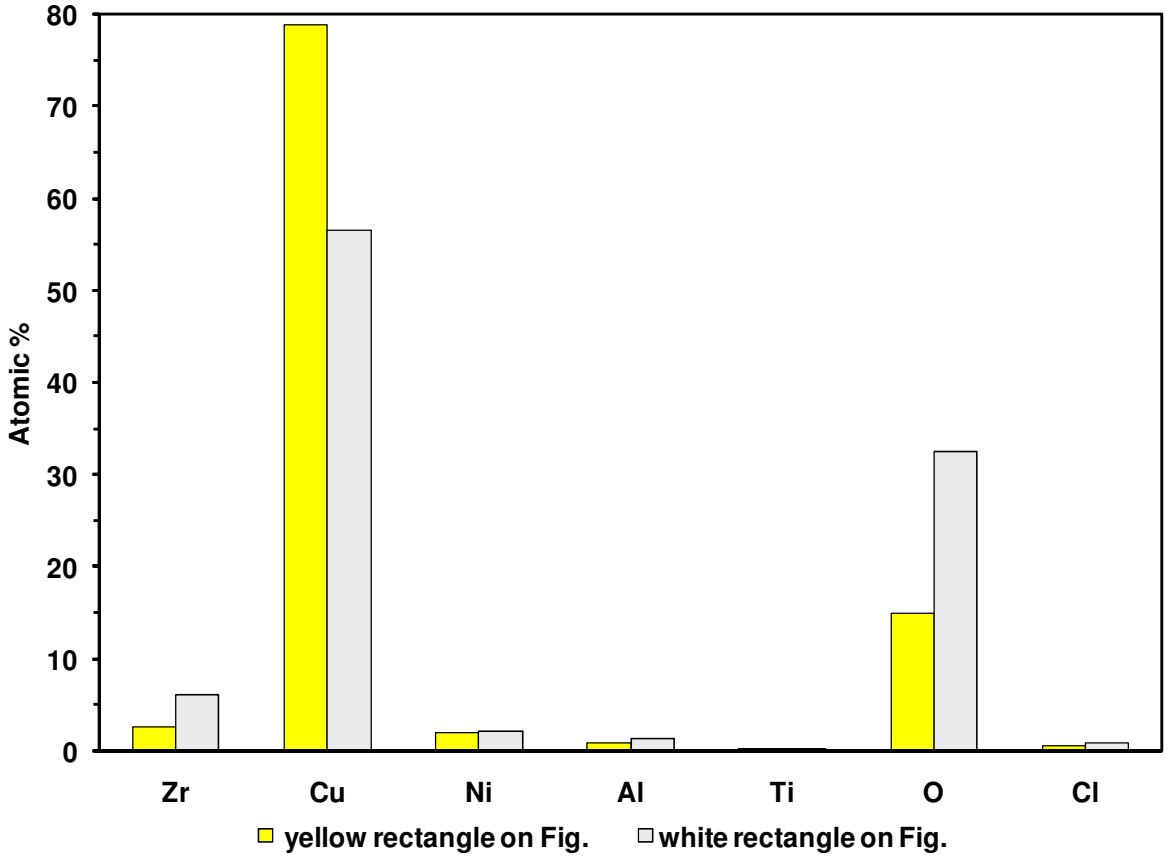

Figure 66. EDS results of the area within the yellow rectangle on Figure 63a and the area within the white rectangle shown in Figure 64.

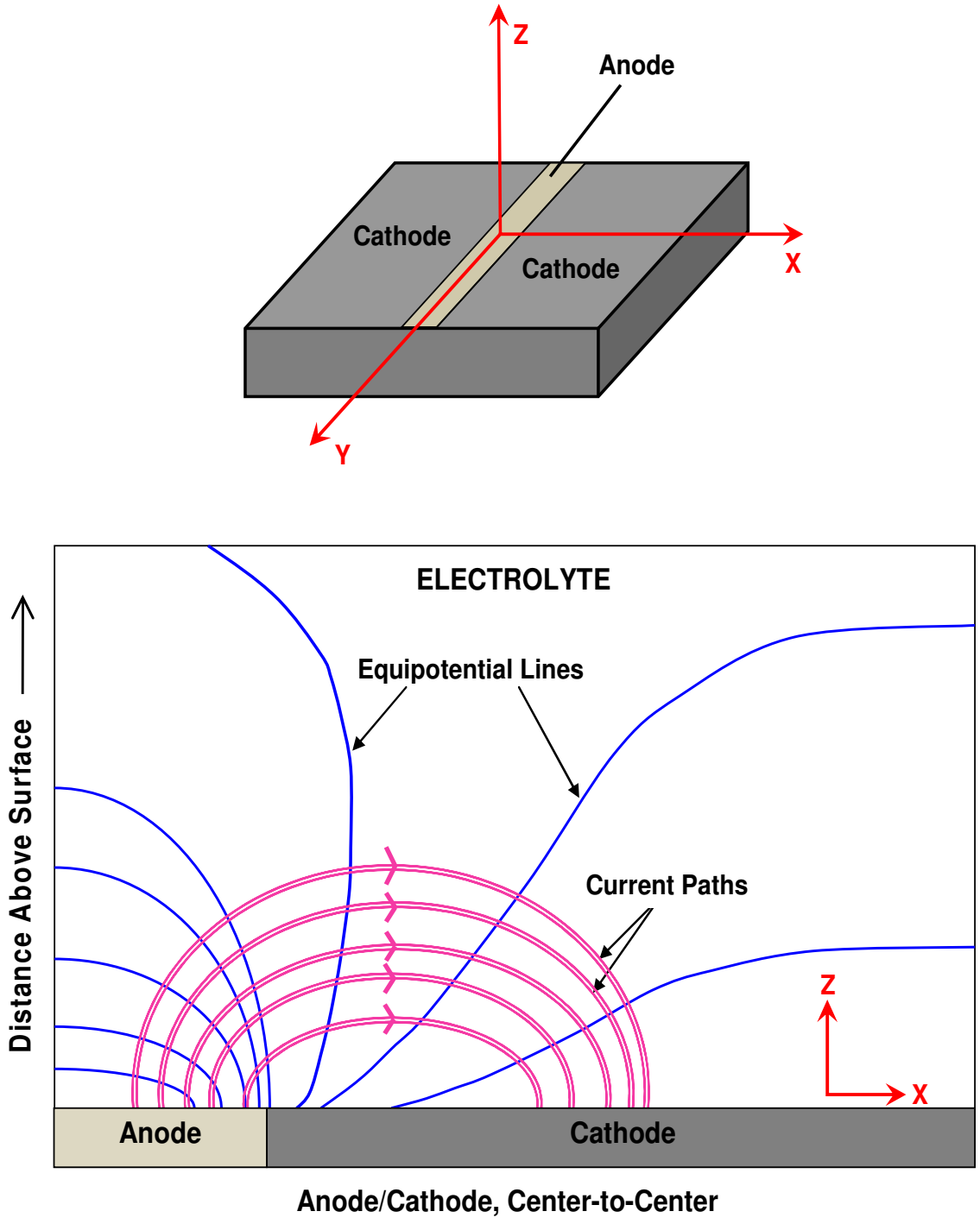

Figure 67. (a) An anodic site between two cathodic sites on a metal surface. (b) A schematic illustrating the current path from the anode to the cathode and the potential gradient within the electrolyte. Adapted from Stansbury and Buchanan [108]

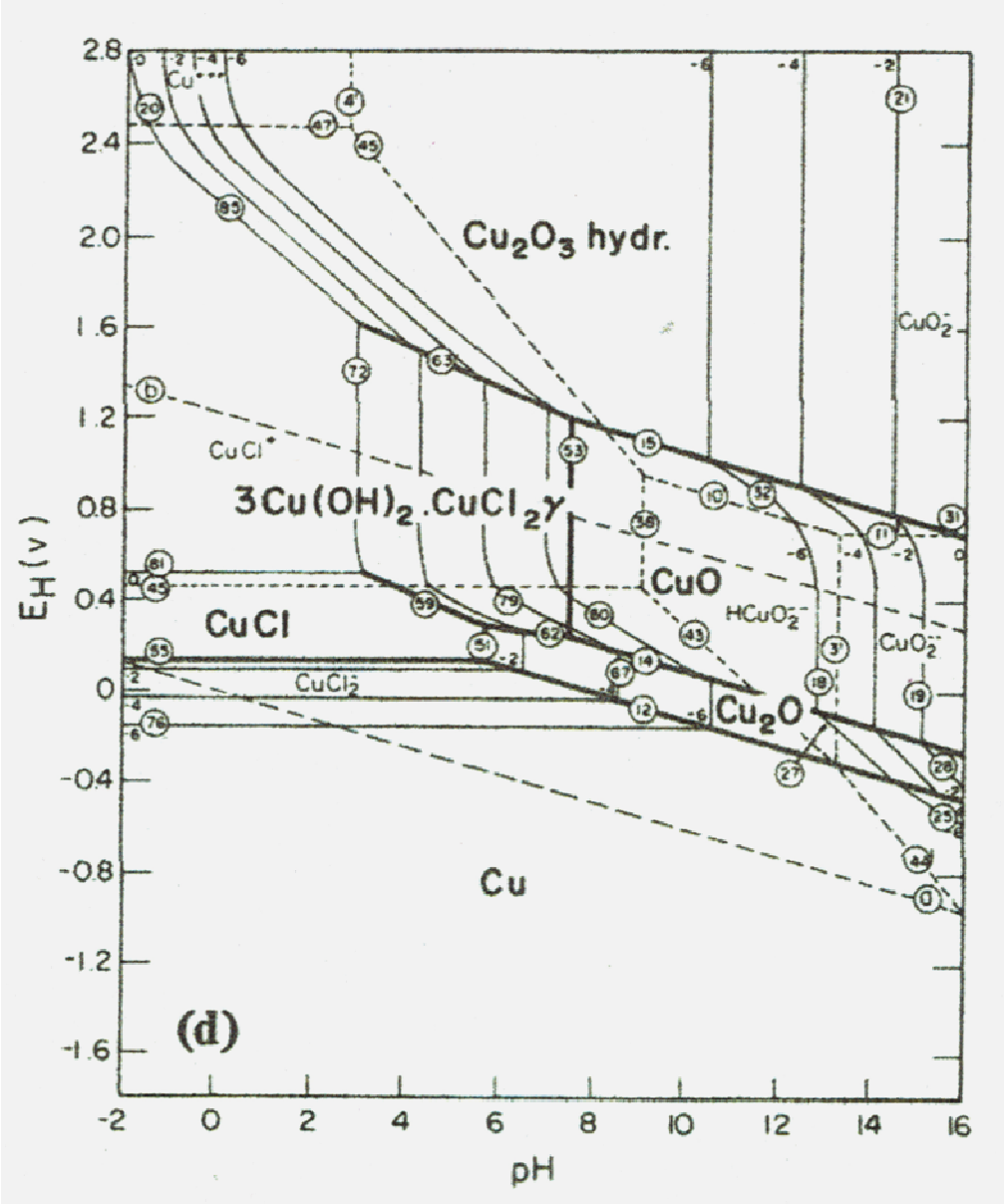

Figure 68. Potential-pH equilibrium diagram for Cu-Cl-H_2O at 25°C and a Cl^- concentration of 35,500 ppm [127].[10] The potential is relative to the hydrogen reference electrode; the standard calomel electrode (SCE) is +241 relative to the hydrogen reference electrode.

[10] The figure was obtained from Lectures on Electrochemical Corrosion, 1973, p. 301, Chapter 7: Further Applications of Electrochemistry to Corrosion Studies, by Marcel Pourbaix, figure 111d, © 1973 Plenum Press, New York, with kind permission of Springer Science and Business Media.

Vita

Brandice Annette Green was raised in Memphis, Tennessee. She went to grade school at Harding Academy and graduated from White Station High School. From Memphis, Brandice moved to Knoxville to attend The University of Tennessee. She received her Bachelor of Science degree in 2002 and her Master of Science degree in 2004, both in materials science and engineering. In 2008, she obtained her Doctor of Philosophy degree in materials science in engineering.